Guardian ubiquitin E3 ligases target cancer-associated APOBEC3 deaminases for degradation to promote human genome integrity.

Irene Schwartz[1,2,3,*], Valentina Budroni[1,2,3,*] , Mathilde Meyenberg[1,4,5], Harald Hornegger[1,3,6], Kathrin Hacker[1,2], Siegfried Schwartz[7], Zuzana Hodakova[8], Daniel B. Grabarczyk[8], Julian F. Ehrmann[3,8,9,10], Sara Scinicariello[1,2,3], David Haselbach[8,11], Jörg Menche[1,4,5,12,13], Tim Clausen[8,11], G. Elif Karagöz[1,6], Gijs A. Versteeg[1,2,#]

[1]Max Perutz Labs, Vienna BioCenter Campus (VBC), Dr. -Bohrgasse 9, 1030, Vienna, Austria.
[2]University of Vienna, Center for Molecular Biology, Department of Microbiology, Immunobiology and Genetics, Dr. -Bohrgasse 9, 1030, Vienna, Austria.
[3]Vienna Biocenter PhD Program, a Doctoral School of the University of Vienna and the Medical University of Vienna, A-1030 Vienna, Austria.
[4]University of Vienna, Center for Molecular Biology, Department of Structural and Computational Biology, Dr. -Bohrgasse 9, 1030, Vienna, Austria.
[5]CeMM Research Center for Molecular Medicine of the Austrian Academy of Sciences, Lazarettgasse 14, AKH BT 25.3, A-1090 Vienna, Austria
[6]Medical University of Vienna, Center for Medical Biochemistry, Department of Molecular Biology, Dr. -Bohrgasse 9, 1030, Vienna, Austria.
[7]TU Wien, Faculty of Informatics, Favoritenstrasse 9-11, 1040 Vienna, Austria.
[8]Research Institute of Molecular Pathology (IMP), Vienna BioCenter Campus (VBC), Campus-Vienna-Biocenter 1, 1030, Vienna, Austria.
[9]Current affiliation: Department of Biological Chemistry and Molecular Pharmacology, Harvard Medical School, Boston, MA, USA
[10]Current affiliation: Program in Cellular and Molecular Medicine, Boston Children's Hospital, Boston, MA, USA
[11]Medical University of Vienna, Vienna BioCenter (VBC), Vienna, Austria.
[12]Faculty of Mathematics, University of Vienna, Oskar-Morgenstern-Platz 1, A-1090 Vienna, Austria
[13]Ludwig Boltzmann Institute for Network Medicine at the University of Vienna, Augasse 2-6, A-1090 Vienna, Austria
*These authors contributed equally
[#]Correspondence: gijs.versteeg@univie.ac.at

Highlights

- RNA-free APOBEC3 (A3) can enter the nucleus, leading to genomic mutations.
- Three E3 ligases specifically bind the RNA-binding domain of nuclear A3s.
- Cancer-associated A3B and A3H-I are thereby targeted for proteasomal degradation.
- These E3 ligases thus act as genome guardians by limiting A3-mediated mutagenesis.

Abstract

APOBEC family members play crucial roles in antiviral restriction. However, certain APOBEC3 (A3) proteins drive harmful hypermutation in humans, contributing to cancer. The cancer-associated A3 proteins are capable of transiting from the cytosol to the nucleus, where they can cause genome mutations. Here, we uncover a specific set of cellular pathways that protect genomic DNA from the major cancer-associated A3 proteins. Through genetic and proteomic screening we identify UBR4, UBR5, and HUWE1 as key ubiquitin E3 ligases marking cancer-associated A3B and A3H-I for degradation, thereby limiting A3-driven hypermutation. Mechanistically, UBR5 and HUWE1 recognize unoccupied A3 RNA-binding domains, thus promoting proteasomal degradation of APOBEC3 protein that is not engaged in its antiviral cellular function. Depletion or mutation of the E3 ligases in cells and human cancer samples increases A3-driven genome mutagenesis. Our findings reveal that UBR4, UBR5, and HUWE1 are crucial factors in a ubiquitination cascade that maintains human genome stability.

Keywords

APOBEC, cytidine deaminase, E3 ligase, ubiquitin, proteasome, protein degradation, genome hypermutation, UBR4, UBR5, HUWE1

Introduction

The human genome encodes seven members of the APOBEC3 (apolipoprotein B mRNA editing enzyme, catalytic polypeptide-like 3) family of cytidine deaminases[1]. These deaminases play a critical role in innate immunity against retro/lentiviruses by causing hypermutation of the viral cDNA[2,3]. The APOBEC3 (A3) family is under strong selective pressure in humans and other primates, with all seven members (A-H) possessing DNA C-to-U deaminase activity[4–7]. A3H is the oldest and most evolutionarily distant member of the A3 family and contains a unique zinc-coordinating motif in its deaminase domain[8,9]. In addition, it has the most haplotypes in the human population[1,10–12]. These haplotypes differ significantly in terms of their stability, subcellular localization and antiviral activity[13,14].

In contrast to this host-beneficial function, previous studies have shown that several A3 family members can have detrimental effects in humans by driving hypermutation of cellular DNA. Such hypermutation has been documented in diverse cancer types, thereby contributing to a broader, disadvantageous mutational landscape within these tumors[12,15–18].

Elevated levels of A3A, A3B, and A3H-I have been associated with mutagenesis in a range of cancers[15–17,19,20]. A3-mediated mutagenesis has been shown to drive some of the most prevalent mutational signatures in cancer, characterized by C-to-T transitions and clustered mutations (kataegis) at TCN trinucleotides[17,21–28]. APOBEC-associated mutational signatures have been identified in more than 70% of cancer types and around 50% of all cancer genomes[17,29,30]. These signatures are prominent in breast, lung, and bladder cancer, as well as other cancers[17,18,31–33]. A3A is overexpressed in a wide spectrum of human cancers and can induce kataegis and omikli, a form of extreme kataegis with more than 100 mutations per megabase[15–17,28,33]. A3B is overexpressed in many cancers and can generate APOBEC-specific SBS2 and SBS13 mutational signatures[17,34,35]. A3H occurs as several haplotypes in the human population, of which only the nuclear haplotype I (A3H-I) is associated with APOBEC signatures in breast and lung cancer, whereas the cytosolic haplotype II (A3H-II) is not[18,32].

Although these A3 deaminases mutagenize ssDNA substrates, their localization and activity are controlled through binding to double-stranded secondary structures in cellular RNAs[36,37]. In infected cells, cytosolic A3 binding to secondary structures in the viral RNA genome is essential for packaging into progeny virions, and subsequent mutagenesis of the viral cDNA during reverse transcription[12–14,38,39]. A3F, A3G, and A3H-II have been reported to have strong virus restrictive properties[10–13]. Importantly, these A3 proteins are not turned-over by the proteasome, and as a consequence of their stability, accumulate at high steady-state intracellular protein concentrations[10–14,38]. In contrast, other A3 members which have been associated with hypermutation signatures in various cancers, such as A3A, A3B, and A3H-I, are predominantly nuclear. These A3s are rapidly turned-over by the proteasome, and consequently are present at low intracellular protein concentrations[15–17,19,20]. A3H-I instability is determined by a single nucleotide polymorphism (SNP) (R105G) that is associated with increased nuclear localization[18]. It remains unclear why this SNP results in increased nuclear localization and instability. Nuclear localization of A3A, A3B, and A3H-I has been proposed to contribute to cancer hypermutation as it promotes access to genomic DNA[18].

The unstable A3 family members, though usually present at low nuclear levels, play a greater role in generating cancer-linked APOBEC mutational signatures than the more stable cytosolic variants[18,28]. However, it is unclear how the former group of A3s is more closely associated with cancer given their instability. We hypothesized that: **i)** deregulation of the limited protein concentrations of the unstable nuclear A3 members is likely sufficient to drive mutagenesis in cancers, **ii)** there are unidentified cellular factors that, under physiological conditions, maintain low nuclear A3 protein levels through active degradation, and **iii)** these cellular factors protect against cell-intrinsic genome mutagenesis by specifically keeping the cellular concentrations of potentially harmful nuclear A3 variants low. In addition, we predicted

that the absence of these unidentified 'guardian' factors would unleash hypermutation through increased nuclear A3 protein levels that compromise host genome integrity.

Through genetic screening and proximity proteomics, we identified UBR4, UBR5, and HUWE1 as E3 ligases that ubiquitinate A3B and A3H-I, thereby targeting them for proteasomal degradation. Consistent with their genome-guardian roles, ablation or mutation of these E3 ligases in cancer cell lines and human cancer samples led to increased APOBEC3-driven hypermutation.

Results

Proteasomal degradation controls protein levels of cancer-associated A3s.

Since the cancer-associated A3 family members, A3A, A3B, and A3H-I, only accumulate to low steady-state levels, we hypothesized that the cellular concentrations of these factors are controlled by protein degradation. To test this, constructs encoding all human A3 family members were delivered and expressed at similar steady-state protein levels (Fig. 1a). Subsequently, these cells were treated with the proteasome inhibitor epoxomicin (EPOX), and the effect on the various A3 proteins was determined by Western Blot (WB) analysis (Fig. 1a and 1b). Inhibition of proteasomal degradation significantly increased protein concentrations of the nuclear and cancer-associated A3A, A3B, and A3H-I proteins, indicating that their intracellular protein levels are substantially determined by proteasomal degradation. In contrast, protein levels of cytoplasmic A3s (A3D, A3F, A3G, and A3H-II), which are important for the innate immune response against retro/lentiviruses, were unaffected (Fig. 1a and 1b).

To further study the cellular mechanisms governing proteasomal degradation of nuclear, cancer-associated A3 protein levels in cells, we decided to use A3H as a model. The two predominant human A3H haplotypes represent each of the two identified phenotypes: A3H-I is nuclear, cancer-associated, and turned-over by the proteasome, whereas A3H-II is cytoplasmic and stable. Stability differences are reflected in much lower accumulation of A3H-I steady-state protein levels, as described for the endogenous protein in primary T lymphocytes[40]. This difference in stability is phenocopied upon exogenous expression in a wide variety of cell lines[12,40,41]. In line with previous reports[13,14,42], some exogenous A3H-I localized to the cytosol but a substantial portion was nuclear, whereas A3H-II was mostly localized in the cytoplasm (Fig. 1c).

Subsequently, we set out to measure the protein stability of A3H-I and A3H-II. To this end, we generated polyclonal RKO (human colon carcinoma) and HeLa (human cervical adenocarcinoma) cell lines expressing a stable myc-tagged mCherry internal control, and either A3H-I or A3H-II through a P2A ribosomal skip site (Fig. S1a). To compensate for the differences in steady-state protein levels of the two A3H haplotypes, A3H-I cells were transduced with a higher virus-like particle concentration, and, therefore, express more of the mCherry control (Fig. 1d). A3H protein stability was then determined in a chase experiment with the translation inhibitor cycloheximide (CHX), or in the presence of proteasome inhibitor MG132 (Fig. 1d and S1b). Consistent with rapid proteasome-mediated turnover, A3H-I protein accumulated at much lower steady-state levels than A3H-II, and was rapidly depleted in the presence of cycloheximide (Fig. 1d and S1b, compare lanes 1 and 6). These levels were increased 4- to 5-fold upon proteasome inhibition (Fig. 1e and S1c). Confirming their different stabilities, A3H-I was degraded with a half-life of 15 min. in RKO cells (Fig. 1f), and 10 min. in HeLa cells (Fig. S1d), whereas A3H-II remained stable during the 5 h. chase period.

A3H-I degradation was exclusively dependent on proteasomal degradation, as steady-state protein levels of the two A3H haplotypes were unaffected by inhibitors of autophagy/lysosomal degradation (Fig. S1e). Likewise, no differences in mRNA stability in the presence of Actinomycin D (ActD) (Fig. S1f), nor secretion (Fig. S1g) were measured between

the two A3H haplotypes, indicating that A3H-I protein levels were predominantly regulated through proteasomal degradation.

Consistent with this result, A3H-I and A3B (Fig. 1a-b) were ubiquitinated (Fig. S1h-i). Interestingly, while A3A was highly unstable (Fig. 1a-b), we consistently found it to be minimally ubiquitinated (Fig. S1h-i), which suggested that it may be regulated through a different - possibly ubiquitin-independent - mechanism than A3B and A3H-I.

To identify the residues important for A3H-I turnover, multiple lysine (K) residues in A3H-I were systematically grouped and mutated to arginine (R), based on their position in the A3H structure (Fig. S1j-k). All of these clustered K-to-R mutants accumulated at low steady-state protein levels, and were stabilized by proteasome inhibition, indicating that multiple lysines in different structural regions of A3H-I are likely important for its ubiquitination and degradation (Fig. 1g and 1h, Fig. S1a). In agreement with this conclusion and published data[43], when all lysine residues were mutated to arginine, A3H-I accumulated at 4-fold higher steady-state protein concentrations and were no longer affected by proteasome inhibition (Fig. 1g-h).

Together, these data indicate that protein levels of the nuclear, cancer-associated A3s, A3A, A3B, and A3H-I are regulated through proteasomal degradation, and that degradation of the model protein A3H-I depends on ubiquitination of multiple lysine residues.

The E3 ligases UBR4, UBR5, and HUWE1 independently mediate turnover of A3B and A3H-I.

The results described above positioned A3H-I as an excellent model to identify the cellular machinery that degrades it (and possibly other cancer-associated A3s), allowing its naturally occurring non-cancer-associated variant -A3H-II- to be used as a stable control to determine specificity.

To identify specific protein stability regulators of A3H-I, but not A3H-II, we set up a CRISPR-based genetic screening platform[44–46]. First, an RKO cell line was established harboring a doxycycline (DOX)-inducible Cas9-P2A-BFP construct, and an mCherry-A3H-II-P2A-GFP-A3H-I dual reporter (Dual-A3H-reporter), driven from an exogenous promoter (Fig. 2a). Inhibitor treatments confirmed that the two fluorophore-tagged A3H fusions phenocopied the protein stability pattern of their untagged counterparts (Fig. S2a).

To screen for regulators of A3H-I stability, the Dual-A3H-reporter cell line was transduced with a ubiquitin-focused lentiviral sgRNA library, Cas9 expression was induced, and cells with the highest or lowest 1-2% EGFP or mCherry fluorescence (EGFP^{high}, mCherry^{high}, EGFP^{low}, and mCherry^{low}) were collected after 3 and 6 days. Genomic DNA was isolated from the collected cells, and integrated sgRNA-coding sequences quantified by NGS (Fig. 2b).

Several sgRNAs were specifically enriched in EGFP-A3H-I^{high} sorted cells, which did not score in the mCherry-A3H-II^{high} sorted pool (Fig. 2c-d). Among the top hits were sgRNAs targeting several E3 ligases, E2 conjugating enzymes, DUBs/proteases and other degradation-associated genes. The top E3 ligases scored on day 6 were *UBR4*, *UBR5*, and *HUWE1. HUWE1* was also one of the top hits on day 3 (Fig. S2b-c). Interestingly, we also found the gene encoding the E2 conjugating enzyme UBE2D3, an E2 conjugase known to work with UBR5 and HUWE1, as one of the top hits for both days (Fig. 2c-d and S2c-d). These results identified UBR4, UBR5, and HUWE1 as strong, specific candidates mediating A3H-I degradation.

To test the validity and specificity of the screen results, each of these E3 ligases was targeted in isolation. Individual ablation of each of the E3 ligases significantly increased EGFP-A3H-I levels in the Dual-A3H-reporter screening cell line (Fig. 2e-f), as well as a polyclonal cell pool expressing the same construct (Fig. S2d), whereas mCherry-A3H-II fluorescence was not affected. We further tested whether the increased A3H-I steady-state protein levels in the E3 ligase knock-out cells stemmed from increased protein stability, by inhibiting translation with CHX. Therefore, we generated RKO-DOX-Cas9-MYC-mCherry-P2A-3xHA-A3H-I cells

207 harboring a triple-E3 ligase knock-out, treated them with CHX, and monitored A3H-I protein
208 levels over time by WB (Fig. S2e-f). Ablation of all three E3 ligases increased A3H-I half-life
209 from 21 min. to 1.9 h. (Fig. S2f), indicating that A3H-I degradation is compromised in the
210 absence of UBR4/UBR5/HUWE1.
211 Since we found that A3B is also turned-over in a proteasome-dependent manner (Fig.
212 1a-b), we reasoned that the same cellular machinery may be employed to keep its steady-
213 state levels low. Therefore, we set out to determine whether *UBR4*, *UBR5*, or *HUWE1* ablation
214 would also influence the abundance of A3B. Individual knock-out of *UBR4*, *UBR5,* and
215 *HUWE1*, increased endogenous A3B protein levels by 2.5 – 4-fold in RKO cells (Fig. 2g-h) as
216 well as in THP-1 monocytic cells (Fig. S2g-h), without affecting its mRNA levels (Fig. S2i).
217 Consistent with the hypothesis that the E3 ligases specifically degrade nuclear A3 members,
218 the predominantly cytoplasmic endogenous A3G remained unaffected by the E3 knock-outs in
219 THP-1 cells (Fig. S2g-h). In RKO cells, stability of endogenous A3G could not be evaluated
220 due to low A3G expression in these cells.
221 Importantly, knock-out of each of the individual ligases increased endogenous A3B
222 protein levels by 2-fold in each case (Fig. 2g-h), whereas simultaneous targeting of *UBR4*,
223 *UBR5*, and *HUWE1*, strongly increased A3B levels in an additive fashion to 6-fold in
224 comparison to its matching controls in which three safe harbor loci were targeted (Fig. 2g-h).
225 From these non-epistatic genetic interactions, we concluded that UBR4, UBR5, and HUWE1
226 each target A3B independently of the other two E3 ligases.
227 Collectively, these results identified the E3 ligases UBR4, UBR5, and HUWE1 as
228 important functional effectors of A3H-I degradation. This degradation-dependence is
229 conserved for cancer-associated A3B and is relevant in different human cell types. Our results
230 indicate that the three E3 ligases likely function redundantly, and thus poly-ubiquitinate A3B,
231 and possibly also A3H-I, independently of each other.

232 **UBR5 and HUWE1 form a complex with A3H-I and other unstable A3 deaminases in**
233 **cells.**
234 The above data argue that UBR4, UBR5, and HUWE1, identified through our specific genetic
235 screen, can directly or indirectly mediate A3 degradation. To complement the genetic screen,
236 we set out to also identify specific physical interaction partners of the unstable A3H-I. We
237 reasoned that overlapping factors identified in both approaches would be strong candidates
238 for factors that directly recognize A3B and A3H-I as ubiquitination substrates.
239 For unbiased identification of specific A3H-I interactors, TurboID (TID) proximity
240 labeling proteomics was performed (Fig. 3a). Three different RKO cell lines stably expressing
241 either DOX-inducible **a)** TID-A3H-I, **b)** TID-A3H-II, or **c)** TID-GFP as a control were generated.
242 Similar expression of each of the three constructs was achieved by inducing transgene
243 expression with different concentrations of DOX. Subsequently, proteins proximal to the
244 TurboID fusion proteins were covalently labeled by addition of biotin, after which biotinylated
245 proteins were isolated and identified by nLC-MS/MS.
246 We first compared the interactomes of A3H-I and A3H-II relative to the TID-GFP control.
247 In line with a recent publication[47], both A3H haplotypes share many interactors (Fig. 3b), mainly
248 comprising Gene Ontology (GO) terms for biological processes representing regulation of
249 translation, RNA metabolism, and RNA processing (Fig. S3a), which are amongst the top
250 scoring hits in both A3H haplotypes.
251 However, analysis of A3H-I-specific interactors identified protein ubiquitination and
252 DNA-metabolism related processes as the top ranked biological process GO terms (Fig. 3c).
253 Processes related to A3H-II-specific included translation, stress granule assembly, and RNA
254 metabolic processes (Fig. 3c), terms which are partially shared with the A3H-I interactome
255 (Fig. S3a). This reinforces the above results, which indicate that only A3H-I is targeted by the
256 ubiquitin-proteasome system. In addition, the enrichment for DNA-metabolism related
257 processes indicates that A3H-I may have access to DNA. As expected, top-ranked GO terms

258 for cellular compartments were enriched for nuclear terms in the case of the A3H-I-specific
259 interactome. In contrast, A3H-II-linked terms predominantly included cytoplasmic stress
260 granules and P-bodies (Fig. S3b), underlining the propensity of stable A3s to form high-
261 molecular-weight RNP complexes[48–51].
262 Consistent with a high degree of shared interaction partners, most interactors were not
263 unique to either the A3H-I/GFP or A3H-II/GFP haplotype (Fig. 3d-e; unlabelled data points in
264 upper-right quadrant). Amongst the specific proteins significantly enriched in the A3H-I
265 samples were the E3 ligases UBR5 and HUWE1 (Fig. 3d-f), which were also identified as
266 specific genetic interactors of A3H-I (Fig. 2c-d). Although UBR4 peptides were detected by
267 nLC-MS/MS, they were not significantly enriched in any one sample. In line with these MS
268 results, WB analysis detected UBR5 and HUWE1 in streptavidin-enriched lysates from TID-
269 A3H-I expressing cells, but not in lysates from TID-A3H-II or TID-GFP controls (Fig. S3c).
270 Consistent with the proximity labeling results, endogenous UBR5 and HUWE1 specifically
271 interacted with exogenously expressed A3H-I (Fig. 3g) and A3B (Fig. 3h) but did not co-IP with
272 the stable A3H-II haplotype (Fig. 3g).
273 Together, these data show that UBR5 and HUWE1 specifically interact with A3B and
274 A3H-I in cells and may thus directly ubiquitinate them. In contrast, UBR4 was not identified as
275 a specific A3B/A3H-I interactor in cells. UBR4 may either have an indirect effect on A3B and
276 A3H-I stability, or its interaction with these A3s may be too transient to detect in cell-based
277 assays.

278 **RNA binding protects A3 from E3 ligase binding and ubiquitination, thus promoting**
279 **stability in cells.**

280 RNA binding plays an important regulatory role in A3 localization and antiviral activity[39,48,52,53].
281 The antiviral family members A3H-II and A3G are retained in the cytoplasm through RNA
282 binding[39,48,52,53]. A3H haplotype I and II differ by three amino acids (Fig. S4a), with a single
283 glycine at position 105 determining the difference in stability[14,18,32]. In line with these data,
284 mutation of G105R in A3H-I turns it from unstable and partially nuclear, to stable and
285 predominantly cytosolic, phenocopying A3H-II (Fig. S4b-d). Conversely, R105G mutation
286 renders A3H-II unstable and partially nuclear, thereby phenocopying A3H-I (Fig. S4b-d).
287 Previous work has suggested that the R105G mutation may render the A3H protein less
288 capable of binding dsRNA structures, leading to diminished antiviral potential[14,18,32].
289 Furthermore, introducing the G105R into A3H-I, strongly reduced its ubiquitination (Fig. S4e)
290 and interaction with UBR5 and HUWE1 (Fig. S4f). Conversely, the A3H-II R105G mutation
291 resulted in its ubiquitination (Fig. S4e) and association with UBR5 and HUWE1 (Fig. S4f).
292 Based on these and prior observations[14,18,32], we hypothesized that lack of RNA binding
293 leads to the re-localization of cytoplasmic A3H-II to the nucleus and renders it a substrate for
294 proteasomal degradation. Therefore, we tested previously characterized A3H-II mutants
295 (W115A and R175/176E)[39], which harbor mutations in the α6 helix and the structurally adjacent
296 loop 1, which mediate RNA binding. In line with previous reports[39,48,52,53], lack of RNA binding
297 decreased cytosolic A3H-II levels and increased nuclear localization (Fig. S4g). In contrast to
298 the stable wild-type (WT) A3H-II, the RNA-binding mutants were highly unstable: their levels
299 decreased rapidly upon translation inhibition yet stabilized in the presence of a proteasome
300 inhibitor (Fig. 4a-b). These results indicated that RNA binding affects two characteristics of
301 cellular A3: **i)** it retains it in the cytosol, and **ii)** it prevents its degradation.
302 Next, we asked in which compartment the respective A3H mutants are degraded. For
303 this experiment, A3H WT and RNA-binding mutant constructs were expressed at similar levels,
304 after which their accumulation upon proteasome inhibition was assessed in the nuclear and
305 cytosolic cell fractions (Fig. 4c-d). As expected, A3H-II protein levels in whole cell extracts were
306 not affected by proteasome inhibition, whereas it significantly increased the levels of the
307 unstable A3H-I and A3H-II RNA-binding mutants (Fig. S4h-i). Analysis of fractionated samples
308 showed that A3H-I and the RNA-binding mutants of A3H-II predominantly accumulated in the

309 nucleus when their degradation was blocked (Fig. 4c-d), indicating that unstable A3H variants
310 are degraded in the nucleus. Moreover, RNA-binding mutants of A3H-II were strongly
311 ubiquitinated (Fig. 4e) and co-immunoprecipitated with UBR5 and HUWE1 (Fig. 4f), indicating
312 that loss of RNA binding renders A3H-II a substrate for degradation by the identified E3 ligases.
313 These data indicated that RNA binding may be a general mechanism by which A3
314 protein degradation is prevented, and may be the reason why other family members, such as
315 A3G, are stable. To test this hypothesis, we analyzed the stability of WT A3G compared to
316 three A3G RNA-binding mutants[54] in cells. Consistent with comparable RNA-binding
317 mechanisms across the A3 family, structural alignment with A3H showed that the helix region
318 of A3G CD1-containing mutations superimposed with the α6 helix of A3H-II, identifying it as a
319 likely determinant for RNA binding (Fig. S4j). In contrast to WT A3G, steady-state protein levels
320 of A3G RNA-binding mutants increased upon proteasome inhibition, underlining the
321 importance of the integrity of this helix, its ability to bind RNA, and formation of high molecular
322 weight complexes for protein stability (Fig. 4g-h). Notably, A3G-Y181/182A was stabilized less
323 upon EPOX treatment (Fig. 4g-h), possibly resulting from incomplete disruption of the α-helix
324 by these mutations.
325 In agreement with the above data, which argue that RNA binding prevents recognition
326 of A3 as substrates for degradation, the A3G 6M and FWKL mutants were ubiquitinated (Fig.
327 4i) and co-immunoprecipitated with UBR5 and HUWE1 (Fig. 4j), whereas their WT
328 counterparts did not. Lower levels of A3G Y181/182A ubiquitination and E3 interaction (Fig.
329 4i-j) correlated with reduced instability of this mutant compared to WT protein (Fig. 4g-h),
330 potentially stemming from differences in their RNA-binding.
331 Collectively, these results show that the RNA-binding ability of A3H-II and A3G are
332 important for their stability. Absence of RNA binding enables UBR5 and HUWE1 engagement,
333 ubiquitination, and eventual proteasomal degradation in cells.

334 **RNA binding by APOBEC3 proteins prevents their recognition and ubiquitination by**
335 **E3 ligases *in vitro*.**
336 Cell-based assays showed that impaired RNA binding renders A3 proteins substrates for
337 proteasomal degradation. Therefore, we hypothesized that the identified E3 ligases recognize
338 the unoccupied RNA-binding surface of A3 proteins, and that RNA binding thus prevents
339 ubiquitination. However, RNA binding has two confounding effects in cells as it influences both
340 A3 localization, and stability. To test the hypothesis that the E3 ligases recognize unengaged
341 RNA-binding interfaces, we therefore set out to analyze direct E3 ligase targeting of A3H in a
342 cell-free *in vitro* reconstituted ubiquitination system.
343 First, A3H-I and A3H-II were purified from *E. coli* as previously described[39,52,55,56].
344 Despite several attempts during purification to remove co-purified bacterial RNA bound to A3H-
345 I WT and A3H-II WT with high salt or extensive RNase A treatment, we were unable to purify
346 these proteins without any residual bound RNA, as both proteins became insoluble and
347 precipitated upon complete removal of RNA (not shown). For that reason, we additionally
348 purified an A3H-II RNA-binding mutant (A3H-II-RBM) from *E. coli*, which has been previously
349 reported to purify as an RNA-free monomer (Fig. 5a)[39]. In cells, this mutant phenocopied the
350 stability of other A3H-II RNA-binding mutants (W115A and R175E/176E) (Fig. S5a-b).
351 A3H-I eluted exclusively as a monomer in size exclusion chromatography (SEC),
352 whereas A3H-II eluted both as monomer and dimer (Fig. S5c). However, both proteins were
353 bound to substantial amounts of short RNA fragments, as visualized by denaturing PAGE
354 analysis (Fig. 5b), consistent with previous reports[39,52,55,56]. In contrast, A3H-II-RBM eluted as
355 a monomer, free from any bound RNA (Fig. 5b and S5c).
356 Our cell-based data suggested that UBR5, HUWE1, and UBR4 poly-ubiquitinate A3H-
357 I in cells, likely independently of one other (Fig. 2g-h). To validate these results in a cell-free
358 system, we performed *in vitro* ubiquitination assays using purified proteins and either A3H-I,
359 A3H-II or the RNA-free A3H-II-RBM mutant as substrates. Consistent with our cell-based data,

360 UBR5 and HUWE1 independently poly-ubiquitinated A3H-II-RBM and A3H-I (Fig. 5c-d). Both
361 enzymes polyubiquitinated the RNA-free A3H-II-RBM mutant most strongly, followed by RNA-
362 bound A3H-I, with A3H-II showing the lowest modification levels (Fig. 5c-d). All three A3
363 substrates were efficiently mono-ubiquitinated by the E2 conjugase UBE2A (a.k.a. RAD6A) in
364 the absence of its E3 ligase UBR4 (Fig. 5e). Addition of UBR4 efficiently extended the mono-
365 ubiquitin into poly-ubiquitin chains (Fig. 5e; compare samples 4-6 with 7-9). These data
366 suggest that UBR5 and HUWE1 indeed poly-ubiquitinate A3H independently. In contrast,
367 UBR4 requires prior substrate mono-ubiquitination by its specific E2 conjugase UBE2A and
368 adopts an E4 ligase poly-ubiquitin chain-extending function. However, UBR4-dependent chain
369 extension is not haplotype-specific, suggesting that UBR4 can likely extend any pre-formed
370 chains on A3H.
371 Cell-based assays had shown that while A3H-I is turned-over by the proteasome,
372 engineered RNA-binding mutants were substantially more unstable (Fig. 4a-b). Since A3H-I
373 purified from *E. coli* bound to substantial amounts of bacterial RNA, we speculated that it might
374 bind RNA in cells. However, the equilibrium may be shifted to a larger unbound fraction of
375 A3H-I in cells compared to A3H-II. Based on the SEC profiles, we predicted that the vast
376 majority of purified WT A3H protein molecules were RNA-bound in our preparations (Fig. S5c),
377 possibly not fully mirroring in-cell equilibrium conditions. Consistent with this notion, RNA-
378 bound A3H-I and A3H-II were substantially less ubiquitinated *in vitro* by each of the three E3
379 ligases compared to A3H-II-RBM. We hypothesized that this difference might stem from the
380 co-purified RNA shielding the A3H substrates from E3 ligase engagement and predicted that
381 RNA removal during the reaction would render them susceptible to ubiquitination. To test this,
382 RNase A was added to the ubiquitination reaction mixtures. Under these conditions, both A3H-
383 I and A3H-II were ubiquitinated by UBR5, HUWE1, and UBR4 to a similar extent as the A3H-
384 II RBM (Fig. 5f-h). In contrast, ubiquitination of the RNA-free A3H-II-RBM mutant was
385 independent of RNase A addition. From these data, we concluded that RNA indeed shields
386 either the ubiquitination- or E3 ligase recognition site of A3H. Given that ubiquitination of
387 multiple lysine residues contributes to A3H turnover (Fig. 1g-h), we concluded that the RNA-
388 binding region in A3H is likely the recognition site of the E3 ligases, after which the flexibility
389 of these large E3 ligases would allow ubiquitination of multiple surface lysine residues.
390 Together, these data showed that RNA binding 'shields' A3H from ubiquitination by the
391 E3 ligases. In the absence of RNA binding, UBR5 and HUWE1 independently poly-ubiquitinate
392 A3H. Similarly, in the absence of RNA binding, mono-ubiquitination by UBE2A was enhanced,
393 which further increased UBR4 E4 ligase activity, extending poly-ubiquitin chains on pre-formed
394 (mono)-ubiquitin marks (Fig. 5h). Based on these findings and published data[57], it seems likely
395 that UBR4 can additionally amplify poly-ubiquitination in cellular contexts, by targeting
396 substrates partially ubiquitinated by UBR5 or HUWE1, or factors that were not identified in our
397 screens.

398 **E3 ligase loss or mutation increases APOBEC signature mutations.**
399 Single Base Substitution (SBS) signature mutations are specific patterns of genetic mutations,
400 categorized based on their types and surrounding sequence context. Unbiased computational
401 analysis has identified over 30 different SBS patterns; among these are two highly APOBEC-
402 specific signatures (SBS2, SBS13)[24,30].
403 As ablation of *UBR4*, *UBR5*, and *HUWE1* elevated levels of cancer-associated A3B
404 and A3H-I (Fig. 2e-h), we hypothesized that this would increase A3-dependent mutagenesis.
405 To test this hypothesis in an experimentally feasible time frame, we generated an RKO cell
406 line with exogenous A3H-I-driven mutagenic activity (Fig. S6a) and analyzed APOBEC
407 signature mutations. RKO cells have no detectable endogenous A3A or A3H expression, yet
408 express detectable A3B protein levels (Fig. 2g). Therefore, these cells would predominantly
409 accumulate APOBEC mutations driven by the exogenous A3H-I, and potentially to a lesser
410 extent, by endogenous A3B.

411 These cells were transduced with sgRNAs individually targeting *UBR4*, *UBR5*, or
412 *HUWE1*, sorted for sgRNA-positive cells, after which gene-editing was induced with DOX.
413 Given some eventual growth impairment of E3 ligase knock-out cell pools and potential out-
414 selection over extended cultivation periods, the maximum analysis period with a substantial
415 E3 ligase knock-out population after Cas9 induction was restricted to four doublings (Fig. S6b).
416 Cellular gDNA was isolated from these samples and mutREAD sequencing was performed to
417 determine changes in SBS signature mutations in the gDNA of the analyzed cell pools in an
418 unbiased manner (Fig. 6a)[24,30,58]. This analysis yields a relative distribution of all SBS signature
419 mutations identified in the gDNA of the different genotypes.
420 In *AAVS1*-targeted control cells, three major SBS signatures were identified (Fig. 6b;
421 SBS5/6/15), commonly found in colorectal cancer cell lines. However, APOBEC-specific
422 signatures were not present in these samples. In contrast, APOBEC signature mutations
423 (SBS2 and SBS13) were readily detected in samples from *UBR4*- and *UBR5*-targeted cells
424 (Fig. 6b-c and S6c-d). The total number of mutations accumulated over the cultivation period
425 increased in sg*UBR4* and sg*UBR5* cells, indicating that the increase in APOBEC signature
426 largely represented elevated mutational activity in these samples (Fig. 6c).
427 In contrast to the other two E3 genotypes, the increase in APOBEC signature was not
428 as pronounced in *HUWE1* knock-out cells (Fig. 6b-c and S6c-d). This correlated with having
429 fewer mutations (Fig. 6c), and the slowest doubling-time of the tested genotypes. We speculate
430 that cells with the strongest increase in mutagenesis in a less-fit *HUWE1* knock-out
431 background, may have been counter-selected during the cultivation period, resulting in lower
432 mutation rates overall.
433 Taken together, our data showed that under conditions in which degradation of A3
434 proteins is compromised, A3-driven signature mutations increase, resulting in an elevated
435 mutational burden on the gDNA.
436 Lastly, we asked whether our cell-based findings would translate to a human setting.
437 To this end, we tested whether mutation – and thus possible loss of function - of the identified
438 E3 ligases, correlated with a specific increase in APOBEC-signature burden in cancer patient
439 samples. For this purpose, cancer whole-genome sequence samples from the PCAWG
440 study[30,59] were sorted into bins, in which the gDNA sequence for a particular E3 ligase was
441 either WT (wt) or had at least one SNV or InDel outside of intronic regions (mut) (Fig. 6d). In
442 addition, samples in which any of the three E3 ligase genes (*UBR4*, *UBR5*, *HUWE1*) was
443 mutated ($E3s_{comb}$) were compared to all remaining samples.
444 Subsequently, SBS mutational signatures were retrieved, and the binned groups of
445 each E3 ligase gene compared in a pairwise fashion. To account for a bias in the total
446 mutational burden in the mutant groups of *UBR4*, *UBR5*, *HUWE1,* and unrelated E3 ligases
447 (Fig. S6e), mutational counts were normalized to the total number of mutations in each
448 individual sample. This enabled direct comparison of relative SBS signature distributions
449 between sample groups.
450 In line with our cell-based experiments, *UBR5*- and *HUWE1*-mutated cancer samples
451 had significantly more APOBEC signature mutations (SBS2/SBS13) compared to their
452 respective WT control groups (Fig. 6e and S6f). In contrast to our cell-based data, there was
453 no significant difference in APOBEC signature mutations between wild-type and *UBR4*-mutant
454 samples (Fig. 6e and Fig. S6f).
455 The effect in *UBR5*- and *HUWE1*-mutant samples was specific for APOBEC mutational
456 signatures, as mutations in unrelated E3 ligases did not correlate with significant changes in
457 APOBEC signature mutations (Fig. S6g-h). In addition, mutations in *UBR5* or *HUWE1* did not
458 correlate with an increase in other abundant, non-APOBEC signatures (Fig. S6i-k;
459 SBS1/SBS5/SBS18). In fact, the frequencies of these non-APOBEC signatures were
460 predominantly decreased in mutant samples (Fig. S6i-k), which likely stems from the
461 normalization to total mutation counts (Fig. S6e). This indicates that -as one would expect-

there is a bias toward greater numbers of total mutations in mutated samples, yet a significantly higher fraction of APOBEC signatures specifically occur in *UBR5* and *HUWE1* mutant cancers (Fig. 6e and Fig. S6f). In agreement with our cell-based data, this suggests that *UBR5* and *HUWE1* are important for curtailing the levels of specific APOBEC proteins in human cancers thereby limiting APOBEC-driven mutagenesis.

Collectively, this study identifies a hitherto unknown framework of cellular guardians that keeps steady-state levels of nuclear A3 proteins low. Our data support a model in which the core of this network consists of UBR5 and HUWE1, E3 ligases that directly recognize A3B and A3H-I and mark them for degradation (Fig. 6f). UBR4 may play an indirect, amplifying role through its E4 ubiquitin chain extension activity.

UBR5 and HUWE1 specifically engage non-RNA-bound A3 proteins through recognition of their unoccupied RNA-binding surfaces. Since RNA binding is important for A3 cytosolic retention, this framework ensures **i)** specific targeting of nuclear A3 proteins that pose a risk to our genome, while **ii)** leaving cytosolic A3 family members available as antiviral restriction factors. Since broad mutational landscapes in cancers enable escape from therapeutic interventions, our findings enable future studies into the identified E3 ligases as possible diagnostic or therapeutic targets.

Discussion

High A3 levels have been identified in many cancers, and are correlated with higher A3-induced mutational rates (reviewed in [60]), with A3A, A3B and A3H-I being the major sources of these signatures[18,28,34,35]. The prevalence of APOBEC signatures, found in >50% of all cancers and across cancer types[30], underpins the critical importance of understanding how human cells restrict APOBEC-induced mutagenesis of their own genomes. Thus far, studies have focused on the differential transcriptional regulation of cancer-associated A3s to explain the high prevalence of APOBEC signatures in tumors. However, other major modes of A3 regulation may play a critical role in cancer mutagenesis.

Here, we identified a novel post-translational regulatory mechanism regulating cellular A3B and A3H-I protein abundance, two major APOBEC signature drivers[18,28,34,35]. The mechanisms we uncovered limit APOBEC-induced mutagenesis in cells. We show that the loss of the central E3 ligases, UBR4, UBR5, and HUWE1, stabilizes A3B and A3H-I proteins, resulting in their accumulation and eventually increasing APOBEC-related mutational burden. Our findings reveal a previously unknown layer of regulation acting to limit cellular A3 protein levels. In the absence of these guardian factors, A3s may broaden the mutational landscape in late-stage cancer, and affect the development of therapy resistance[33,61–64].

RNA binding stabilizes A3 proteins

RNA binding mediates important A3 regulatory functions, bridging A3s to form high-molecular-weight complexes in the cytoplasm and inhibiting catalytic activity[36,51,65–70]. In an antiviral context, this leads to inhibition of A3 deaminase activity by the viral RNA until it is released during reverse transcription. However, nuclear A3 accumulation is often the result of diminished cytosolic RNA binding[39], and comes at the risk of accumulation of an active enzyme with access to the host genome. This requires a cellular framework to ensure high levels of cytosolic antiviral A3 variants, while limiting the concentrations of nuclear, active A3 variants in order to preserve genome integrity.

Our data provide a mechanistic explanation of how such selectivity is achieved: E3 ligases target the A3 RNA-binding surface, a region that also determines its subcellular localization based on whether RNA is bound. This ensures that variants that bind less RNA and are more nuclear, simultaneously become E3 ligase substrates, resulting in their

510 degradation. Our *in vitro* experiments showed that RNA binding plays a major mechanistic role
511 in determining whether UBR5 and HUWE1 can engage A3 proteins as substrates (Fig. 5). Cell-
512 based microscopy and fractionation experiments showed that A3H-I and RNA-binding mutants
513 are predominantly nuclear and degraded in the nucleus (Fig. 4). This degradation may be
514 mediated by the large fraction of cellular proteasomes residing in the nucleus[44]. However, it
515 remains to be determined where in cells E3-substrate interaction and ubiquitination takes
516 place. Localization of the E3 ligases varies in different cell types, and previous analysis places
517 all three E3 ligases in the nucleus and cytosol[71–78].
518 Previous work showed that A3H-II has strong RNA-binding activity[36,51,65–70]. However,
519 since the R105G mutation lies outside of the RNA-binding interface, it was unclear whether
520 A3H-I has differential RNA-binding ability, and whether this may underlie the phenotypic
521 changes in localization and stability. Our cell-based data consistently showed intermediate
522 nuclear localization and instability phenotypes for A3H-I, in between A3H-II and designed
523 RNA-binding mutants. Moreover, SEC analysis of recombinant A3H-I revealed that it still co-
524 purified with substantial amounts of bound RNA, albeit less than its A3H-II counterpart.
525 Moreover, while A3H-II purified in part as RNA-bound dimers, A3H-I was exclusively obtained
526 as an RNA-bound monomer.
527 In line with the findings of a recent interaction study[79], our cell-based TurboID
528 proteomics showed that A3H-II and A3H-I share many interactors related to RNA processes,
529 albeit fewer for A3H-I. This further supports a model in which A3H-I is still bound by RNA in
530 cells, but to a lesser extent than A3H-II. Together, our findings indicate that A3H-I is likely a
531 partial RNA-binding mutant, for which the equilibrium in cells is shifted towards a more
532 unbound state. As a consequence, it may be less amenable to forming high molecular weight
533 RNA/A3 RNP complexes, as previously described[36,51,65–70], allowing passive diffusion into the
534 nucleus[42]. The R105G mutation and structural changes in its β-sheet may affect proper
535 positioning of the distal RNA-binding domain. Nevertheless, we cannot rule out additional
536 effects on protein-protein interactions required for high molecular weight complex formation as
537 seen for A3H-II[36,51,65–70]. At least two nuclear and unstable A3H haplotypes arose
538 independently in evolution[10,12,13,40], suggesting either negative counter-selection of cytosolic
539 variants, or positive selection for nuclear A3 enzymes. In line with this latter notion, various A3
540 members have been reported to counter infections of unrelated nuclear viruses and
541 transposable elements with DNA genomes or replication intermediates[80–86]. It is, therefore,
542 essential to balance required nuclear antiviral activity with preventing genomic hypermutation.
543 The identified E3 ligase machinery ensures this balance, by only recognizing nuclear A3s that
544 are not engaged with RNA.

545 **Substrate preference and cooperativity of UBR4, UBR5, and HUWE1**

546 The three identified A3-targeting E3 ligases, UBR5, HUWE1, and UBR4, have previously been
547 linked to the turnover of a diverse array of substrates, thereby exerting control over numerous
548 cellular processes[57,71,72,74,87–105]. This suggests that these E3 ligases possess the ability to
549 identify multiple substrate classes based on broad biochemical or biophysical characteristics.
550 Supporting this idea, recent structural studies of HUWE1 have revealed three distinct
551 substrate-binding domains[106,107], facilitating the recognition and ubiquitination of unbound
552 nucleic acid binding proteins as well as ubiquitinated/PARylated substrates. Similarly, UBR5
553 was recently shown to bind and ubiquitinate unengaged transcription factors[87], and has the
554 ability to function as a ubiquitin chain elongating E4[90,91]. In combination with our findings in this
555 study, these results indicate that HUWE1 and UBR5 are both important players in recognizing
556 and degrading unengaged DNA- and RNA-binding proteins.
557 Although comprehensive structural information is currently unavailable for UBR4, its
558 involvement in ubiquitinating aggregation-prone nascent polypeptides during proteotoxic
559 stress[94], diverse mitochondrial proteins[87,95], and ER-associated degradation substrates[96]
560 identified in independent screens suggests that this large E3 ligase may also possess the

561 capability to recognize various substrate classes, potentially contingent upon its interaction
562 with different partners. While UBR4 may define substrate selection in other cellular contexts,
563 our data show that in the context of A3 degradation, it likely plays a role as a chain extending
564 E4 ligase. In line with this, UBR4 was neither enriched in our TurboID experiments, nor
565 identified by co-IP (Fig. 3), pointing towards a more distal engagement. However, it could be
566 that UBR4 is specifically recruited to UBR5- or HUWE1-containing complexes in cells to
567 amplify their ubiquitination, and, thereby, proteasomal degradation. In agreement with previous
568 reports[57,108], our cell-based (Fig. 2g) and *in vitro* (Fig. 5) data suggest that UBR4, UBR5 and
569 HUWE1 have redundant functions and cooperate to assemble ubiquitin chains on their
570 substrates.

571 **Maintenance of genome integrity**

572 Prior studies have indicated that A3A and A3B are responsible for a substantial part of
573 APOBEC signatures in cancer[28,34]. The presence of the distinct A3H-I haplotype was linked to
574 increased APOBEC signatures in breast and lung cancers[18,32]. However, additional evidence
575 for a contribution of A3H-I to APOBEC3 signatures in other cancers is sparse and little research
576 focuses on A3H-I. We show that APOBEC signatures accumulate in cells in which A3H-I is
577 exogenously expressed, and that impairment of A3H-I and A3B degradation mediated by
578 UBR4, UBR5 and HUWE1 results in an increase in their protein levels, paralleled by an
579 increase in APOBEC signature mutations (Fig. 6). In agreement, we found a significant
580 correlation between *UBR5* or *HUWE1* mutations in human cancer genomes and increased
581 APOBEC signature mutations in these samples. Therefore, analysis of A3 protein levels and/or
582 the mutational status of UBR5 and HUWE1 may prove helpful as a future diagnostic tool that
583 acts as a proxy for the tumor mutational landscape and indicates the likelihood of developing
584 treatment-resistance.

585 Several proteasome inhibitors are used as therapy for treating multiple myeloma and
586 mantle cell lymphoma, yet relapses and acquired resistance are frequent[109]. The role of
587 APOBEC mutagenesis in cancer therapy and evolution has been suggested to be a double-
588 edged sword. Depending on the level of APOBEC mutagenesis, it could either contribute to
589 greater treatment effectiveness by driving error-catastrophe and synthetic-lethality in cancer
590 cells, while on the other hand it could have detrimental effects by broadening the mutational
591 landscape in tumors, thereby increasing the frequencies of therapeutic resistance[110]. With our
592 finding that proteasomal degradation plays an important role in regulating cancer-associated
593 APOBEC3 protein levels, the application of proteasome inhibitors in cancer therapy and the
594 resulting increase in cellular A3 levels should be assessed accordingly.

595 **Future directions**

596 Our data presents the importance of a previously underrated RNA-dependent regulatory
597 mechanism of APOBEC3 protein activity and localization through proteasomal degradation
598 controlling levels of nuclear APOBEC3s. While A3A is even more unstable than A3B and A3H-
599 I, it is not ubiquitinated (Fig. 1a and S1h), indicating that cancer-associated A3A protein levels
600 are controlled by a different cellular mechanism. The lack of ubiquitination could suggest A3A
601 is degraded in a ubiquitin-independent manner. Moreover, previous work has shown that A3A
602 transcription is influenced by proteasome inhibition[111], possibly contributing to the observed
603 increase in A3A protein levels.

604 Nevertheless, it raises the question of why A3A is not a UBR5/HUWE1 substrate, in
605 contrast to A3B and A3H-I. A3A differs from A3B and A3H-I as it does not form large multimeric
606 complexes[112–114]. The protein sequence of single-domain A3A resembles the C-terminal
607 domain (CTD) of A3B and A3G. However, only the inactive N-terminal domain (NTD) of dual-
608 domain A3s is responsible for RNA binding[115,116], and contains the critical RNA-binding
609 residues comprising bulky hydrophobic and positively charged amino acids in loop7 and the
610 α6-helix. As the sequence of A3H is similar to the NTD of A3B, we speculate that A3A does

not possess the "RNA-binding surface" and can therefore not be recognized by the E3 ligases identified in this study. Thus, future studies will be necessary to identify mechanisms through which A3A protein levels are regulated by proteasomal degradation.

In sum, our current data identify a critical mechanism by which A3B and A3H-I are linked to APOBEC mutation signatures, making these cancer-associated A3s a strong starting point for future development of therapeutic and diagnostic tools.

Acknowledgements

Next Generation Sequencing analysis was performed by the Vienna Biocenter Core Facilities using the VBCF instrument pool. Proteomics analyses were performed by the Mass Spectrometry Facility at Max Perutz Labs using the VBCF instrument pool; we particularly thank Markus Hartl and WeiQiang Chen for their expert support. Flow cytometry analyses were performed at the BioOptics FACS Facility at the Max Perutz Labs using the Max Perutz Labs instrument pool; we particularly acknowledge Kitti Csalyi, Thomas Sauer, and Johanna Stranner for expert support. Microscopy was performed at the BioOptics Light Microscopy Facility at the Max Perutz Labs; we thank Thomas Peterbauer and Irmgard Fischer for their expert support and training. We thank Johannes Bock for establishing TurboID-related reagents and methodology, Robert Kurzbauer for purification of recombinant proteins, Anna Hakobyan for advice on cancer genome data analysis, Joanna Loizou for expert advice on DNA damage assays, and Marcel Ooms for APOBEC expertise, discussions, and manuscript feedback. We are grateful to the 'Signaling Mechanisms in Cellular Homeostasis' doctoral program community, in particular Thomas Decker, Pavel Kovarik and their labs for their technical expertise and help. We thank Life Science Editors for editing services. The results shown here are in whole or part based upon data generated by the TCGA Research Network: https://www.cancer.gov/tcga

Funding sources: This work was funded by Stand-Alone grants (P30231-B, P30415-B, P36572, P36945), Special Research Grant (SFB grant F79), and Doctoral School grant (DK grant W1261) from the Austrian Science Fund (FWF) to GAV, an Austrian Science Fund Special Research Grant (FWF, SFB F79) to TC, and an ERC European Union's Horizon 2020 research and innovation program grant (AdG 694978) to TC and the Austrian Science Fund Special Research Grant (SFB grant F79) to GEK. VB and S.Sci are the recipients of a DOC fellowship of the Austrian Academy of Sciences. Research at the IMP is supported by Boehringer Ingelheim and the Austrian Research Promotion Agency (Headquarter grant FFG-852936).

Funding Statement

The funders had no role in study design, data collection and interpretation, or the decision to submit the work for publication.

Materials availability statement

All data generated or analyzed during this study are included in the manuscript and supporting files. Data and code pertaining to genomics and mutational signature analysis can be found on https://github.com/menchelab/apobex.

Author contributions

Conceptualization, G.A.V., I.S., V.B., D.H., T.C. and E.K.; Methodology, G.A.V., I.S., V.B., M.M., H.H., Z.H., D.B.G. and J.F.E.; Software, M.M, I.S. and S.S.; Validation, I.S. and V.B.; Formal Analysis, I.S., V.B. and M.M.; Investigation, I.S., V.B. and K.H.; Resources, Z.H., D.B.G., J.F.E., S.Sci.; Data Curation, I.S., V.B., M.M and G.A.V.; Writing – Original Draft, I.S., V.B. and G.A.V.; Writing – Review & Editing, I.S., V.B., M.M., H.H., K.H., S.S., Z.H., D.B.G.,

J.F.E., S.Sci, D.H., J.M., T.C., E.K. and G.A.V.; Visualization, I.S., V.B. and M.M.; Supervision G.A.V.; Project Administration, G.A.V.; Funding Acquisition, G.A.V.

Declaration of interests

The authors declare no competing interests.

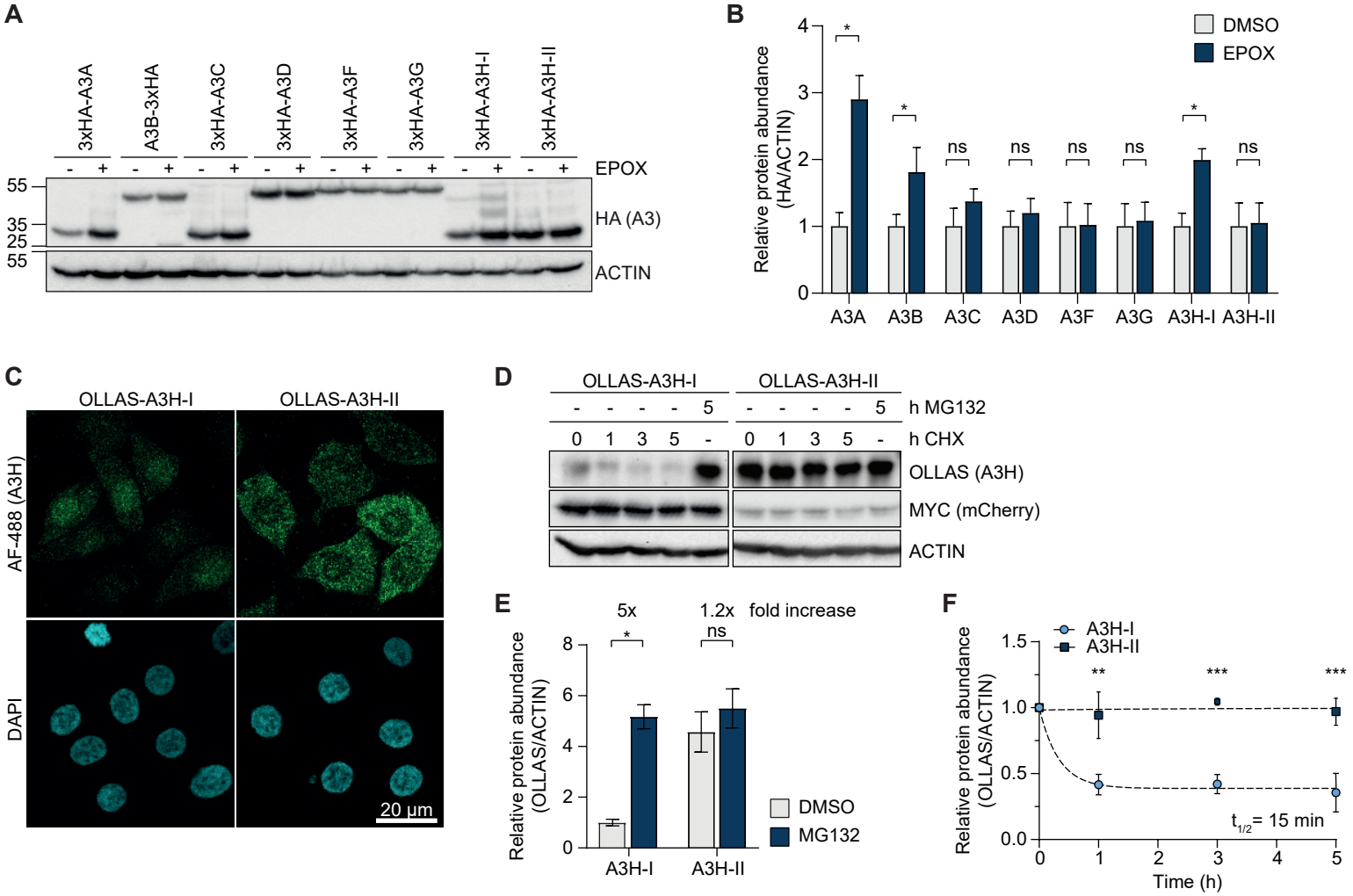
A
3xHA-A3A
A3B-3xHA
3xHA-A3C
3xHA-A3D
3xHA-A3F
3xHA-A3G
3xHA-A3H-I
3xHA-A3H-II
EPOX
55
35
25
55
HA (A3)
ACTIN
B
DMSO
EPOX
Relative protein abundance (HA/ACTIN)
A3A
A3B
A3C
A3D
A3F
A3G
A3H-I
A3H-II
ns
C
OLLAS-A3H-I
OLLAS-A3H-II
AF-488 (A3H)
DAPI
20 µm
D
OLLAS-A3H-I
OLLAS-A3H-II
h MG132
h CHX
OLLAS (A3H)
MYC (mCherry)
ACTIN
E
5x
1.2x
fold increase
Relative protein abundance (OLLAS/ACTIN)
DMSO
MG132
A3H-I
A3H-II
F
A3H-I
A3H-II
Relative protein abundance (OLLAS/ACTIN)
$t_{1/2}$= 15 min
Time (h)
G
3xHA-A3H-I
WT
M1
M2
M3
M4
M5
M6
K-
EPOX
HA (A3H)
MYC (mCherry)
ACTIN
H
DMSO
EPOX
Relative A3H expression (HA/MYC)
WT
M1
M2
M3
M4
M5
M6
K-

663 **Figure 1. Proteasomal degradation controls protein levels of cancer-associated A3s.**
664 **(a)** HEK-293T cells were transfected with different amounts of 3xHA-tagged A3 expressing
665 plasmids to achieve similar steady-state A3 protein levels. 24 h. post transfection, cells were
666 treated for 16 h. with EPOX, and protein levels were analyzed by WB, and **(b)** quantified
667 (means and SD, multiple unpaired t-tests, * $p < 0.05$, $n = 5$). **(c)** RKO cells stably expressing
668 OLLAS-A3H-I/II were fixed, and their subcellular localization determined by
669 immunofluorescence confocal microscopy; scale bar: 20 µm. **(d-f)** Lentiviral expression
670 constructs encoding A3H-I or A3H-II were delivered to RKO cells at different integration rates
671 to obtain comparable A3H-I and A3H-II protein levels in the presence of proteasome inhibitor.
672 Polyclonal cell pools were treated with CHX or MG132 for the indicated times, **(d)** protein levels
673 analyzed by WB, **(e)** relative A3H-I and A3H-II protein levels quantified by densitometry (means
674 and SD, multiple unpaired t-tests, * $p < 0.05$, $n = 2$), and **(f)** single-step exponential decay
675 curves were calculated, from which protein half-life was derived (means and SD, 2-way
676 ANOVA, *** $p < 0.0005$, ** $p < 0.005$, $n = 2$). **(g-h)** HEK-293T cells were transfected with equal
677 amounts of plasmids encoding the indicated MYC-mCherry-P2A-3xHA-tagged A3H-I mutants,
678 in which multiple lysine residues were mutated to arginine. 36 h. post transfection, cells were
679 treated with EPOX for 5 h., **(g)** protein levels determined by WB, and **(h)** quantified (means
680 and SD, multiple unpaired t-tests, **** $p < 0.0001$, * $p < 0.05$, $n = 3$).
681

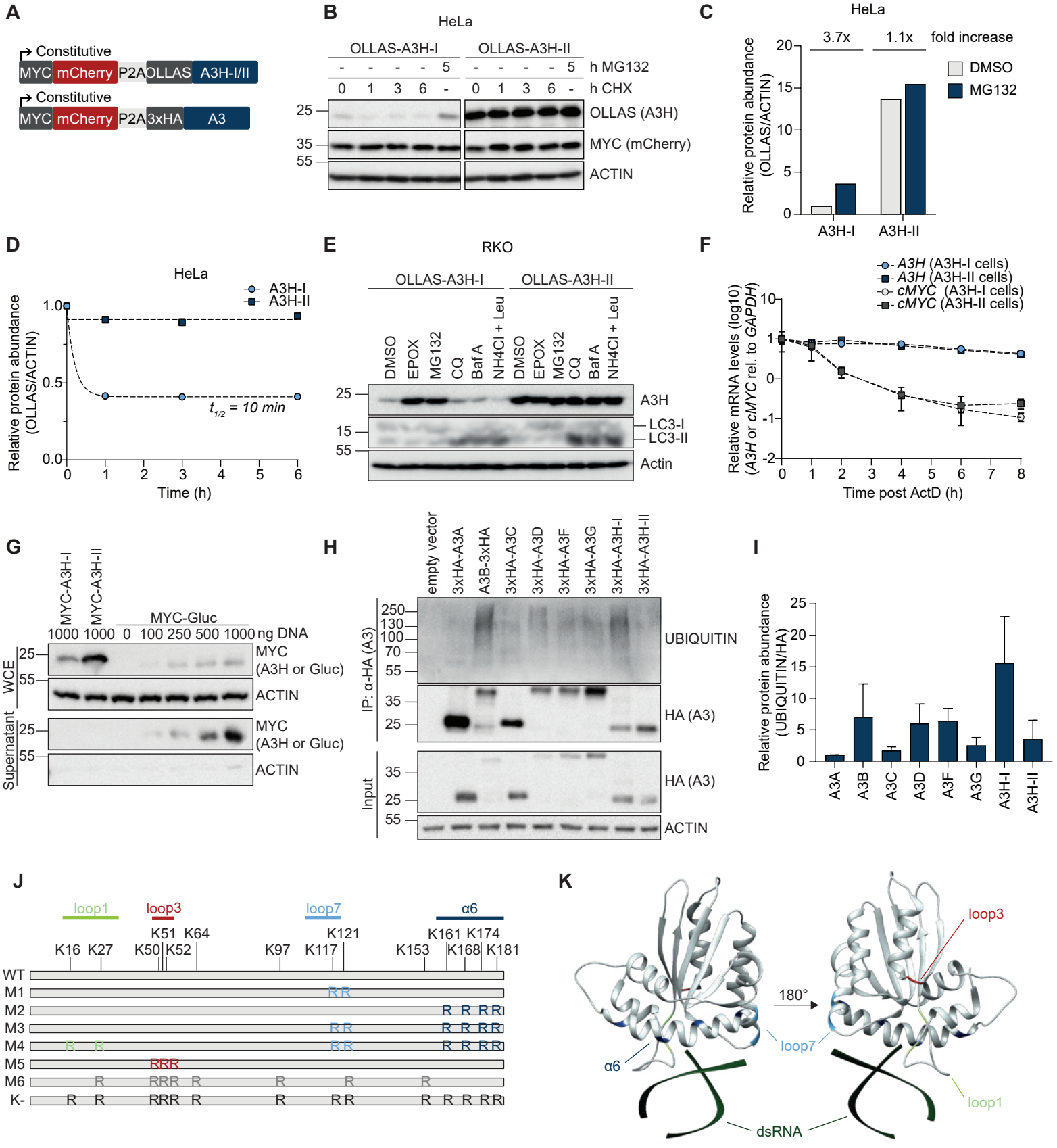
A
Constitutive
MYC mCherry P2A OLLAS A3H-I/II
Constitutive
MYC mCherry P2A 3xHA A3
B
HeLa
OLLAS-A3H-I
OLLAS-A3H-II
h MG132
h CHX
OLLAS (A3H)
MYC (mCherry)
ACTIN
C
HeLa
3.7x
1.1x
fold increase
DMSO
MG132
Relative protein abundance (OLLAS/ACTIN)
A3H-I
A3H-II
D
HeLa
A3H-I
A3H-II
Relative protein abundance (OLLAS/ACTIN)
$t_{1/2}$ = 10 min
Time (h)
E
RKO
OLLAS-A3H-I
OLLAS-A3H-II
DMSO
EPOX
MG132
CQ
Baf A
NH4Cl + Leu
A3H
LC3-I
LC3-II
Actin
F
A3H (A3H-I cells)
A3H (A3H-II cells)
cMYC (A3H-I cells)
cMYC (A3H-II cells)
Relative mRNA levels (log10) (A3H or cMYC rel. to GAPDH)
Time post ActD (h)
G
MYC-A3H-I
MYC-A3H-II
MYC-Gluc
1000 1000 0 100 250 500 1000 ng DNA
WCE
Supernatant
MYC (A3H or Gluc)
ACTIN
H
empty vector
3xHA-A3A
A3B-3xHA
3xHA-A3C
3xHA-A3D
3xHA-A3F
3xHA-A3G
3xHA-A3H-I
3xHA-A3H-II
IP: α-HA (A3)
Input
UBIQUITIN
HA (A3)
ACTIN
I
Relative protein abundance (UBIQUITIN/HA)
A3A
A3B
A3C
A3D
A3F
A3G
A3H-I
A3H-II
J
loop1
loop3
loop7
α6
K16 K27 K50 K51 K52 K64 K97 K117 K121 K153 K161 K168 K174 K181
WT
M1
M2
M3
M4
M5
M6
K-
K
loop3
180°
loop7
α6
loop1
dsRNA

682 **Figure S1. Proteasomal degradation controls protein levels of cancer-associated A3s.**
683 **(a)** Schematic representation of the lentiviral mCherry-P2A-OLLAS-A3 and mCherry-P2A-
684 3xHA-A3 expression constructs used in this study. The ribosomal skip site P2A ensures
685 equimolar translation of the stable internal control mCherry and tagged A3 protein. **(b-d)**
686 Lentiviral constructs encoding mCherry-P2A-OLLAS-A3H-I/II were stably integrated in HeLa
687 cells by lentiviral transduction. Polyclonal cell pools were treated with MG132 or CHX for the
688 indicated times, followed by **(b)** analysis of protein levels by WB, **(c)** quantification of relative
689 A3H-I and A3H-II protein levels upon proteasome inhibition, or **(d)** translation inhibition, by
690 calculating single-step exponential decay curves to derive protein half-live. **(e)** RKO cells
691 expressing the indicated OLLAS-tagged-A3H haplotypes were treated with different
692 proteasome inhibitors (EPOX, MG132), or autophagy/lysosomal degradation inhibitors
693 (chloroquine (CQ)), bafilomycin A (BafA), or leupeptin (Leu)) for 5 h. LC3-I to LC3-II conversion
694 was detected as a marker for inhibition of lysosomal degradation. **(f)** RKO cells stably
695 expressing OLLAS-A3H were treated for the indicated times with Actinomycin D (ActD), after
696 which relative exogenous *APOBEC3H* and endogenous *cMYC* mRNA levels were quantified
697 by RT-qPCR. **(g)** HEK-293T cells were transfected with plasmids encoding MYC-tagged A3H-
698 I/II or Gaussia luciferase (MYC-Gluc). 48 h. post transfection, MYC-tagged protein levels in the
699 supernatant and the whole cell extract (WCE) were analyzed by WB. **(h-i)** HEK-293T cells
700 were transfected with different amounts of the indicated 3xHA-A3 plasmids to achieve similar
701 steady-state A3 protein levels. After treatment with EPOX for 5 h., 3xHA-tagged proteins were
702 immunoprecipitated from cell lysates, and their ubiquitination analyzed by **(h)** WB with a total
703 ubiquitin antibody, and **(i)** quantified (means and SD, n = 4). **(j)** Schematic representation of
704 lysine positions in A3H-I. Lysine residues were systematically grouped based on their proximity
705 in the A3H structure and mutated to arginine (M1-M6). In K-, all 14 lysine residues were
706 mutated to arginine. **(k)** The positions of the mutated lysine residues in the A3H-II crystal
707 structure are highlighted in different colors (PDB: 6B0B).

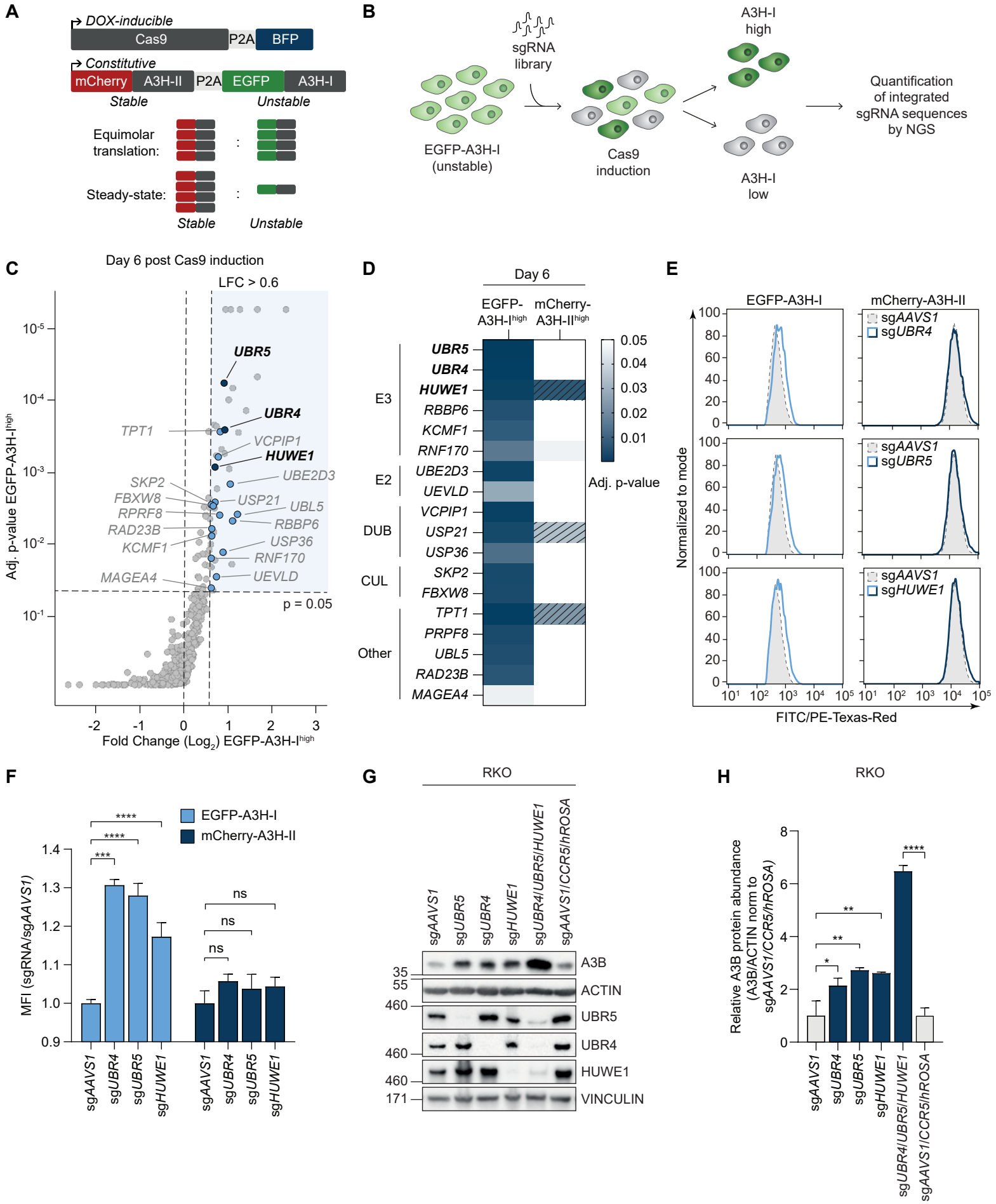
A
DOX-inducible
Cas9
P2A
BFP
Constitutive
mCherry
A3H-II
P2A
EGFP
A3H-I
Stable
Unstable
Equimolar translation:
Steady-state:
Stable
Unstable
B
sgRNA library
EGFP-A3H-I (unstable)
Cas9 induction
A3H-I high
A3H-I low
Quantification of integrated sgRNA sequences by NGS
C
Day 6 post Cas9 induction
LFC > 0.6
p = 0.05
UBR5
UBR4
TPT1
VCPIP1
HUWE1
UBE2D3
SKP2
FBXW8
USP21
UBL5
RPRF8
RBBP6
RAD23B
USP36
KCMF1
RNF170
MAGEA4
UEVLD
Adj. p-value EGFP-A3H-I^high
Fold Change (Log2) EGFP-A3H-I^high
D
Day 6
EGFP-A3H-I^high
mCherry-A3H-II^high
E3
E2
DUB
CUL
Other
UBR5
UBR4
HUWE1
RBBP6
KCMF1
RNF170
UBE2D3
UEVLD
VCPIP1
USP21
USP36
SKP2
FBXW8
TPT1
PRPF8
UBL5
RAD23B
MAGEA4
Adj. p-value
E
EGFP-A3H-I
mCherry-A3H-II
sgAAVS1
sgUBR4
sgUBR5
sgHUWE1
Normalized to mode
FITC/PE-Texas-Red
F
EGFP-A3H-I
mCherry-A3H-II
MFI (sgRNA/sgAAVS1)
sgAAVS1
sgUBR4
sgUBR5
sgHUWE1
ns
G
RKO
sgAAVS1
sgUBR5
sgUBR4
sgHUWE1
sgUBR4/UBR5/HUWE1
sgAAVS1/CCR5/hROSA
A3B
ACTIN
UBR5
UBR4
HUWE1
VINCULIN
H
RKO
Relative A3B protein abundance (A3B/ACTIN norm to sgAAVS1/CCR5/hROSA)
sgAAVS1
sgUBR4
sgUBR5
sgHUWE1
sgUBR4/UBR5/HUWE1
sgAAVS1/CCR5/hROSA

Figure 2. The E3 ligases UBR4, UBR5, and HUWE1 independently mediate turnover of A3B and A3H-I. (a) A monoclonal RKO cell line harboring a DOX-inducible Cas9-P2A-BFP expression construct and a constitutively expressed mCherry-A3H-II-P2A-EGFP-A3H-I dual-reporter (RKO-DOX-Cas9-dualA3H) was established. Unstable EGFP-A3H-I and stable-mCherry-A3H-II are synthesized in equimolar amounts, yet EGFP-A3H-I accumulates at low steady-state levels due to proteasomal degradation. **(b)** Schematic representation of CRISPR/Cas9 FACS-based screening procedure. RKO-DOX-Cas9-dualA3H cells were transduced with an sgRNA library targeted at ubiquitin-proteasome- and autophagy-linked factors. After selection of sgRNA-positive cells with G418, Cas9 expression was induced with DOX for 3 and 6 days, followed by sorting of cells with the 1-2% highest and lowest EGFP or mCherry fluorescence by flow cytometry. Integrated sgRNA sequences were identified by next generation sequencing (NGS), and their differential abundance relative to non-sorted cells analyzed. **(c)** Targeted genes enriched in EGFP-A3H-I^{high} sorted cell populations 6 days post Cas9 induction. **(d)** Heatmap of top genes on $\log_2$ fold-change and p-value grouped by functional categories. Genes enriched in EGFP-A3H-I^{high} cell populations 6 days post Cas9 induction with a $\log_2$ fold-change >0.6 which were not enriched in mCherry^{high} or GFP^{low} on either day 3 (LFC > 0.45) or day 6 (LFC > 0.6). Adjusted p-values are based on MaGECK analysis of three independent replicate sorts. Dashed lines indicate a $\log_2$ fold-change < 0.6. E3 (E3 ligases), E2 (E2 conjugating enzymes), DUB (Deubiquitinases), CUL (components of Cullin-RING ubiquitin ligase complex). **(e)** Monoclonal RKO-Dox-Cas9-dualA3H cells were transduced with individual sgRNAs targeting the indicated genes. Subsequently, Cas9 expression was induced by DOX for 6 days and EGFP-A3H-I and mCherry-A3H-II mean fluorescence intensity (MFI) analyzed by flow cytometry, and **(f)** quantified (means and SD, one-way ANOVA, **** $p < 0.0001$, *** $p < 0.0005$, $n = 3$). **(g)** RKO cells harboring DOX-inducible Cas9 were transduced with sgRNAs targeting *UBR4*, *UBR5*, or *HUWE1,* individually or in combination, and sorted for sgRNA-positive cells. Gene editing was induced with DOX for 6 days, after which endogenous A3B protein levels were determined by WB, and **(h)** quantified (means and SD, one-way ANOVA, **** $p < 0.0001$, ** $p < 0.005$, * $p < 0.05$, $n = 2$).

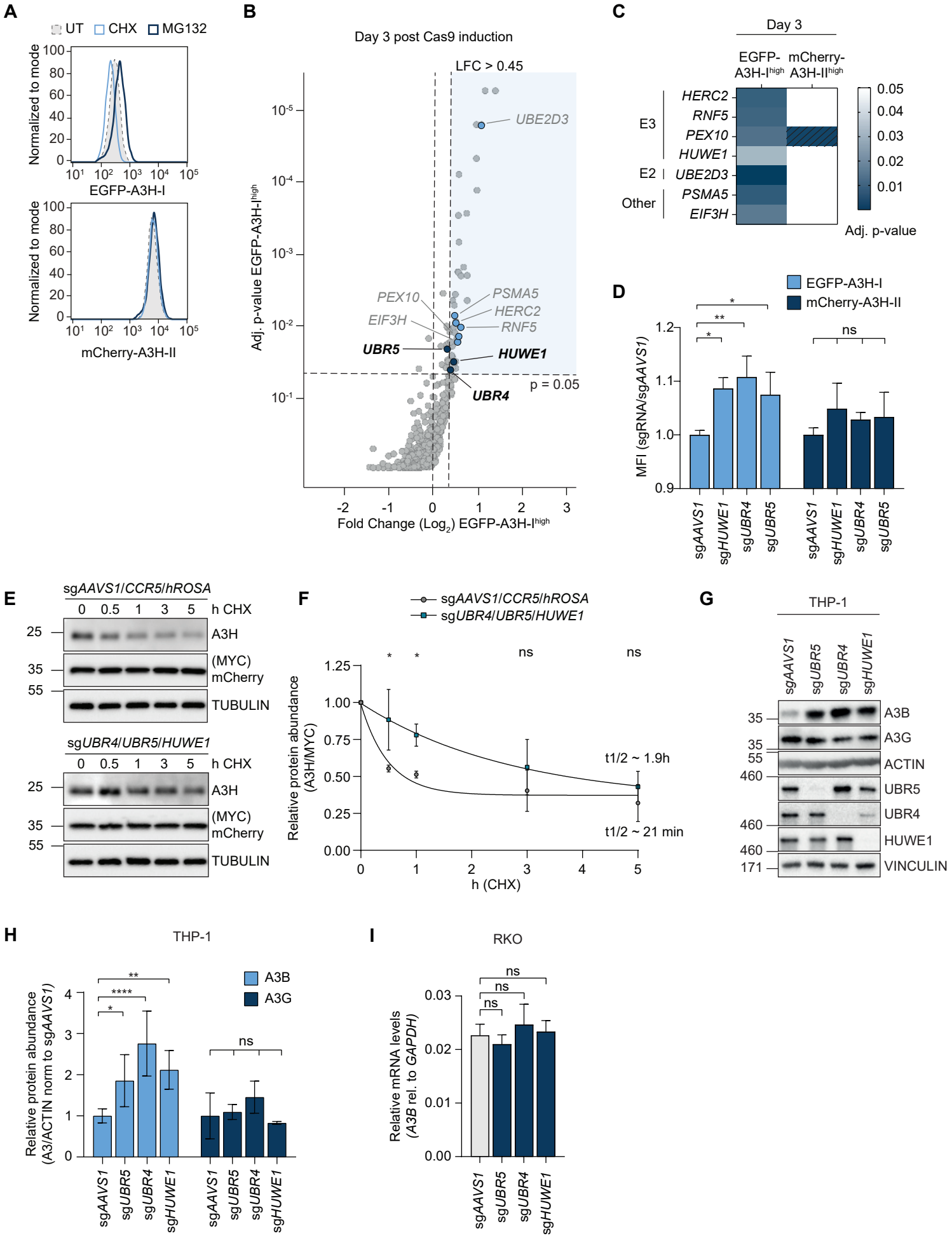
A
UT
CHX
MG132
Normalized to mode
EGFP-A3H-I
mCherry-A3H-II
B
Day 3 post Cas9 induction
LFC > 0.45
UBE2D3
PEX10
EIF3H
PSMA5
HERC2
RNF5
UBR5
HUWE1
UBR4
p = 0.05
Adj. p-value EGFP-A3H-I^high
Fold Change (Log2) EGFP-A3H-I^high
C
Day 3
EGFP-A3H-I^high
mCherry-A3H-II^high
E3
E2
Other
HERC2
RNF5
PEX10
HUWE1
UBE2D3
PSMA5
EIF3H
Adj. p-value
D
EGFP-A3H-I
mCherry-A3H-II
MFI (sgRNA/sgAAVS1)
ns
sgAAVS1
sgHUWE1
sgUBR4
sgUBR5
E
sgAAVS1/CCR5/hROSA
h CHX
A3H
(MYC) mCherry
TUBULIN
sgUBR4/UBR5/HUWE1
F
sgAAVS1/CCR5/hROSA
sgUBR4/UBR5/HUWE1
Relative protein abundance (A3H/MYC)
t1/2 ~ 1.9h
t1/2 ~ 21 min
h (CHX)
G
THP-1
A3B
A3G
ACTIN
UBR5
UBR4
HUWE1
VINCULIN
H
THP-1
A3B
A3G
Relative protein abundance (A3/ACTIN norm to sgAAVS1)
I
RKO
Relative mRNA levels (A3B rel. to GAPDH)

Figure S2. The E3 ligases UBR4, UBR5, and HUWE1 independently mediate turnover of A3B and A3H-I. (a) Monoclonal RKO-DOX-Cas9-dualA3H cells were treated with CHX or EPOX for 5 h., followed by analysis of EGFP-A3H-I or mCherry-A3H-II levels by flow cytometry. **(b)** Targeted genes enriched in EGFP-A3H-I^{high} sorted cell populations 3 days post Cas9 induction. **(c)** Heatmap of top genes on $\log_2$ fold-change and p-value grouped by functional categories. Genes enriched in EGFP-A3H-I^{high} cell populations 3 days post Cas9 induction with a $\log_2$ fold-change > 0.45 which were not enriched in mCherry^{high} or GFP^{low} on the same day. Dashed lines indicate a $\log_2$ fold-change < 0.45. Adjusted p-values are based on MaGECK analysis of three independent replicate sorts. E3 (E3 ligases), E2 (E2 conjungating enzymes). **(d)** Polyclonal RKO-DOX-Cas9-dualA3H cells were transduced with sgRNA vectors targeting *UBR4*, *UBR5*, or *HUWE1*. EGFP-A3H-I and mCherry-A3H-II abundance was analyzed by flow cytometry 6 days after Cas9 induction. The mean fluorescence intensity (MFI) was quantified (one-way ANOVA compared to sg*AAVS1*, ** $p < 0.005$, * $p < 0.05$, $n = 3$). **(e)** RKO-DOX-Cas9-MYC-mCherry-P2A-3xHA-A3H-I cells were transduced with sgRNA simultaneously targeting either the three E3 ligases or control loci (*AAVS1*, *CCR5*, *hROSA*), gene editing induced with DOX for 6 days and then treated with CHX for different times. A3H-I protein levels were determined by WB and **(f)** the half-life quantified from single-step exponential decay curves, statistics were calculated by two-way ANOVA, * $p < 0.05$ ($n = 3$). **(g)** THP-1 cells harboring DOX-inducible Cas9 were transduced with sgRNAs targeting *UBR4*, *UBR5*, or *HUWE1*, and sorted for sgRNA-positive cells. Gene editing was induced with DOX for 3 days, after which endogenous A3B and A3G protein levels were determined by WB, and **(h)** quantified (means and SD, two-way ANOVA, **** $p < 0.0001$, *** $p < 0.0005$, ** $p < 0.005$, * $p < 0.05$, $n = 4$). **(i)** RKO cells harboring DOX-inducible Cas9 were transduced with sgRNAs targeting *UBR4*, *UBR5*, or *HUWE1*, and sorted for sgRNA-positive cells. Gene editing was induced with DOX for 6 days, after which endogenous *A3B* mRNA levels were determined by RT-qPCR (means and SD, one-way ANOVA, ns $p > 0.1$, $n = 3$).

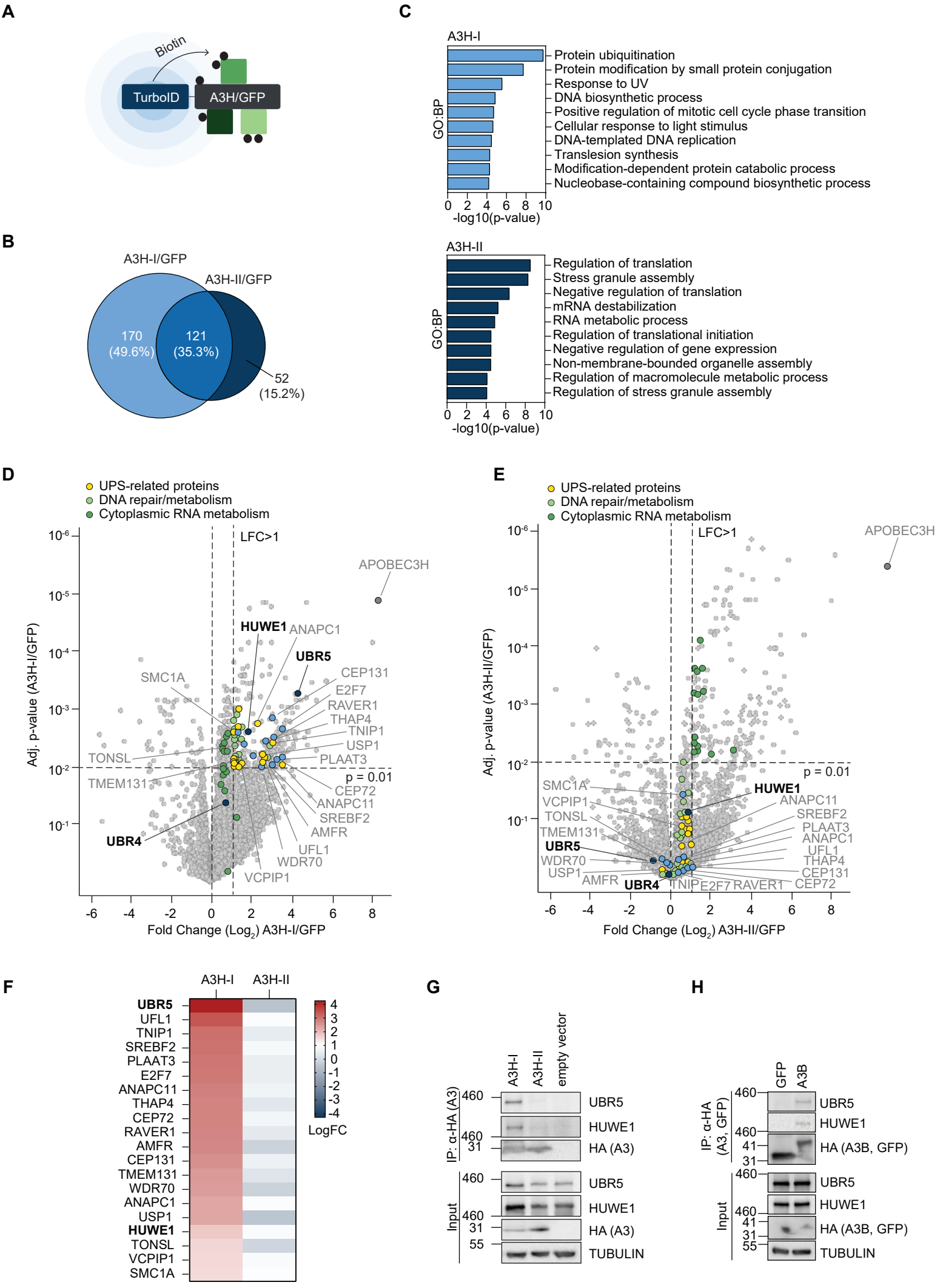
A
Biotin
TurboID
A3H/GFP
B
A3H-I/GFP
A3H-II/GFP
170
(49.6%)
121
(35.3%)
52
(15.2%)
C
A3H-I
GO:BP
Protein ubiquitination
Protein modification by small protein conjugation
Response to UV
DNA biosynthetic process
Positive regulation of mitotic cell cycle phase transition
Cellular response to light stimulus
DNA-templated DNA replication
Translesion synthesis
Modification-dependent protein catabolic process
Nucleobase-containing compound biosynthetic process
-log10(p-value)
A3H-II
Regulation of translation
Stress granule assembly
Negative regulation of translation
mRNA destabilization
RNA metabolic process
Regulation of translational initiation
Negative regulation of gene expression
Non-membrane-bounded organelle assembly
Regulation of macromolecule metabolic process
Regulation of stress granule assembly
D
UPS-related proteins
DNA repair/metabolism
Cytoplasmic RNA metabolism
LFC>1
APOBEC3H
HUWE1
ANAPC1
UBR5
CEP131
E2F7
RAVER1
THAP4
TNIP1
USP1
PLAAT3
SMC1A
TONSL
TMEM131
UBR4
p = 0.01
CEP72
ANAPC11
SREBF2
AMFR
UFL1
WDR70
VCPIP1
Adj. p-value (A3H-I/GFP)
Fold Change (Log2) A3H-I/GFP
E
UPS-related proteins
DNA repair/metabolism
Cytoplasmic RNA metabolism
LFC>1
APOBEC3H
p = 0.01
SMC1A
VCPIP1
TONSL
TMEM131
UBR5
WDR70
USP1
AMFR
UBR4
TNIP
E2F7
RAVER1
CEP72
HUWE1
ANAPC11
SREBF2
PLAAT3
ANAPC1
UFL1
THAP4
CEP131
Adj. p-value (A3H-II/GFP)
Fold Change (Log2) A3H-II/GFP
F
A3H-I
A3H-II
UBR5
UFL1
TNIP1
SREBF2
PLAAT3
E2F7
ANAPC11
THAP4
CEP72
RAVER1
AMFR
CEP131
TMEM131
WDR70
ANAPC1
USP1
HUWE1
TONSL
VCPIP1
SMC1A
LogFC
G
A3H-I
A3H-II
empty vector
IP: α-HA (A3)
Input
UBR5
HUWE1
HA (A3)
TUBULIN
H
GFP
A3B
IP: α-HA (A3, GFP)
Input
UBR5
HUWE1
HA (A3B, GFP)
TUBULIN

763 **Figure 3. UBR5 and HUWE1 form a complex with A3H-I and other unstable A3**
764 **deaminases in cells. (a)** Overview of TurboID proximity labeling principle. **(b)** Polyclonal
765 RKO-DOX-TID-A3H-I/II/GFP were treated with different concentrations of DOX for 2 days to
766 achieve similar protein levels. Subsequently, cells were treated with EPOX for 5 h. and the
767 culture media supplemented with biotin during the last 15 min. Biotinylated proteins were
768 purified under denaturing conditions and quantified by nLC-MS/MS. Differentially enriched
769 proteins in A3H-I/GFP (light blue, LFC > 1, p-value < 0.01) and A3H-II/GFP (dark blue, LFC >
770 1, p-value < 0.01) were compared. **(c)** GO terms for biological processes (GO:BP) of
771 differentially enriched proteins in A3H-I/GFP (light blue, LFC > 1, p-value < 0.01, input: 170
772 factors derived from (b)) and A3H-II/GFP (dark blue, LFC > 1, p-value < 0.01, input: 52 factors
773 derived from (b)). **(d)** Differential expression of TID-A3H-I, or **(e)** TID-A3H-II interactors relative
774 to TID-GFP (n = 3). Proteins specifically enriched for either A3H-I or A3H-II identified in (a) are
775 indicated in color. **(f)** Heatmap representation of enriched proteins in TID-A3H-I samples, or
776 TID-A3H-II samples relative to TID-GFP. Top 20 A3H-I-specific proteins displayed according
777 to the following criteria: A3H-I/GFP LFC > 1, p-value < 0.01, which are not enriched in A3H-
778 II/GFP LFC > 1, p-value < 0.01. **(g-h)** HEK-293T cells were transiently transfected with different
779 amounts of plasmids encoding **(g)** 3xHA-A3H-I/II, or **(h)** 3xHA-GFP or A3B-3xHA to achieve
780 similar steady-state protein levels. Subsequently, 3xHA-tagged proteins were
781 immunoprecipitated, and their interaction with endogenous UBR5 and HUWE1 determined by
782 WB.
783

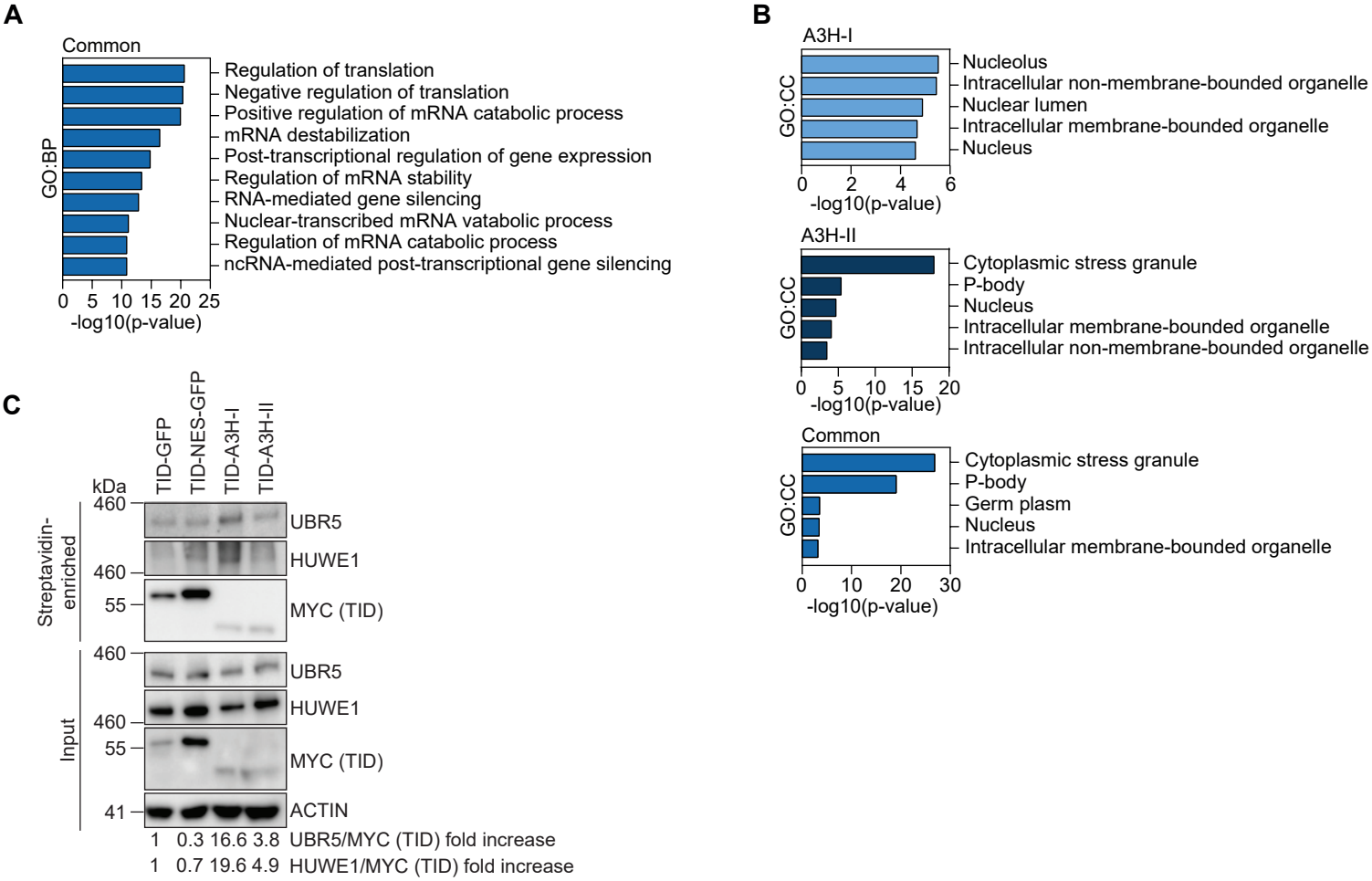
A
Common
GO:BP
Regulation of translation
Negative regulation of translation
Positive regulation of mRNA catabolic process
mRNA destabilization
Post-transcriptional regulation of gene expression
Regulation of mRNA stability
RNA-mediated gene silencing
Nuclear-transcribed mRNA vatabolic process
Regulation of mRNA catabolic process
ncRNA-mediated post-transcriptional gene silencing
0 5 10 15 20 25
-log10(p-value)
B
A3H-I
GO:CC
Nucleolus
Intracellular non-membrane-bounded organelle
Nuclear lumen
Intracellular membrane-bounded organelle
Nucleus
0 2 4 6
-log10(p-value)
A3H-II
GO:CC
Cytoplasmic stress granule
P-body
Nucleus
Intracellular membrane-bounded organelle
Intracellular non-membrane-bounded organelle
0 5 10 15 20
-log10(p-value)
Common
GO:CC
Cytoplasmic stress granule
P-body
Germ plasm
Nucleus
Intracellular membrane-bounded organelle
0 10 20 30
-log10(p-value)
C
TID-GFP
TID-NES-GFP
TID-A3H-I
TID-A3H-II
kDa
Streptavidin-enriched
460
UBR5
HUWE1
460
55
MYC (TID)
Input
460
UBR5
HUWE1
460
55
MYC (TID)
41
ACTIN
1 0.3 16.6 3.8 UBR5/MYC (TID) fold increase
1 0.7 19.6 4.9 HUWE1/MYC (TID) fold increase

784 **Figure S3 UBR5 and HUWE1 form a complex with A3H-I and other unstable A3**
785 **deaminases in cells. (a)** GO terms for biological processes (GO:BP) of differentially enriched
786 proteins shared between A3H-I/GFP and A3H-II/GFP (LFC > 1, p-value < 0.01, input: 121
787 factors derived from Fig. 3b) **(b)** GO terms for cellular compartments (GO:CC) of differentially
788 enriched proteins in A3H-I/GFP (light blue, input: 170 factors derived from Fig. 3b), A3H-II/GFP
789 (dark blue, input: 52 factors derived from Fig. 3b) and proteins shared between both A3H-I and
790 A3H-II/GFP ("common", medium blue, input: 121 factors derived from Fig. 3b) (LFC > 1, p-
791 value < 0.01). **(c)** Polyclonal RKO-DOX-TID-A3H-I/II/GFP cells were treated with different
792 concentrations of DOX for two days to achieve similar protein levels. Subsequently, cells were
793 treated with EPOX for 5 h., during the last 15 min. of which, exogenous biotin was added to
794 the culture media. Biotinylated proteins were purified, and their interaction with endogenous
795 UBR5 and HUWE1 detected by WB. Relative abundance of UBR5/MYC (TID) or HUWE1/MYC
796 (TID) was quantified. Densitometry values are listed.

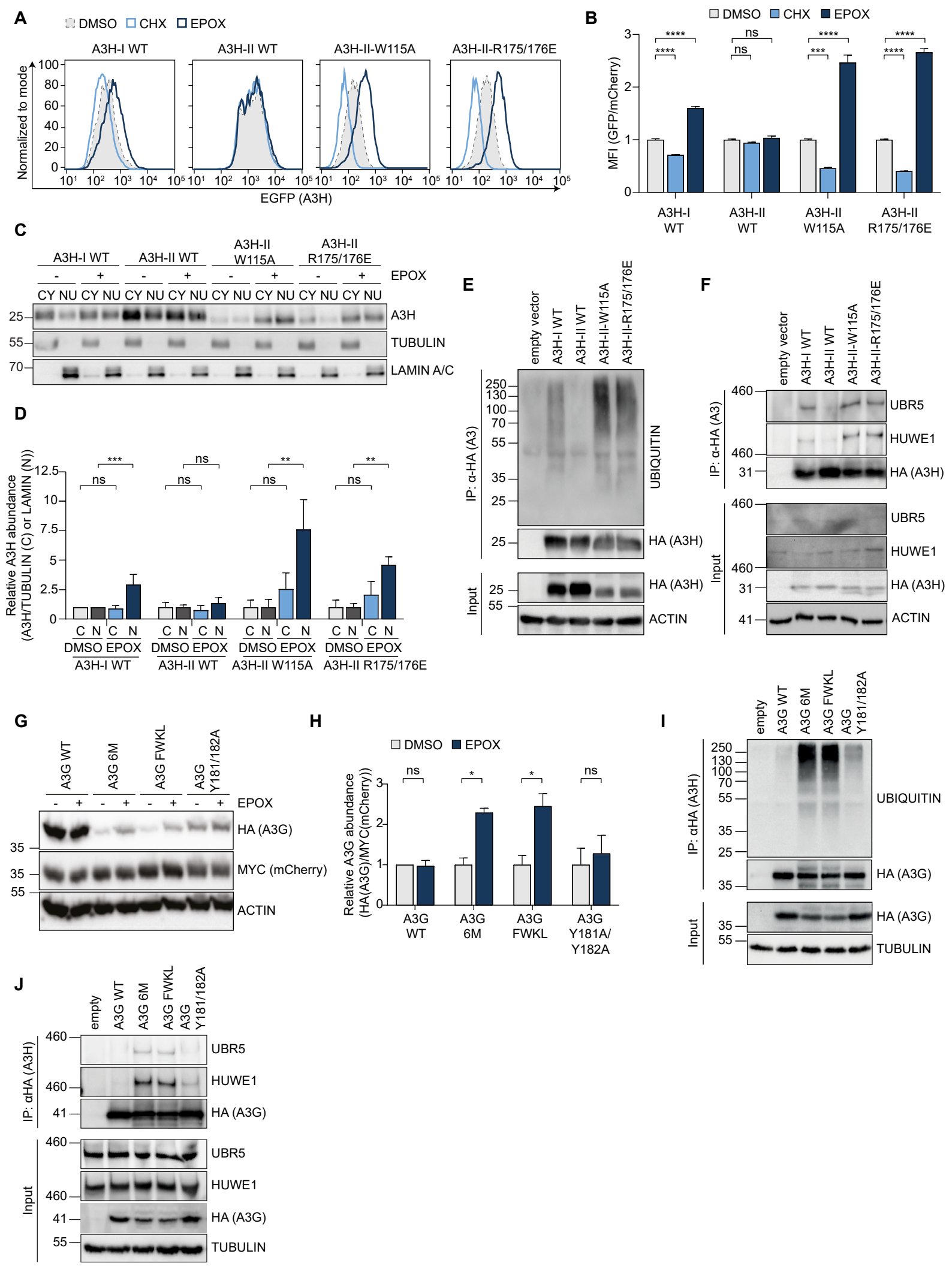
A
DMSO
CHX
EPOX
A3H-I WT
A3H-II WT
A3H-II-W115A
A3H-II-R175/176E
Normalized to mode
EGFP (A3H)
B
MFI (GFP/mCherry)
A3H-I WT
A3H-II WT
A3H-II W115A
A3H-II R175/176E
C
EPOX
CY NU
A3H
TUBULIN
LAMIN A/C
D
Relative A3H abundance (A3H/TUBULIN (C) or LAMIN (N))
DMSO EPOX
E
empty vector
IP: α-HA (A3)
UBIQUITIN
HA (A3H)
Input
ACTIN
F
UBR5
HUWE1
G
A3G WT
A3G 6M
A3G FWKL
A3G Y181/182A
HA (A3G)
MYC (mCherry)
H
Relative A3G abundance (HA(A3G)/MYC(mCherry))
I
IP: αHA (A3H)
J

Figure 4. RNA binding protects A3 from E3 ligase binding and ubiquitination, thus promoting stability in cells. (a) RKO-mCherry-P2A-EGFP-A3H cells expressing the indicated EGFP-tagged A3H variants were treated for 5 h. with EPOX or CHX, after which mCherry and EGFP-A3H abundances were measured by flow cytometry, and **(b)** the MFI quantified (means and SD, one-way ANOVA, **** $p < 0.0001$, *** $p < 0.0005$, $n = 3$). **(c)** HEK-293T cells were transfected with different amounts of plasmids expressing the indicated 3xHA-tagged A3H constructs to achieve similar steady-state protein levels. Following 5 h. of EPOX treatment, whole cell extracts (Fig. S4h), cytoplasmic (C) and nuclear (N) fractions were extracted, analyzed by WB, and **(d)** quantified (means and SD, one-way ANOVA; *** $p < 0.0005$, ** $p < 0.005$; $n = 3$). **(e-f)** HEK-293T cells were transfected with different amounts of plasmids expressing the indicated 3xHA-tagged A3H constructs to achieve similar protein levels. Following 5 h. of EPOX treatment, 3xHA-tagged proteins were immunoprecipitated, and **(e)** their ubiquitination or **(f)** interaction with UBR5 and HUWE1 analyzed by WB. **(g)** mCherry-P2A-3xHA-tagged A3G WT and A3G RNA-binding mutants (6M (F126Y, W127S, K180A, I183A, L184A, I187A), FWKL (F126Y, W127S, K180S, L184S) and Y181A/Y182A) were transiently expressed in HEK-293T cells, followed by 5 h. of EPOX treatment and analysis of protein levels by WB, and **(h)** quantified. Multiple unpaired t-tests, * $p < 0.05$; $n = 3$). **(i-j)** HEK-293T cells were transfected as in (g), but with different amounts of plasmid constructs to achieve similar steady-state protein levels, followed by EPOX treatment for 5 h. and immunoprecipitation of 3xHA-tagged proteins from the cell lysates. Their **(i)** ubiquitination, or **(j)** interaction with UBR5 and HUWE1 was analyzed by WB.

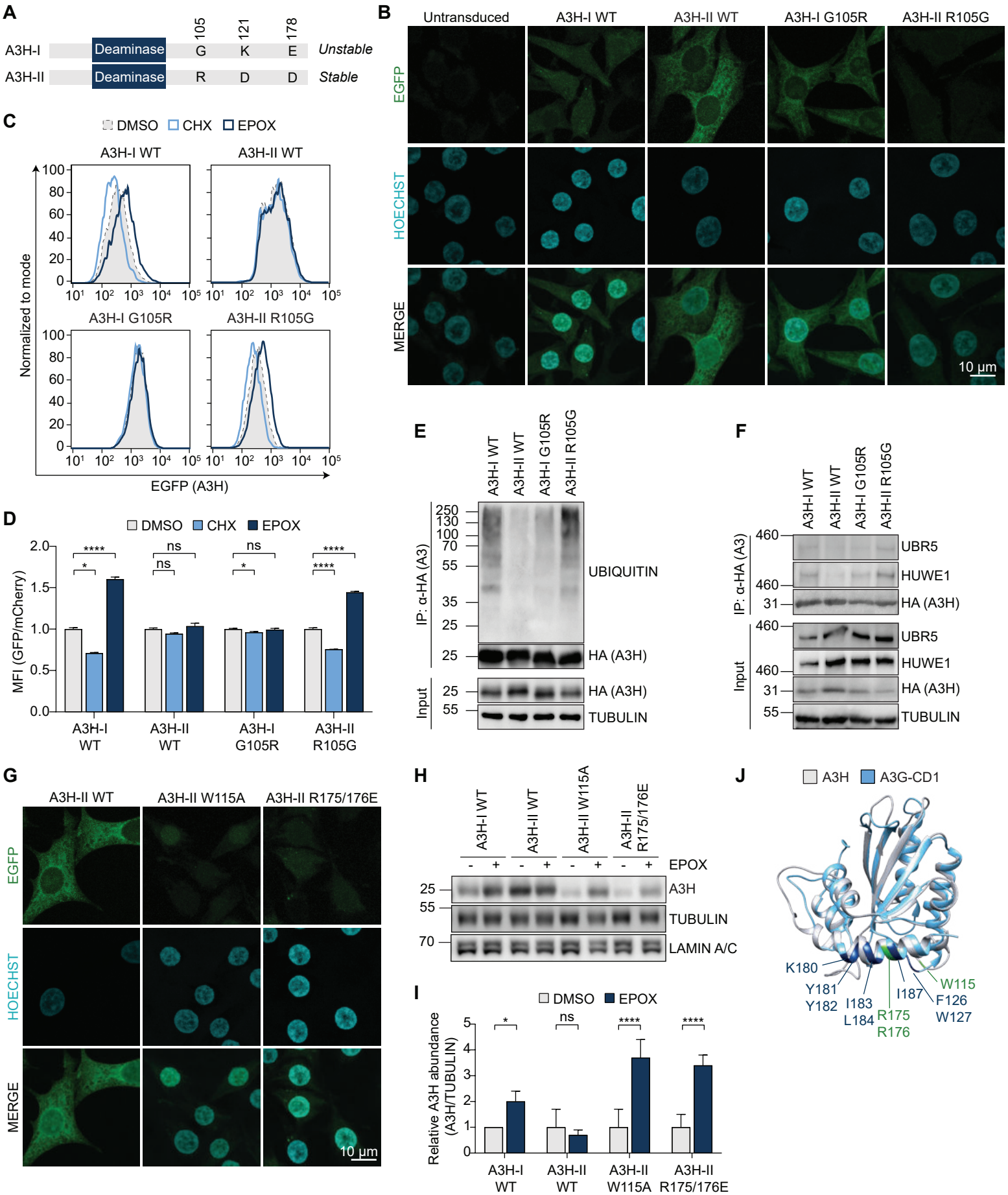
A
105
121
178
A3H-I
Deaminase
G
K
E
Unstable
A3H-II
Deaminase
R
D
D
Stable
B
Untransduced
A3H-I WT
A3H-II WT
A3H-I G105R
A3H-II R105G
EGFP
HOECHST
MERGE
10 µm
C
DMSO
CHX
EPOX
A3H-I WT
A3H-II WT
A3H-I G105R
A3H-II R105G
Normalized to mode
EGFP (A3H)
D
DMSO
CHX
EPOX
MFI (GFP/mCherry)
A3H-I WT
A3H-II WT
A3H-I G105R
A3H-II R105G
E
A3H-I WT
A3H-II WT
A3H-I G105R
A3H-II R105G
IP: α-HA (A3)
UBIQUITIN
HA (A3H)
Input
HA (A3H)
TUBULIN
F
A3H-I WT
A3H-II WT
A3H-I G105R
A3H-II R105G
IP: α-HA (A3)
UBR5
HUWE1
HA (A3H)
Input
UBR5
HUWE1
HA (A3H)
TUBULIN
G
A3H-II WT
A3H-II W115A
A3H-II R175/176E
EGFP
HOECHST
MERGE
10 µm
H
A3H-I WT
A3H-II WT
A3H-II W115A
A3H-II R175/176E
EPOX
A3H
TUBULIN
LAMIN A/C
I
DMSO
EPOX
Relative A3H abundance (A3H/TUBULIN)
A3H-I WT
A3H-II WT
A3H-II W115A
A3H-II R175/176E
J
A3H
A3G-CD1
K180
Y181
Y182
I183
L184
R175
R176
I187
W115
F126
W127

819 **Figure S4. RNA binding protects A3 from E3 ligase binding and ubiquitination, thus**
820 **promoting stability in cells. (a)** Schematic overview of the three differential amino acid
821 positions in A3H-I and A3H-II. **(b)** Confocal microscopy of RKO-mCherry-P2A-EGFP-A3H-
822 I/II/I-G105R/II-R105G cells. Maximum intensity projections of 11 slices are displayed (scale
823 bar = 10 µm). **(c-d)** RKO-mCherry-P2A-EGFP-A3H cells expressing the indicated EGFP-
824 tagged A3H variants were treated for 5 h. with EPOX or CHX, followed by measurement of
825 the mean fluorescence intensity (MFI) of EGFP-A3H by flow cytometry. **(d)** Quantification of
826 (c) (means and SD, one-way ANOVA, **** $p < 0.0001$, * $p < 0.05$ n = 3). **(e-f)** Different
827 amounts of the indicated 3xHA-A3H plasmids were transiently transfected in HEK-293T cells
828 to achieve similar steady-state A3 protein levels, followed by 5 h. of EPOX treatment and
829 immunoprecipitation of 3xHA-tagged proteins from the cell lysates. Their **(e)** ubiquitination or
830 **(f)** interaction with UBR5 and HUWE1 was analyzed by WB. **(g)** Confocal microscopy of
831 RKO-mCherry-P2A-EGFP-A3H cells expressing the indicated EGFP-tagged A3H variants.
832 Maximum intensity projections of 11 slices are displayed (scale bar = 10 µm). **(h)** Whole cell
833 extract samples corresponding to Fig. 4c. **(i)** Quantification of (h) (multiple unpaired t-tests,
834 **** $p < 0.0001$, * $p < 0.05$; n = 3). **(j)** Structural alignment of A3H-II (PDB:6B0B) and A3G-
835 CD1 (PDB: 5K81). Relevant amino acid residues mutated in the various RNA-binding
836 mutants are colored in green (A3H-II) or dark blue (A3G).

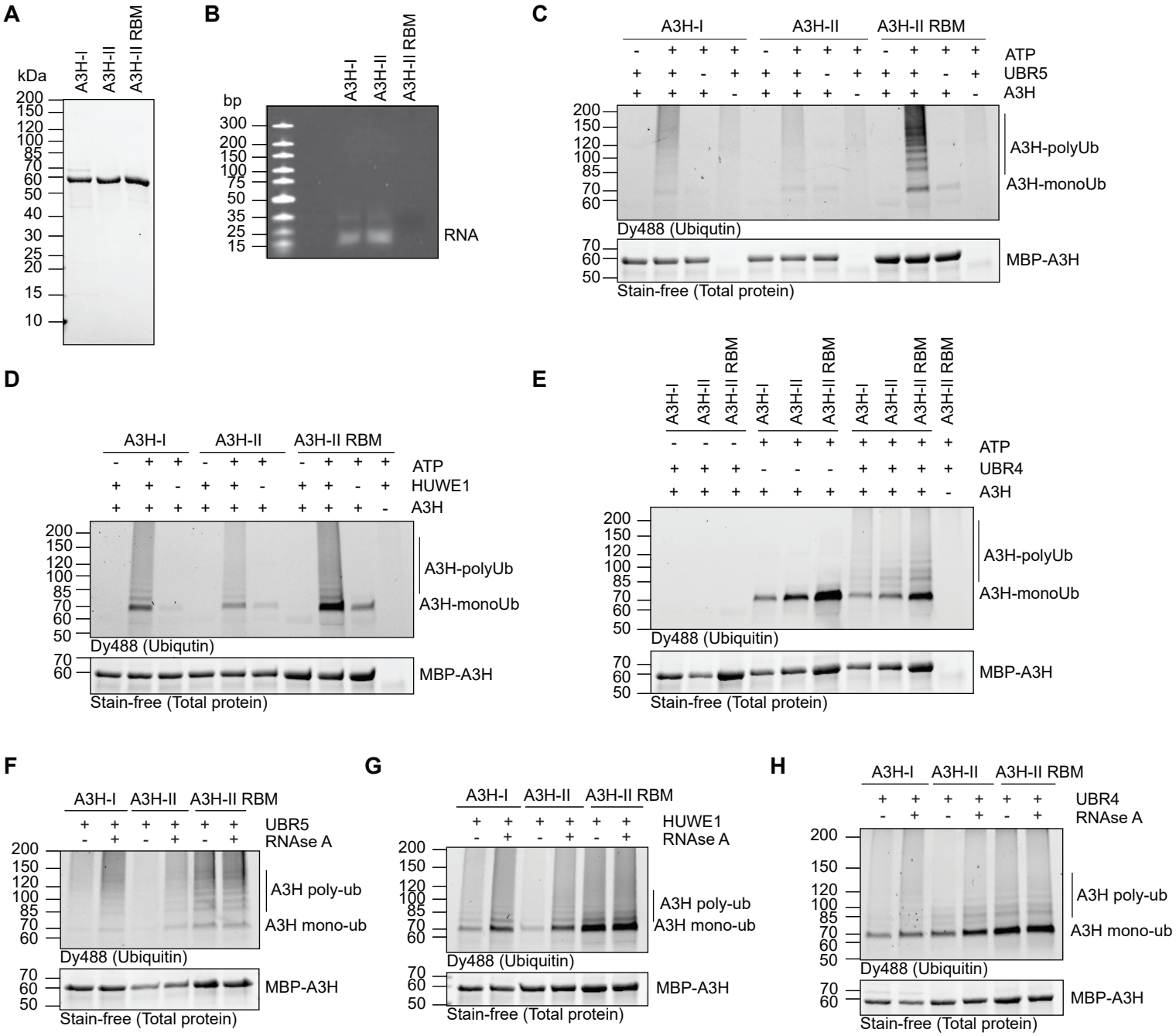
A
kDa
A3H-I
A3H-II
A3H-II RBM
200
150
120
100
85
70
60
50
40
30
25
20
15
10
B
bp
A3H-I
A3H-II
A3H-II RBM
300
200
150
100
75
50
35
25
15
RNA
C
A3H-I
A3H-II
A3H-II RBM
ATP
UBR5
A3H
A3H-polyUb
A3H-monoUb
Dy488 (Ubiqutin)
MBP-A3H
Stain-free (Total protein)
D
A3H-I
A3H-II
A3H-II RBM
ATP
HUWE1
A3H
A3H-polyUb
A3H-monoUb
Dy488 (Ubiqutin)
MBP-A3H
Stain-free (Total protein)
E
A3H-I
A3H-II
A3H-II RBM
ATP
UBR4
A3H
A3H-polyUb
A3H-monoUb
Dy488 (Ubiquitin)
MBP-A3H
Stain-free (Total protein)
F
A3H-I
A3H-II
A3H-II RBM
UBR5
RNAse A
A3H poly-ub
A3H mono-ub
Dy488 (Ubiquitin)
MBP-A3H
Stain-free (Total protein)
G
A3H-I
A3H-II
A3H-II RBM
HUWE1
RNAse A
A3H poly-ub
A3H mono-ub
Dy488 (Ubiquitin)
MBP-A3H
Stain-free (Total protein)
H
A3H-I
A3H-II
A3H-II RBM
UBR4
RNAse A
A3H poly-ub
A3H mono-ub
Dy488 (Ubiquitin)
MBP-A3H
Stain-free (Total protein)

837 **Figure 5. RNA binding by APOBEC3 proteins prevents their recognition and**
838 **ubiquitination by E3 ligases *in vitro*. (a)** 10x-His-MBP-A3H-I, 10x-His-MBP-A3H-II and
839 10xHis-MBP-A3H-II-RBM (E56A/ W115A/ R175E/ R176E) were expressed in *E. coli*, purified
840 by HisTrap and subsequent gel filtration, after which purified proteins were analyzed by PAGE
841 and Coomassie staining. **b)** Purified proteins were analyzed by denaturing Urea-TBE PAGE
842 followed by SYBR Gold staining. **(c-e)** *In vitro* ubiquitination assays were performed with
843 recombinant **(c)** UBR5, **(d)** HUWE1, or **(e)** UBR4 and WT A3H-I/II or A3H-RBM as substrates,
844 and in the presence of DyLight488-labeled recombinant ubiquitin. Subsequently, A3H was
845 immunoprecipitated using anti-MBP-coupled beads and the ubiquitination pattern visualized
846 by fluorescent imaging for DyLight488. **f-h)** *In vitro* ubiquitination assay with recombinant **f)**
847 UBR5, **g)** HUWE1, **h)** UBR4 and A3H-I/II WT or A3H-RBM in the absence or presence of
848 RNase A. Ubiquitinated A3H was visualized as in (c-e).
849

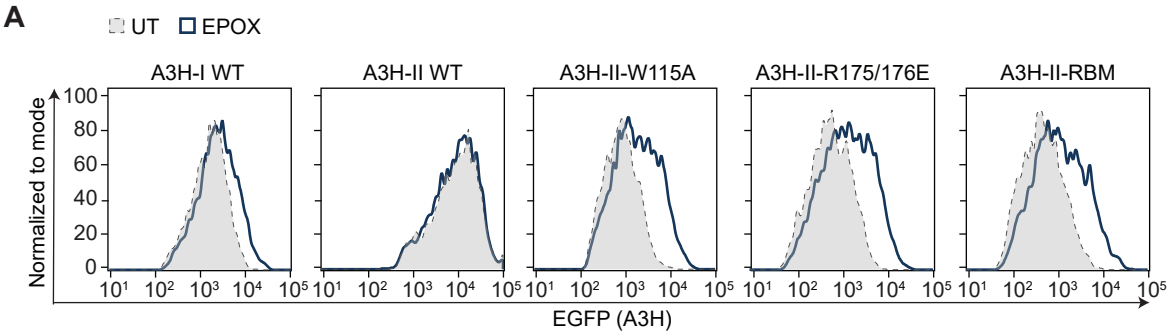
A
UT
EPOX
A3H-I WT
A3H-II WT
A3H-II-W115A
A3H-II-R175/176E
A3H-II-RBM
Normalized to mode
EGFP (A3H)

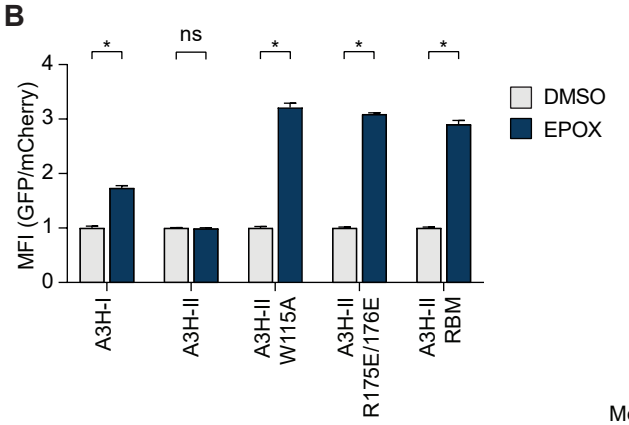
B
MFI (GFP/mCherry)
ns
DMSO
EPOX
A3H-I
A3H-II
A3H-II W115A
A3H-II R175E/176E
A3H-II RBM

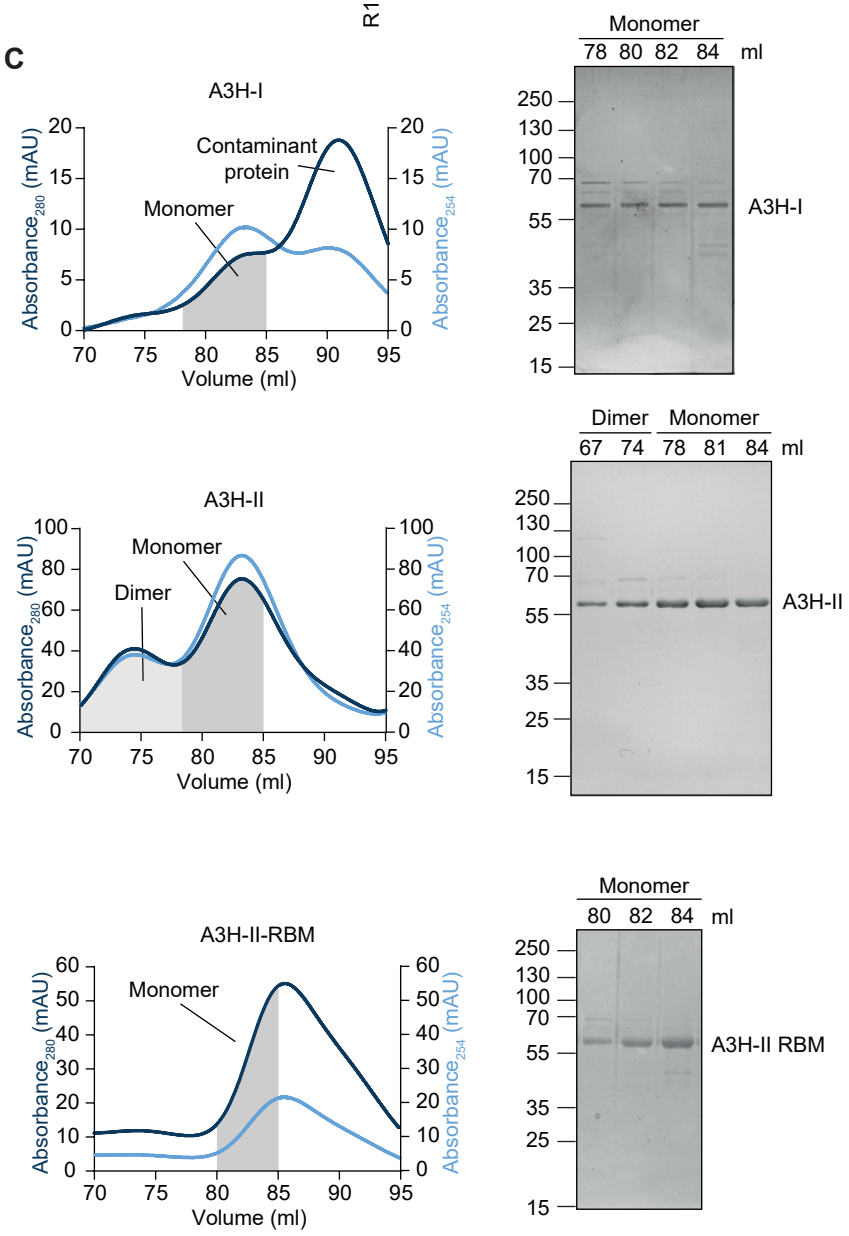
C
A3H-I
Contaminant protein
Monomer
Absorbance280 (mAU)
Absorbance254 (mAU)
Volume (ml)
Monomer
78 80 82 84 ml
A3H-I
A3H-II
Monomer
Dimer
Dimer Monomer
67 74 78 81 84 ml
A3H-II
A3H-II-RBM
Monomer
Monomer
80 82 84 ml
A3H-II RBM

850 **Figure S5. RNA binding by APOBEC3 proteins prevents their recognition and**
851 **ubiquitination by E3 ligases *in vitro*. (a-b)** HEK-293T cells were transiently transfected with
852 EGFP-tagged A3H-I/II or A3H-II-RBM. After 48 h., cells were treated with EPOX for 5 h.,
853 followed by **(a)** measurement of EGFP-A3H fluorescence by flow cytometry, and **b)** followed
854 by subsequent quantification (multiple unpaired t-tests, * $p < 0.05$, $n = 3$). **(c)** SEC profiles of
855 10x-His-MBP-A3H-I, 10x-His-MBP-A3H-II and 10x-His-MBP-A3H-II-RBM. Dark blue lines
856 depict the absorbance at 280 nm representing eluted protein, light blue lines at 254 nm
857 representing nucleic acid bound to the protein. Monomeric or dimeric fractions were pooled
858 separately and analyzed by Coomassie stained SDS PAGE (right insets).

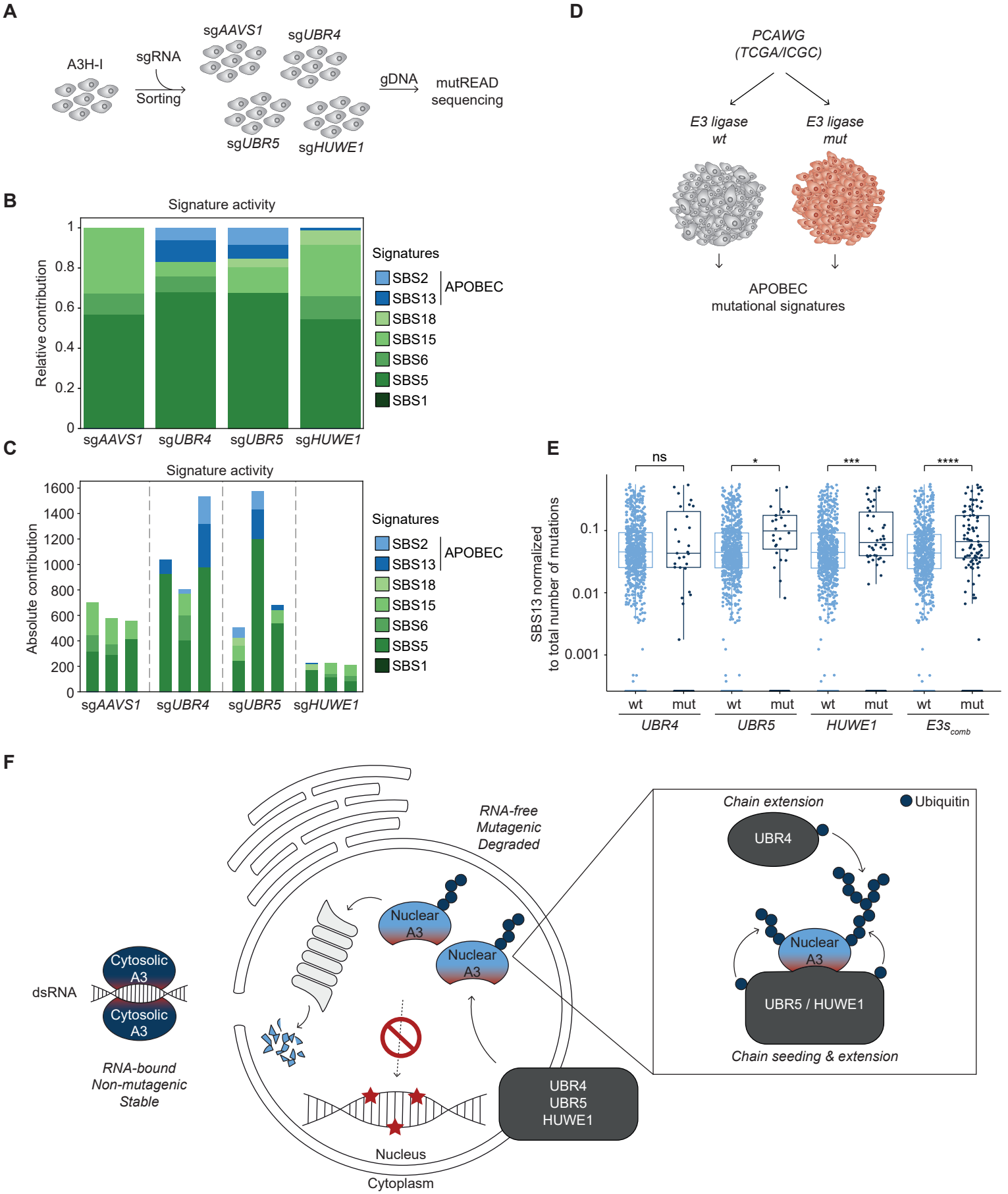
A
A3H-I
sgRNA
Sorting
sgAAVS1
sgUBR4
sgUBR5
sgHUWE1
gDNA
mutREAD sequencing
B
Signature activity
Relative contribution
Signatures
SBS2
SBS13
APOBEC
SBS18
SBS15
SBS6
SBS5
SBS1
sgAAVS1
sgUBR4
sgUBR5
sgHUWE1
C
Signature activity
Absolute contribution
Signatures
SBS2
SBS13
APOBEC
SBS18
SBS15
SBS6
SBS5
SBS1
sgAAVS1
sgUBR4
sgUBR5
sgHUWE1
D
PCAWG (TCGA/ICGC)
E3 ligase wt
E3 ligase mut
APOBEC mutational signatures
E
SBS13 normalized to total number of mutations
ns
*
***
****
wt
mut
UBR4
UBR5
HUWE1
E3s comb
F
RNA-free Mutagenic Degraded
Cytosolic A3
dsRNA
Cytosolic A3
RNA-bound Non-mutagenic Stable
Nuclear A3
Nuclear A3
UBR4 UBR5 HUWE1
Nucleus
Cytoplasm
Chain extension
Ubiquitin
UBR4
Nuclear A3
UBR5 / HUWE1
Chain seeding & extension

Figure 6. E3 ligase loss or mutation increases APOBEC signature mutations. (a) Schematic representation of mutREAD sequencing to identify APOBEC signature mutations in cells. A *UNG2*$^{-/-}$ RKO cell line expressing DOX-inducible Cas9 and mCherry-P2A-3xHA-A3H-I was transduced with sgRNAs targeting *UBR4*, *UBR5*, or *HUWE1*, and subsequently sorted for sgRNA-positive cells. Gene editing was induced with DOX for up to four cell doublings, after which gDNA was isolated and samples prepared for mutREAD sequencing. **(b-c)** Best subset signature refitting of mutREAD data, averaged per genotype, using signatures related to overactivity of APOBEC family enzymes and signatures commonly active in colon carcinoma, the parent tumor type for the model cell line RKO. For the purpose of comparing signature activity across genotypes, samples were matched by recorded doubling time. Each bar represents the average signature refitting results for 3 technical replicates, **(b)** scaled to 1 to show the relative signature contribution, or **(c)** unscaled to show the absolute signature contribution in terms of number of mutations for individual replicates. **(d)** Schematic representation of mutational signature analysis from PCAWG dataset. **(e)** Cancers from TCGA/ICGC were grouped, based on whether the indicated E3 ligase genes were wild-type (wt) or mutated (mut). Mutational signatures were normalized to the total number of mutations in each sample. The level of SBS13 APOBEC signature was compared between the two groups. "E3s$_{comb}$" compares all samples, in which *UBR4*, *UBR5*, and *HUWE1* are either all wild-type, or at least one of the E3 ligase genes was mutated. Data represent Wilcox rank sum test between wt and mut of each genotype, ns: $p > 0.05$, *: $p \leq 0.05$, **: $p \leq 0.01$, ***: $p \leq 0.001$, ****: $p \leq 0.0001$, $n = 2703$ cancer genome samples). **(f)** Model of A3 protein abundance regulation. RNA binding shields A3 proteins from UBR5/HUWE1 binding and degradation, ensuring high antiviral A3 protein levels in the cytosol. Lack of RNA binding enables UBR5/HUWE1 binding to the unengaged interaction interface (red), resulting in A3 degradation. Since unengaged A3s localize to the nucleus, this ensures low nuclear A3 levels, thereby protecting from genomic DNA mutagenesis. UBR4 acts as an E4 ligase to extend poly-ubiquitin chains.

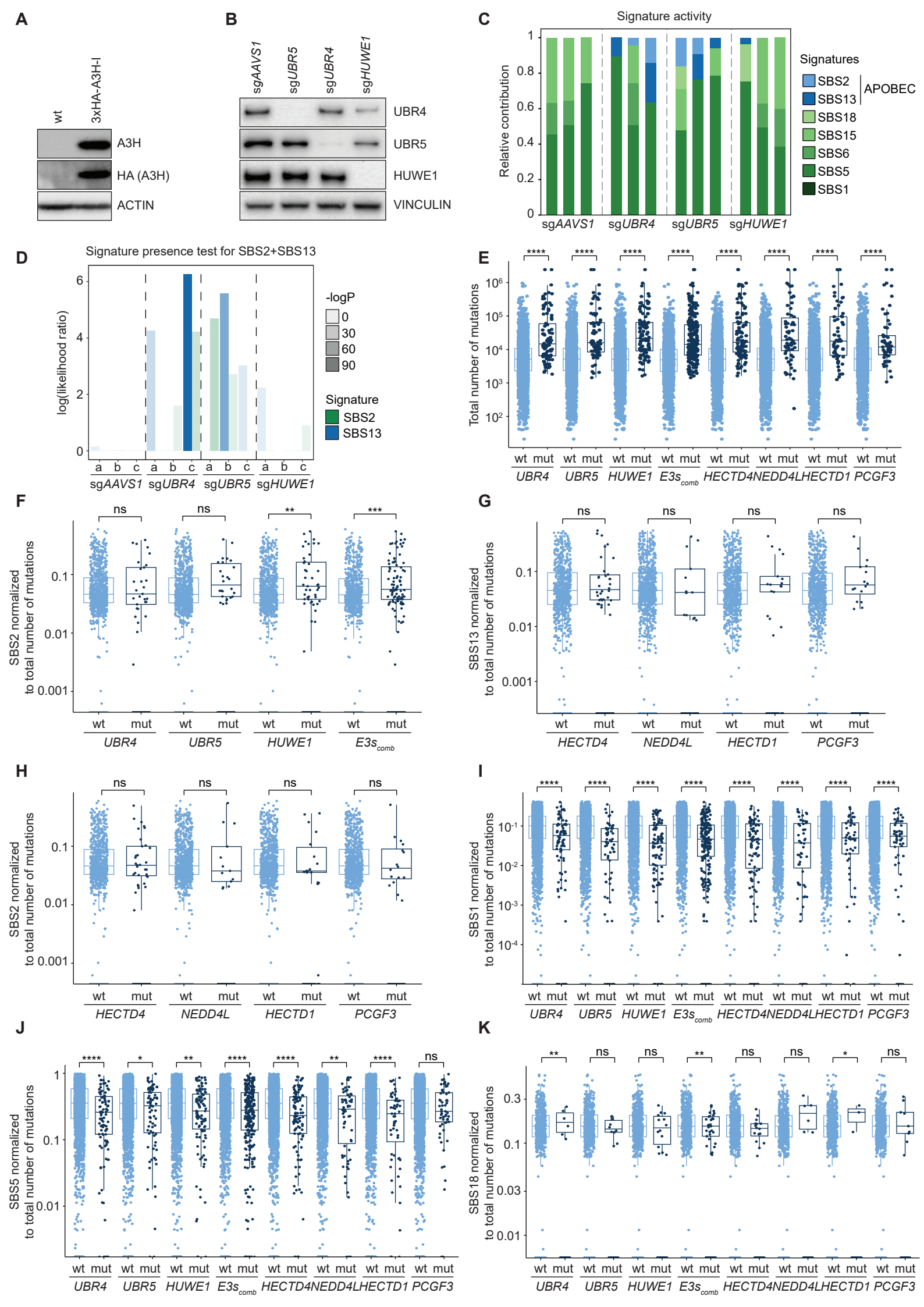
A
wt
3xHA-A3H-I
A3H
HA (A3H)
ACTIN
B
sgAAVS1
sgUBR5
sgUBR4
sgHUWE1
UBR4
UBR5
HUWE1
VINCULIN
C
Signature activity
Relative contribution
Signatures
SBS2
SBS13
APOBEC
SBS18
SBS15
SBS6
SBS5
SBS1
sgAAVS1
sgUBR4
sgUBR5
sgHUWE1
D
Signature presence test for SBS2+SBS13
log(likelihood ratio)
-logP
0
30
60
90
Signature
SBS2
SBS13
sgAAVS1
sgUBR4
sgUBR5
sgHUWE1
E
Total number of mutations
wt mut
UBR4
UBR5
HUWE1
E3s comb
HECTD4
NEDD4L
HECTD1
PCGF3
F
SBS2 normalized to total number of mutations
ns
**
***
UBR4
UBR5
HUWE1
E3s comb
G
SBS13 normalized to total number of mutations
HECTD4
NEDD4L
HECTD1
PCGF3
H
SBS2 normalized to total number of mutations
I
SBS1 normalized to total number of mutations
J
SBS5 normalized to total number of mutations
K
SBS18 normalized to total number of mutations

Figure S6. E3 ligase loss or mutation increases APOBEC signature mutations. (a) Cell lysates from a *UNG2*$^{-/-}$ RKO cell line expressing DOX-inducible Cas9 and mCherry-P2A-3xHA-A3H-I were analyzed by WB for transgene expression. **(b)** These cells we transduced with sgRNAs targeting *UBR4*, *UBR5*, or *HUWE1*, and subsequently sorted for sgRNA-positive cells. Gene editing was induced with DOX for up to four cell doublings, after which the protein levels of the targeted E3 ligases were analyzed by WB. **(c)** Best subset signature refitting of mutREAD data, averaged per genotype, using signatures related to overactivity of APOBEC family enzymes and signatures commonly active in colon carcinoma, the parent tumor type for the model cell line RKO. For the purpose of comparing signature activity across genotypes, samples were matched by doubling time. Each bar represents the signature refitting results, scaled to 1 to show the relative signature contribution. **(d)** Signature presence test for the indicated signatures. Genotypes (n = 3, a-c), are divided by vertical dashed lines. The y-axis shows the log of the likelihood ratio, representing the maximum likelihood of the data, given a refit model including the signature of interest over the maximum likelihood of the data, given a refit model excluding the signature of interest. A log(likelihood ratio) greater than 0 indicates a significant activity of the signature of interest. The translucence of the bars (-log(p)) indicates the level of significance of the likelihood ratio test compared to the null hypothesis, which assumes that the mutational profile can be reasonably reconstructed without the signature of interest. **(e-k)** Cancers from TCGA/ICGC were grouped, based on whether the indicated E3 ligase genes were wild-type (wt) or mutated (mut), and the **(e)** total number of mutations per group plotted. **(f-k)** Subsequently, mutational signatures were normalized to the total number of mutations in each sample, and the levels of indicated signatures compared between two groups. "E3s_{comb}" compares all samples, in which *UBR4*, *UBR5* and *HUWE1* are either all wild-type (wt), or at least one of the E3 ligase genes was mutated (mut). Data represent Wilcox rank sum test between wt and mut of each genotype, ns: $p > 0.05$, *: $p \leq 0.05$, **: $p \leq 0.01$, ***: $p \leq 0.001$, ****: $p \leq 0.0001$, n = 2703 cancer genome samples).

Materials and methods

Vectors

The lentiviral human ubiquitin-focused sgRNA library consists of 6 sgRNAs per gene for ubiquitin-proteasome system- and autophagy-related genes, and has been described[117]. Lentiviral vectors expressing single or dual sgRNAs from a U6 promoter and eBFP2 or iRFP from a PGK promoter have been described[44]. sgRNA CDSs were cloned in pLentiv2-U6-PGK-iRFP670-P2A-Neo[44] to perform knock-outs in RKO cell lines. The Dual-A3H-reporter (pLX303-SFFV-MYC-mCherry-A3H-II-P2A-OLLAS-EGFP-A3H-I) was constructed by cloning the ORF of human A3H-I or A3H-II into a modified pLX303 vector[46,118]. cDNAs encoding A3H-I, A3H-II, A3H-I-G105R, A3H-II-R105-G, A3H-II-W115A, A3H-II-R175/176E, A3H-II-E56A-W115A-R175/176E, A3H-I-K-mutants, A3A, A3C, A3D, A3F, A3G, A3G-RNA-binding mutants were synthesized by Twist Bioscience, or generated by fusion PCR and cloned into a modified pLX303 vector for mammalian expression, or into a modified pET47 containing a decahistidine (10×His) tag followed by a Maltose binding protein (MBP) tag and a 3C site vector for bacterial expression. The plasmids and sgRNAs used in this study are listed in the Key resource table.

Cell culture

Unless otherwise indicated, experiments in this study were reproduced at least twice in independent experiments. All cell lines used in this study were maintained at 37 ºC with 5% CO2 in a humidified incubator, routinely tested for mycoplasma contamination, and authenticated by STR analysis. Human RKO (sex unspecified; American Type Culture Collection (ATCC) cat. no. CRL-2577, RRID:CVCL_0504) and THP-1 cells (male; ATCC cat no. TIB-202, RRID:CVCL_0006) were cultured in RPMI 1640 (Gibco) supplemented with 10% FBS (Sigma-Aldrich), L-glutamine (4 mM, Gibco), sodium pyruvate (1 mM, Sigma-Aldrich) and penicillin/streptomycin (100 U/ml/100 µg/ml, Sigma-Aldrich). HeLa cells (female; ATCC cat. no. CCL-2, RRID:CVCL_0030), Lenti-293T lentiviral packaging cells (female, Clontech, cat. No. 632180), and HEK-293T cells (female; ATCC cat. No. CRL-3216, RRID: RRID:CVCL_0063) were cultured in Dulbecco's modified Eagle's medium (DMEM; Sigma-Aldrich) supplemented with 10% FBS and penicillin/streptomycin (Sigma-Aldrich). All cell lines used in this study are listed in the Key resource table.

Generation of clonal iCas9 cell lines

THP-1-DOX-Cas9-P2A-GFP cells were generated by transducing THP-1 cells with the pRRL-TRE3G-Cas9-P2A-GFP-PGK-IRES-rtTA3 lentiviral vector[46]. Cas9 expression was induced with 500 ng/ml of Doxycycline hyclate (DOX, Sigma-Aldrich) and single cells were sorted by FACS into 96-well plates using a FACSAria III cell sorter (BD Biosciences) to obtain single-cell-derived clones. To generate the genetic screening cell line (Dual-A3H-reporter), RKO-DOX-Cas9-P2A-BFP cells[117] were transduced with pLX303-SFFV-MYC-mCherry-A3H-II-P2A-OLLAS-EGFP-A3H-I and mCherry$^+$/GFP$^+$ double-positive cells were sorted by FACS into 96-well plates using a FACSAria III cell sorter (BD Biosciences). The mutREAD cell line was generated by co-transducing pLX303-SFFV-MYC-mCherry-P2A-3xHA-A3H-I and DualCRISPR-hU6-sg*UNG2*-mU6-sg*UNG2*-Thy1.1-P2A-Neo into RKO-DOX-Cas9-P2A-GFP[44]. Following Cas9 induction with 200 ng/ml DOX for 6 days, live cells were immunostained for the Thy1.1 surface marker. In brief, cells were washed with PBS, and incubated for 15 min.at 4 °C in Human BD Fc Block (BD Biosciences) to inhibit non-specific antibody binding. Cells were then stained with APC anti-rat CD90/mouse CD90.1 (Thy-1.1) Antibody (BioLegend, 1:260) for 20 min. at 4 °C. Following two washes, mCherry$^+$/Thy1.1$^+$ single cells were sorted into 96-well plates. *UNG2* homozygous knock-out was confirmed by PCR amplification, TA-cloning and Sanger sequencing of the targeted *UNG2* locus. Polyclonal RKO cell lines were obtained by transducing the parental RKO-DOX-Cas9-P2A-BFP or RKO-DOX-Cas9-P2A-GFP cells with the respective lentiviral expression plasmids listed in the Key resource table.

966 **Transfections**
967 Transfections for analysis by WB were performed by mixing DNA and polyethylenimine (PEI,
968 Polysciences) in a 1:3 ratio (w/w) in DMEM (Sigma-Aldrich) without supplements. Transfection
969 was performed using 1000 ng of total DNA per well. The day before transfection, 2×10^5 HEK-
970 293T cells were seeded in 6-well clusters in fully supplemented DMEM media. 36 h. after
971 transfection cells were harvested, washed with ice cold PBS and stored at −80 ºC until further
972 processing.
973
974 **Lentivirus production and transduction**
975 Lenti-293T lentiviral packaging cells were transfected with DNA mixes containing lentiviral
976 transfer plasmids, pCRV1-Gag-Pol[119] and pHCMV-VSV-G[120] using polyethylenimine (PEI,
977 Polysciences) in a 1:3 µg DNA/ µl PEI ratio in non-supplemented DMEM. Virus-containing
978 supernatants were clarified of cellular debris by filtration through a 0.45 µm filter. Virus-like
979 particles were directly used after harvesting or stored at -80 °C. Target cells were transduced
980 in the presence of 5 µg/ml polybrene (Sigma-Aldrich).
981
982 **FACS-based CRISPR–Cas9 screens**
983 Lentivirus-like particles were used to transduce RKO-DOX-Cas9-mCherry-A3H-II-P2A-EGFP-
984 A3H-I cells (Dual-A3H-reporter) at a multiplicity of infection (MOI) of less than 0.2 TU/cell, and
985 500 to 1,000-fold library representation. The percentage of library-positive cells was
986 determined after 3 days of transduction by immunostaining for the Thy1.1 surface marker and
987 subsequent flow cytometric analysis. RKO cells with integrated lentiviral vectors were selected
988 with G418 (1 mg/ml, Sigma-Aldrich) for 5 days. After G418 selection, Cas9 genome editing
989 was induced with DOX (350 ng/ml, Sigma-Aldrich) and after 3 days and 6 days, cells were
990 sorted by FACS. Therefore, cells were harvested, washed with PBS, resuspended in
991 supplemented RPMI-1640 and sorted using the FACSAria III cell sorter operated by BD
992 FACSDiva software (v8.0). RKO cells were gated for non-debris, singlets, BFP-positive (Cas9
993 expression), EGFP-positive, mCherry-positive, and 1-2% of cells with the lowest or highest
994 EGFP or mCherry signals were sorted into PBS. At least 1×10^6 cells were collected for each
995 population at each time point in three independent experiments. Sorted samples were re-
996 analyzed for purity, pelleted and stored at −80 ºC until further processing. Additionally, 10
997 million cells from an unsorted reference sample corresponding to 1,000-fold library
998 representation were collected on each sorting day and stored at −80 ºC until further processing.
999
1000 **Next-generation sequencing library preparation**
1001 NGS libraries of sorted and unsorted control samples were processed as previously
1002 described[44]. In brief, isolated genomic DNA was subjected to two-step PCR. The first PCR
1003 amplified the integrated sgRNA cassettes, whereas the second PCR introduced the Illumina
1004 adapters. Purified PCR products' size distribution and concentrations were measured using a
1005 fragment analyzer (Advanced Analytical Technologies). Equimolar ratios of the obtained
1006 libraries were pooled and sequenced on a HiSeq 2500 platform (Illumina). Primers used for
1007 library amplification are listed in the Key resource table.
1008
1009 **Analysis of pooled CRISPR screens**
1010 The analysis of the genetic screens was carried out as previously described[44]. Three biological
1011 replicates of each sort were included in the analysis. In brief, sgRNAs enriched on day 3 and
1012 day 6 (post-Cas9 induction) sorted samples were compared to the matching unsorted control
1013 populations harvested on the same days using MAGeCK[121]. Hits were selected based on $\log_2$
1014 fold-change and p-value and grouped by functional categories. To exclude unspecific hits, we
1015 selected genes enriched in EGFP-A3H-I^{high} cell populations on day 3 with a $\log_2$ fold-change
1016 >0.45 and adj. p-value <0.05, which were neither enriched in mCherry^{high} on day 3 ($\log_2$ fold-
1017 change >0.45, p-value <0.05) nor in GFP^{low} on day 3 ($\log_2$ fold-change >0.45, p-value <0.05).
1018 Similarly, genes enriched in EGFP-A3H-I^{high} cell populations on day 6 with a $\log_2$ fold-change
1019 >0.6 and adj. p-value <0.05, which were neither enriched in mCherry^{high} on day 3 ($\log_2$ fold-
1020 change >0.45, p-value <0.05) or day 6 ($\log_2$ fold-change >0.6, p-value <0.05) nor in GFP^{low} on
1021 day 6 ($\log_2$ fold-change >0.6, p-value <0.05) were selected.

1022 **Protein half-life determination**
1023 To estimate A3H-I or A3H-II protein half-lives, cells were treated with 200 µg/ml of
1024 cycloheximide (CHX, Sigma-Aldrich). At the indicated time points, total protein extracts were
1025 generated using 2x Disruption buffer (1.05 M Urea, 0.667 M β-Mercaptoethanol and 0.7%
1026 SDS) or RIPA buffer supplemented with 1% SDS and Benzonase (50 mM Tris HCl (pH 7.4),
1027 150 mM NaCl, 1% NP-40, 0.5% Sodium Deoxycholate, 1 mM EDTA, 1% SDS, 1 mM PMSF
1028 (Sigma-Aldrich), Benzonase (25 U/ml, Merck) and 1X cOmplete Protease Inhibitor Cocktail
1029 (Roche), analyzed by WB, quantified and normalized as indicated. Single exponential decay
1030 curves were plotted using GraphPad Prism (v9), from which protein half-lives were calculated.
1031
1032 **Immunofluorescence confocal microscopy**
1033 250,000 RKO cells stably expressing OLLAS-A3H-I or OLLAS-A3H-II (RKO-MYC-mCherry-
1034 P2A-OLLAS-A3H-I/II) or RKO cells stably expressing EGFP-A3H-I/II/I-G105R/-II-R105G/II-
1035 W115A/II-R175/176E were seeded onto coverslips. After 48 hours, cells were fixed with 4%
1036 paraformaldehyde (PFA) for 15 min. In case of antibody staining, cells were permeabilized with
1037 0.25% Triton X-100 in PBS for 5 min., followed by blocking of non-specific sites by incubation
1038 with 1% BSA for 30 min. at RT. Coverslips were incubated for 1 h. at RT with primary anti-A3H
1039 antibody (Novus Biologicals) 1:100 in 1% BSA, followed by incubation with 1:800 anti-rabbit
1040 IgG Alexa Fluor 488 (Abcam) secondary antibody, and incubation for 5 min. with 0.4X Hoechst
1041 (Thermo Fisher Scientific) in PBS. The coverslips were mounted using ProLong Gold Antifade
1042 Mountant (Invitrogen). Images were collected using a Zeiss LSM 980 confocal microscope at
1043 40X magnification.
1044
1045 **Subcellular fractionation**
1046 Subcellular fractionation was performed as previously described[122]. In brief, two million cells
1047 were washed in 1 ml PBS and lysed in 500 µl ice-cold REAP buffer (0.1% NP-40 in 1x PBS)
1048 supplemented with 1 mM PMSF (Sigma-Aldrich), 1X cOmplete Protease Inhibitor Cocktail
1049 (Roche) and Benzonase. 240 µl of the lysates were collected as whole cell fractions, the
1050 remaining lysate was centrifuged at 3,000 x g for 60 sec. at 4°C. 240 µl of supernatants were
1051 collected as cytosolic fractions, after which pellets were washed with 500 µl of REAP buffer,
1052 collected by centrifugation at 3,000 x g for 60 sec. at 4°C, and then resuspended in 240 µl of
1053 REAP buffer (nuclear fraction). All fractions were subsequently supplemented with 6x Laemmli
1054 sample buffer (62.5 mM Tris-HCl (pH 6.8), 5.8% Glycerol, 2% SDS and 1.7% β-
1055 Mercaptoethanol), and boiled for 10 min. Equal volumes of fractions were loaded on a 12 %
1056 SDS polyacrylamide gel.
1057
1058 **Western blot analysis**
1059 24-48 hours post seeding, cells were treated with various inhibitors (CHX (200 µg/ml), MG132
1060 (10 µM), EPOX (10 µM), CQ (50 µM), BafA (400 nM), NH4Cl (20mM), Leu (50 µM)) for the
1061 indicated time points or left untreated. Cells were lysed in Disruption buffer or RIPA lysis buffer
1062 supplemented with 1% SDS and Benzonase. Lysates were rotated for 30 min. at 4 °C and then
1063 centrifuged at 18,500 x g for 10 min. at 4 °C. Supernatants were transferred to new tubes and
1064 protein concentrations were determined using the BCA Protein Assay Kit (Thermo Fisher
1065 Scientific). Between 20-50 µg of protein per sample was mixed with Laemmli sample buffer
1066 and boiled for 10 min. Proteins were loaded on 12% or 15% SDS polyacrylamide gels, based
1067 on the molecular weight of the protein of interest, or alternatively 3-8% NuPage gels
1068 (Invitrogen) to probe for high molecular weight proteins. Proteins were separated by SDS page
1069 using Tris-Glycine (25 mM Tris, 192 mM glycine, 0.1% SDS) or Tris-Acetate (2.5 mM Tricine,
1070 2.5 mM Tris, 0.05% SDS) SDS running buffer, respectively. Proteins were blotted on PVDF or
1071 nitrocellulose membranes at 4 °C for 75 min. at 300 mA in Towbin buffer (25 mM Tris pH 8.3,
1072 192 mM glycine and 20% ethanol). Membranes were blocked in 5% BSA in PBS-T for 1 h. at
1073 RT, and subsequently incubated with primary antibodies diluted in 5% BSA overnight at 4 °C
1074 (ARP10 Antibody (Novus, 1:1000), Anti-APOBEC3B Antibody (Abcam, 1:1000), Anti-MYC
1075 antibody (Sigma-Aldrich, 1:5000), HA-Tag (C29F4) Rabbit mAb (Cell Signaling Technology,

1:1000), HA-Tag (6E2) Mouse mAb (Cell Signaling Technology, 1:1000), OLLAS Epitope Tag Antibody (L2) (Novus, 1:4000), LC3B Antibody ((Cell Signaling Technology, 1:1000), Ubiquitin (P4D1) (Santa Cruz Biotechnology, 1:1000), Anti-UBR4/p600 antibody (Abcam, 1:1000), Rabbit anti-EDD1 Antibody (Bethyl, 1:1000), Rabbit anti-Lasu1/Ureb1 Antibody (HUWE1) (Bethyl, 1:1000), Monoclonal Anti-α-Tubulin antibody produced in mouse (Sigma-Aldrich, 1:1000), Lamin A/C Antibody (E-1) (Santa Cruz Biotechnology, 1:1000), Monoclonal Anti-Vinculin antibody (Sigma-Aldrich, 1:1000), Anti-beta Actin antibody (HRP) (Abcam, 1:20000)). The next day, the membranes were washed three times for 5 min. each with PBS-T and incubated with HRP-coupled secondary antibodies in 5% skimmed milk for 1 h. at RT (Anti-rabbit IgG, HRP-linked Antibody (Cell Signaling Technology, 1:3500), Anti-mouse IgG, HRP-linked Antibody (Cell Signaling Technology, 1:3500), Goat-anti-mouse IgG Light Chain HRP (1:5000), Goat Anti-Rat IgG H&L (HRP) (Abcam, 1:50000)) and imaged with the ChemiDoc Imaging System (Bio-Rad). Relative protein levels were quantified using Image Lab (Bio-Rad).

Co-Immunoprecipitation assays

HEK-293T cells from one confluent 35-mm dish were lysed in 100 µl of Frackelton lysis buffer (10 mM Tris (pH 7.4), 50 mM NaCl, 30 mM $Na_4P_2O_7$, 50 mM NaF, 2 mM EDTA, 1% Triton X-100, 1 mM DTT, 1 mM PMSF (Sigma-Aldrich), and 1X cOmplete Protease Inhibitor Cocktail (Roche)). Cells were incubated on a rotating wheel at 4 °C for 30 min. and subsequently centrifuged at 20,000 x g at 4 °C for 30 min. The supernatant was transferred to a new tube and 10 µl (10% of the lysate used for the IPs) was collected as input. 500 µg of lysates were incubated overnight at 4 °C on a rotating wheel with anti-HA antibody (Cell Signaling Technology, 1:100). The next day, magnetic beads (Protein A/G Magnetic Beads, Thermo Fisher Scientific) used for anti-HA antibody IPs, were blocked by rotation in 3% BSA in Frackelton Buffer for 1 h. at 4 °C. 25 µl of beads were added to 500 µg of lysates and rotated for 2 h. at 4 °C. Then, the beads were washed five times with 1 ml of Frackelton lysis buffer. Proteins were eluted by boiling in 2X Disruption buffer for 10 min. at 95 °C.

Immunoprecipitations for ubiquitination

HEK-293T cells from confluent 35-mm dishes were lysed in 100 µl of RIPA buffer with 1% SDS (50 mM Tris-HCl (pH 7.4), 150 mM NaCl, 1% SDS, 0.5% sodium deoxycholate, 1% Triton X-100), supplemented with 40 mM N-Ethylmaleimide, 40 mM iodoacetamide, 25 U/ml Benzonase, 1 mM PMSF (Sigma-Aldrich), and 1X cOmplete Protease Inhibitor Cocktail (Roche). Cells were incubated on a rotating wheel at 4 °C for 30 min. and centrifuged at 20,000 x g at 4 °C for 15 min. Supernatants were transferred to new tubes and 30 µg of the lysates were collected as input. 500 µg of lysates were incubated overnight at 4 °C on a rotating wheel with an anti-HA antibody (Cell Signaling Technology, 1:100). The next day, magnetic beads (Protein A/G Magnetic Beads, Thermo Fisher Scientific) were blocked by rotation in 3% BSA in RIPA Buffer for 1 h. at 4 °C. 25 µl of beads were added to 500 µg of lysates and rotated for 2 h. at 4 °C. Subsequently, beads were washed five times with 1 ml of RIPA buffer, supplemented with 300 mM NaCl. Proteins were eluted by boiling in 2X Disruption buffer for 10 min. at 95 °C.

RNA isolation, cDNA synthesis, and qPCR

For mRNA half-life determination, cells were treated with actinomycin D (ActD) at a final concentration of 5 µg/ml for the indicated times, at which point total RNA was isolated. The decay of *APOBEC3H* mRNA was assessed by RT-qPCR. RNA from 1×10^6 cells was isolated using Trizol reagent (Thermo Fisher Scientific) and treated with Turbo DNase (Thermo Fisher Scientific). cDNA was prepared using random hexamer primers and RevertAid Reverse Transcriptase (Thermo Fisher Scientific). Real-time PCR experiments were run on a Mastercycler (Biorad), using the Luna Universal qPCR Master Mix (NEB). Primers for qPCR are listed in the Key resource table.

1129 **TurboID**
1130 A3H-I and A3H-II, as well as an EGFP control were cloned into lentiviral plasmid pCW-MYC-
1131 TurboID-MCS-PGK-mCherry-P2A-rtTA[46], for the expression of fusion proteins N-terminally
1132 tagged with TurboID. For the TurboID experiment, polyclonal cell lines stably expressing DOX-
1133 inducible TurboID-A3H-I, TurboID-A3H-II and TurboID-EGFP were stimulated with DOX for
1134 48 h. to induce the expression of the TurboID fusion constructs. Subsequently, cells were
1135 stimulated for 5 h. with 10 µM EPOX to inhibit proteasomal degradation, and finally biotinylation
1136 was induced for 15 min. by addition of 500 µM Biotin (Sigma) to the cell culture medium.
1137 Subsequently, cells were washed 4 times with ice-cold PBS, prior to lysis in RIPA lysis buffer
1138 (50 mM Tris HCl (pH 7.4), 150 mM NaCl, 1% NP-40, 0.5% Sodium Deoxycholate, 1 mM EDTA,
1139 0.1% SDS, 1 mM PMSF (Sigma-Aldrich) and 1X cOmplete Protease Inhibitor Cocktail (Roche).
1140 Lysates were rotated for 30 min. at 4 °C, centrifuged at 18,500 x g for 10 min. at 4 °C, and
1141 protein concentrations were determined by BCA assay. 1200 µg of protein was incubated
1142 overnight rotating at 4°C with 200 ul of Streptavidin beads (Thermo Scientific) which were
1143 acetylated with Sulfo-NHS-Acetate beforehand, as described[123]. Beads were washed twice
1144 with 1 ml of RIPA buffer, once with 1 ml of 2 M Urea in 10 mM Tris (pH 8), twice with 1 ml RIPA
1145 buffer and five times with 50 mM HEPES (pH 7.8). Three technical replicates were subjected
1146 to nLC-MS/MS analysis.

1147 **Sample preparation for mass spectrometry analysis**
1148 Beads were resuspended in 50 µl 1 M Urea and 50 mM ammonium bicarbonate. Disulfide
1149 bonds were reduced with 2 µl of 250 mM dithiothreitol (DTT) for 30 min. at room temperature
1150 before adding 2 µl of 500 mM iodoacetamide and incubating for 30 min. at room temperature
1151 in the dark. Remaining iodoacetamide was quenched with 1 µl of 250 mM DTT for 10 min.
1152 Proteins were digested with 150 ng LysC (mass spectrometry grade, FUJIFILM Wako
1153 chemicals) at 25 °C overnight. The supernatant was transferred to a new tube and digested
1154 with 150 ng trypsin (Trypsin Gold, Promega) in 1.5 µl 50 mM ammonium bicarbonate at 37 °C
1155 for 5 h. The digest was stopped by the addition of trifluoroacetic acid (TFA) to a final
1156 concentration of 0.5 %, and the peptides were desalted using C18 Stagetips[124].
1157
1158 **Liquid chromatography-Mass spectrometry data acquisition**
1159 Peptides were separated on an Ultimate 3000 RSLC nano-flow chromatography system
1160 (Thermo-Fisher), using a pre-column for sample loading (Acclaim PepMap C18, 2 cm × 0.1
1161 mm, 5 µm, Thermo-Fisher), and a C18 analytical column (Acclaim PepMap C18, 50 cm × 0.75
1162 mm, 2 µm, Thermo-Fisher), applying a segmented linear gradient from 2% to 35% and finally
1163 80% solvent B (80 % acetonitrile, 0.1 % formic acid; solvent A 0.1 % formic acid) at a flow rate
1164 of 230 nl/min. over 120 min. Eluting peptides were analyzed on an Exploris 480 Orbitrap mass
1165 spectrometer (Thermo Fisher) coupled to the column with a FAIMS pro ion-source (Thermo-
1166 Fisher) using coated emitter tips (PepSep, MSWil) with the following settings: The mass
1167 spectrometer was operated in DDA mode with two FAIMS compensation voltages (CV) set to
1168 -45 or -60 and 1.5 s. cycle time per CV. The survey scans were obtained in a mass range of
1169 350-1500 m/z, at a resolution of 60k at 200 m/z, and a normalized AGC target at 100%. The
1170 most intense ions were selected with an isolation width of 1 m/z, fragmented in the HCD cell
1171 at 28% collision energy, and the spectra recorded for max. 50 ms. at a normalized AGC target
1172 of 100% and a resolution of 15k. Peptides with a charge of +2 to +6 were included for
1173 fragmentation, the peptide match feature was set to preferred, the exclude isotope feature was
1174 enabled, and selected precursors were dynamically excluded from repeated sampling for 45 s.
1175
1176 **Data analysis**
1177 MS raw data split for each CV using FreeStyle 1.7 (Thermo Fisher), were analyzed using the
1178 MaxQuant software package (version 1.6.17.0)[125] with the Uniprot human reference proteome
1179 (version 2020_01)[126], as well as a database of most common contaminants. The search was

1180 performed with full trypsin specificity and a maximum of two missed cleavages at a protein and
1181 peptide spectrum match false discovery rate of 1%. Carbamidomethylation of cysteine
1182 residues was set as fixed, oxidation of methionine, phosphorylation (STY) and N-terminal
1183 acetylation as variable modifications. For label-free quantification the "match between runs"
1184 only within the sample batch and the LFQ function were activated - all other parameters were
1185 left at default. MaxQuant output tables were further processed in R 4.2.1[127] using
1186 Cassiopeia_LFQ[128]. Reverse database identifications, contaminant proteins, protein groups
1187 identified only by a modified peptide, protein groups with less than two quantitative values in
1188 one experimental group, and protein groups with less than 2 razor peptides were removed for
1189 further analysis. Missing values were replaced by randomly drawing data points from a normal
1190 distribution model on the whole dataset (data mean shifted by -1.8 standard deviations, a width
1191 of the distribution of 0.3 standard deviations). Differential expression analysis was performed
1192 with Enrichr[129–131]. In detail, differentially enriched proteins in A3H-I/GFP (light blue, LFC >1,
1193 p-value <0.01) and A3H-II/GFP (dark blue, LFC >1, p-value <0.01) were compared using
1194 RStudio (v4.1.3). GO:CC and GO: BP terms were derived for proteins being specifically
1195 enriched in the A3H-I or A3H-II interactome, or for shared interactors.
1196
1197 **Proteomics data deposition**
1198 The mass spectrometry proteomics data have been deposited to the ProteomeXchange
1199 Consortium via the PRIDE partner repository[132] with the dataset identifier PXD051267.
1200
1201 **Protein purification**
1202 BL21 (DE3) RIPL *E. coli* cells harboring 10xHis-MBP-A3H expression vectors were grown at
1203 37 °C. IPTG at 0.3 mM was added when OD600 reached about 0.6–0.8 for overnight induction
1204 at 18°C. To purify dimer and monomer of 10xHis-MBP-fused A3H, *E. coli* cells expressing
1205 MBP-A3H-I/II/II-E56A-W115A-R175/176E were harvested and lysed using an EmulsiFlex C3
1206 homogenizer in buffer A (25 mM HEPES pH 7.5, 500 mM NaCl, 20mM imidazole, 5% glycerol,
1207 5mM β-Mercaptoethanol, 1X EDTA-free cOmplete Protease Inhibitor Cocktail (Roche), 0.5 mM
1208 PMSF (Sigma-Aldrich), 100 ug/ml RNase A (Carl Roth)). The clear soluble fraction obtained
1209 after centrifugation (45 min. at 18.000 x g) was loaded onto a HisTrap HP 5 mL, washed with
1210 wash buffer (25 mM HEPES pH 7.5, 500 mM NaCl, 20mM imidazole, 5% glycerol, 5mM β-
1211 Mercaptoethanol) and eluted with buffer B (25 mM HEPES pH 7.5, 500 mM NaCl, 500mM
1212 imidazole, 5% glycerol, 5mM β-Mercaptoethanol). Fractions containing A3H were identified by
1213 SDS page, concentrated, and separated by Superdex 200 10/300 gel filtration chromatography
1214 (Cytiva) in SEC buffer (25 mM HEPES pH 7.5, 250 mM NaCl, 5% glycerol, 2 mM DTT. The
1215 dimer and monomer fractions were collected, concentrated and flash frozen in liquid nitrogen.
1216 Codon-optimized human HUWE1 was synthesized in fragments and assembled into a
1217 GoldenBac pGBdest vector using a BsaI-GoldenGate reaction[133]. The construct had a his_8 tag
1218 followed by a rigid enhancer linker
1219 (AEAAAKEAAAKEAAAKEAAAKALEAEAAAKEAAAKEAAAKEAAAKA) and then a TEV
1220 cleavage site. Human UBR4 was cloned by the same procedure, except the tag used was a
1221 C-terminal Strep tag separated from the protein by a 3C cleavage site. Plasmids were
1222 transformed into DH10 MultiBac cells for bacmid generation. *Spodoptera frugiperda* (Sf9) cells
1223 in ESF921 serum-free growth medium (Expression Systems) were transfected with the
1224 bacmids for virus amplification, which was monitored using yellow fluorescent protein signal.
1225 HUWE1 and UBR4 were then expressed in *Trichoplusia ni* High-Five insect cells (Thermo
1226 Fisher) with a density of 1.5 $x10^6$ using a 1:70 inoculation from the V1 stock for 92 hours at
1227 21°C in Insect Xpress Protein-free Insect Cell Medium (Lonza) supplemented with GlutaMAX
1228 (GIBCO) and Pen/Strep Amphotericin B (Lonza). Cells were harvested by centrifugation at 700
1229 x g, washed in PBS and then flash frozen and stored at -70°C. For HUWE1, the thawed pellet

1230 was resuspended in 50 mM HEPES pH 7.5, 300 mM NaCl, 0.5 mM TCEP, 20 mM imidazole
1231 with Complete EDTA-free Protease inhibitor (Roche) and 20 µl Benzonase (IMP Molecular
1232 Biology Service) and lysed using dounce homogenization. The lysate was cleared by
1233 centrifugation at 40,000 x g. The soluble fraction was then loaded on a 5 ml HisTrap HP column
1234 (Cytiva) pre-equilibrated in the lysis buffer using an Äkta Pure 25 system (Cytiva). The column
1235 was washed with 10 column volumes of the same buffer, followed by 7 column volumes of the
1236 same buffer but with 35 mM imidazole, and then eluted with 300 mM imidazole. The protein
1237 was cleaved with TEV protease and simultaneously dialyzed to remove imidazole overnight.
1238 The cleaved protein was then reapplied to the HisTrap HP column in 20 mM imidazole and the
1239 flow through was collected and concentrated to 1.5 ml. Finally, the protein was applied to a
1240 Superose 6 16/60 column (Cytiva) equilibrated in 50 mM HEPES pH 7.5, 150 mM NaCl, 0.5
1241 mM TCEP. Protein-containing fractions were pooled and concentrated. The protein was pure
1242 as assessed by SDS-PAGE and the concentration was estimated by A280 absorption using
1243 an extinction coefficient of 251,770 M^{-1} cm^{-1}. For UBR4, the same lysis procedure was used
1244 except with phosphate buffered saline (PBS), 0.5 mM TCEP at pH 7.4 as the buffer. The
1245 soluble lysate was then loaded on a 5 ml StrepTrap HP column (Cytiva) equilibrated in PBS,
1246 washed with the same buffer and then eluted with 2.5 mM desthiobiotin. Eluted UBR4 was
1247 further applied to a Resource Q column (Cytiva) equilibrated in PBS for further purification by
1248 anion exchange chromatography using a 250 to 500 mM NaCl gradient. UBR4-containing
1249 fractions were pooled and concentrated and the final concentration measured by absorption
1250 at 280 nm using a calculated extinction coefficient of 472,140 $M^{-1}cm^{-1}$ The codon-optimized
1251 UBE2A gene was synthesized by Twist Bioscience. The NEB HiFi assembly kit (New England
1252 Biolabs) was used to clone the gene into a pET29b expression vector, which contained an N-
1253 terminal His6-tag and TEV cleavage site. Expression was performed using *E. coli* BL21 (DE3)
1254 cells with IPTG induction at 20 °C overnight. Cells were resuspended in buffer containing
1255 50 mM Tris pH 7.5, 150 mM NaCl, 10 mM imidazole, Complete EDTA-free protease inhibitor
1256 cocktail. Cells were lysed by sonication and clarified by centrifugation at 18,500*g* for 20 min at
1257 4 °C. Clarified lysates were then incubated with Ni-NTA resin (Qiagen) for 1 h at 4 °C with mild
1258 agitation. Ni-NTA resin was washed before elution with 150 mM imidazole. UBE2A was further
1259 purified by SEC using a Superdex 75 16/600 column (Cytiva) equilibrated in 50 mM Tris,
1260 150 mM NaCl and 0.5 mM TCEP, pH 7.5. Recombinant human UBR5, Ubiquitin, DyLight488-
1261 labeled Ubiquitin, UBE2D3 and UBA1 were purified as described previously[91,107,134].
1262
1263 **UREA denaturing gel**
1264 To determine the amount of bound RNA, equal protein amounts of 10xHis-MBP-A3H-I/II/II-
1265 E56A-W115A-R175/176E were denatured by the addition of 2x denaturing buffer (0.6 g/ml
1266 urea, 0.1% SDS, 1 mM EDTA pH 8.0, 0.5 mg/ml Xylene Cyanol, 0.5 mg/ml Bromophenol blue)
1267 and incubation for 5 min. at 95 °C. Subsequently, the RNA was separated from the proteins
1268 on a 6%Urea-TBE gel and visualized by SYBR Gold staining.
1269
1270 ***In vitro* ubiquitination assays**
1271 *In vitro* ubiquitination assays contained 10 µM ubiquitin, 1 µM DyLight488-labeled ubiquitin for
1272 in-gel visualization, 0.2 µM E1 (UBA1), 0.4 µM E2 (UBE2A for UBR4, UBE2D3 for UBR5 and
1273 HUWE1), 0.4 µM E3 (UBR4, UBR5, HUWE1) and 4 µM substrate protein (10xHis-MBP-A3H),
1274 unless indicated otherwise. The assays were performed in 25 mM HEPES pH 7.5, 200 mM
1275 NaCl, 5 mM MgCl2, 0.5 mM TCEP (assay buffer) at 30 °C (UBR5) or 37°C (UBR4 and HUWE1)
1276 for 1 h. in 11 µl volumes. Reactions were initiated by the addition of 5 mM ATP. After one hour,
1277 reactions were diluted in 500 µl immune-precipitation buffer (RIPA buffer supplemented with
1278 40 mM N-Ethylmaleimide (Sigma-Aldrich), 40 mM iodoacetamide (Sigma-Aldrich), 1 mM
1279 PMSF (Sigma-Aldrich), and 1X cOmplete Protease Inhibitor Cocktail (Roche) and incubated
1280 with 15 µl of anti-MBP couped beads (pre-blocked for 1h in RIPA with 3 % BSA; NEB) for 2 h.

at 4°C. Beads were washed 5 times with RIPA-300 mM NaCl, followed by elution of A3H in 2x Laemmli sample buffer with 2 mM DTT. SDS-PAGE was performed using 4–20% Mini-PROTEAN TGX Stain-Free (BioRad), and ubiquitinated A3H was detected by visualization of DyLight488-ubiquitin using ChemiDoc MP system (Bio-Rad).

mutREAD sequencing and detection of mutational signatures

A monoclonal RKO-DOX-Cas9-P2A-GFP cell line expressing MYC-mCherry-P2A-3xHA-A3H-I that also has a homozygous knock-out of *UNG2*$^{-/-}$ was transduced with DualCRISPR-hU6-sgRNA-mU6-sgRNA-iRFP670 targeting indicated genes and bulk sorted for iRFP^{+} cells. Cas9 was induced with DOX and sequential samples collected up to 10 days after induction. Their doubling times were calculated based on cell numbers counted during cell passaging, and samples of similar doublings compared for analysis. Cells were harvested for WB to verify E3 ligase knock-out and gDNA extraction. DNA was isolated using the DNeasy Blood & Tissue Kit (Qiagen) after which samples were subjected to mutREAD library preparation as described[58]. In brief, 500 ng gDNA was digested with 50 U PstI-HF (NEB) and 50 U ApoI-HF (NEB) together with 0.187 µM annealed mutREAD adapters (see Key resource table), 400 U T4 DNA ligase (NEB), 1 mM ATP in 1X CutSmart buffer. The 50 µl reaction was incubated for 3 h. at 30 °C in a thermal cycler and subsequently stopped by addition of 10 µL 50 mM EDTA. DNA fragments were size selected for 400-600 bp fragments performing a 0.6X/0.15X 2-sided size selection using DNA clean beads (VAHTS). Size-selected DNA fragments were amplified using NEB unique multiplexed i5 and i7 primers (E6440) in a total reaction volume of 100 µl together with 2 U Phusion High-Fidelity DNA Polymerase (NEB) and in the presence of 0.2 mM dNTPs and 1X Phusion High-Fidelity buffer. PCR was performed in the following conditions: 98 °C/2 min. denaturation, 12 cycles of amplification at 98 °C/10 s, 65 °C/30 s, 72 °C/30 s and final extension at 72 °C for 5 min. Subsequently, libraries were selected by again performing a 0.6X/0.15X 2-sided size selection after which samples were eluted in 20 µl TE buffer (Tris-EDTA buffer 10 mM Tris-HCl and 0.1 mM EDTA, pH 8) and stored at −20 °C. Quality and fragment sizes were evaluated on a fragment analyzer (Advanced Analytical Technologies) and quantified using Picogreen assay (Invitrogen). Equimolar ratios of the obtained libraries were pooled and 150 bp paired-end sequenced on an Illumina NovaSeq S4 platform.

Alignment and Somatic Variant Detection

Raw reads were processed according to GATK4 best practices[135]. Briefly, reads were mapped to the GRCh38 human reference genome and single nucleotide substitutions and InDels were called with Mutect2 in tumor-only mode[136]. Resulting variants were filtered by only retaining variants with Mutect2 quality status 'PASS' and variant allele frequency (VAF) between 0.3 and 0.7. Variants were further filtered by retaining only variants which originated from reads aligned to chromosomes 1-22, X or Y. In order to exclude cell-line specific variants found in the parental clone, we obtained 30x whole genome sequencing (BGITech Global, BGI Genomics Co., Ltd.) from the parental clone (RKO-DOX-Cas9-P2A-GFP) and retained only variants which were not also present in the parental clone.

Bootstrapped Background Correction

We applied a bootstrapping strategy to construct an average background mutational profile from the samples obtained 3 days after transduction with the control sgRNA vector targeting *AAVS1* (n = 3). First, to reduce the effect of outliers, the mutational count of all samples was down-scaled proportional to the sample with the lowest mutation count. For each sample, 10,000 bootstrap samples were generated using weighted random multinomial sampling, with the underlying distribution of mutation counts across the 96 features serving as weights. This process yielded 30,000 bootstrapped samples in total, from which the mean mutation count across the 96 mutation channels was computed, resulting in the final average background profile. The average background mutational profile was subsequently subtracted from the mutational matrix of the samples using element-wise subtraction with thresholding at 0.

1336 **Mutational Signature Analysis**
1337 We conducted signature refitting and plotting using the MutationalPatterns package[137] in R.
1338 Refitting was accomplished by incorporating a catalog of signatures frequently active in colon
1339 carcinoma, alongside APOBEC-related signatures (SBS2 and SBS13), using the best subset
1340 refit approach with the parameter max_delta set to 0.001 to obtain a strict estimate of signature
1341 activity. The significance of the refitting results was assessed using the signature activity test
1342 from the mSigAct package[138]. For the purpose of comparing signature activity across
1343 genotypes, samples were matched by the number of cell doublings.
1344
1345 **Computational analysis of cancer genome sequencing database**
1346 SBS mutational signatures analyzed in the PCAWG study were obtained from the ICGC Data
1347 portal[139]. Corresponding vcf files for each sample were either retrieved from the ICGC Data
1348 portal or through granted access of the TCGA Research Network[140]. To identify the genotype
1349 of a specific gene of interested (E3 ligase) in each sample, the corresponding vcf files (snv and
1350 indel) were tested for variants within the location of the coding gene. Samples exhibiting at
1351 least one variant in either snv or indel with a Variant Classification not being "Intron", were
1352 categorized as "mut". Conversely, the remaining samples were categorized as "wt". SBS
1353 mutational signatures were normalized to the total number of mutations in each sample and
1354 the fraction of SBS signatures of interest compared between "wt"' and "mut" groups. Four E3
1355 ligase genes (*HECTD4*, *NEDD4L*, *HECT1*, *PCHF3*), with a similar number of "mut" cancers
1356 were randomly selected and used for probing specificity.
1357
1358 **Quantification and statistical analysis**
1359 Sample number and number of biological replicates are indicated in the figure legends of all
1360 figures. Statistical analyses were performed with the R (v4.0.2) programming environment
1361 using RStudio (v4.1.3) or GraphPad Prism 10.0.2.

1362 ## References

1363 1. Refsland, E.W., and Harris, R.S. (2013). The APOBEC3 family of retroelement restriction
1364 factors. Curr Top Microbiol Immunol *371*, 1–27. https://doi.org/10.1007/978-3-642-37765-
1365 5_1.

1366 2. Sheehy, A.M., Gaddis, N.C., Choi, J.D., and Malim, M.H. (2002). Isolation of a human
1367 gene that inhibits HIV-1 infection and is suppressed by the viral Vif protein. Nature *418*,
1368 646–650. https://doi.org/10.1038/nature00939.

1369 3. Hultquist, J.F., Lengyel, J.A., Refsland, E.W., LaRue, R.S., Lackey, L., Brown, W.L., and
1370 Harris, R.S. (2011). Human and rhesus APOBEC3D, APOBEC3F, APOBEC3G, and
1371 APOBEC3H demonstrate a conserved capacity to restrict Vif-deficient HIV-1. J Virol *85*,
1372 11220–11234. https://doi.org/10.1128/JVI.05238-11.

1373 4. Harris, R.S., Bishop, K.N., Sheehy, A.M., Craig, H.M., Petersen-Mahrt, S.K., Watt, I.N.,
1374 Neuberger, M.S., and Malim, M.H. (2003). DNA deamination mediates innate immunity to
1375 retroviral infection. Cell *113*, 803–809. https://doi.org/10.1016/s0092-8674(03)00423-9.

1376 5. Lecossier, D., Bouchonnet, F., Clavel, F., and Hance, A.J. (2003). Hypermutation of HIV-
1377 1 DNA in the absence of the Vif protein. Science *300*, 1112.
1378 https://doi.org/10.1126/science.1083338.

1379 6. Mangeat, B., Turelli, P., Caron, G., Friedli, M., Perrin, L., and Trono, D. (2003). Broad
1380 antiretroviral defence by human APOBEC3G through lethal editing of nascent reverse
1381 transcripts. Nature *424*, 99–103. https://doi.org/10.1038/nature01709.

1382 7. Zhang, H., Yang, B., Pomerantz, R.J., Zhang, C., Arunachalam, S.C., and Gao, L.
1383 (2003). The cytidine deaminase CEM15 induces hypermutation in newly synthesized
1384 HIV-1 DNA. Nature *424*, 94–98. https://doi.org/10.1038/nature01707.

1385 8. Rogozin, I.B., Iyer, L.M., Liang, L., Glazko, G.V., Liston, V.G., Pavlov, Y.I., Aravind, L.,
1386 and Pancer, Z. (2007). Evolution and diversification of lamprey antigen receptors:
1387 evidence for involvement of an AID-APOBEC family cytosine deaminase. Nat Immunol *8*,
1388 647–656. https://doi.org/10.1038/ni1463.

1389 9. Conticello, S.G. (2008). The AID/APOBEC family of nucleic acid mutators. Genome Biol
1390 *9*, 229. https://doi.org/10.1186/gb-2008-9-6-229.

1391 10. Wang, X., Abudu, A., Son, S., Dang, Y., Venta, P.J., and Zheng, Y.-H. (2011). Analysis
1392 of human APOBEC3H haplotypes and anti-human immunodeficiency virus type 1
1393 activity. J Virol *85*, 3142–3152. https://doi.org/10.1128/JVI.02049-10.

1394 11. Harari, A., Ooms, M., Mulder, L.C.F., and Simon, V. (2009). Polymorphisms and splice
1395 variants influence the antiretroviral activity of human APOBEC3H. J Virol *83*, 295–303.
1396 https://doi.org/10.1128/JVI.01665-08.

1397 12. OhAinle, M., Kerns, J.A., Li, M.M.H., Malik, H.S., and Emerman, M. (2008).
1398 Antiretroelement activity of APOBEC3H was lost twice in recent human evolution. Cell
1399 Host Microbe *4*, 249–259. https://doi.org/10.1016/j.chom.2008.07.005.

1400 13. Ooms, M., Majdak, S., Seibert, C.W., Harari, A., and Simon, V. (2010). The Localization
1401 of APOBEC3H Variants in HIV-1 Virions Determines Their Antiviral Activity. J Virol *84*,
1402 7961–7969. https://doi.org/10.1128/JVI.00754-10.

1403 14. Li, M.M.H., and Emerman, M. (2011). Polymorphism in human APOBEC3H affects a
1404 phenotype dominant for subcellular localization and antiviral activity. J Virol *85*, 8197–
1405 8207. https://doi.org/10.1128/JVI.00624-11.

1406 15. DeWeerd, R.A., Németh, E., Póti, Á., Petryk, N., Chen, C.-L., Hyrien, O., Szüts, D., and
1407 Green, A.M. (2022). Prospectively defined patterns of APOBEC3A mutagenesis are
1408 prevalent in human cancers. Cell Reports *38*, 110555.
1409 https://doi.org/10.1016/j.celrep.2022.110555.

1410 16. Law, E.K., Levin-Klein, R., Jarvis, M.C., Kim, H., Argyris, P.P., Carpenter, M.A., Starrett,
1411 G.J., Temiz, N.A., Larson, L.K., Durfee, C., et al. (2020). APOBEC3A catalyzes mutation
1412 and drives carcinogenesis in vivo. J Exp Med *217*, e20200261.
1413 https://doi.org/10.1084/jem.20200261.

1414 17. Petljak, M., Dananberg, A., Chu, K., Bergstrom, E.N., Striepen, J., von Morgen, P., Chen,
1415 Y., Shah, H., Sale, J.E., Alexandrov, L.B., et al. (2022). Mechanisms of APOBEC3
1416 mutagenesis in human cancer cells. Nature *607*, 799–807.
1417 https://doi.org/10.1038/s41586-022-04972-y.

1418 18. Starrett, G.J., Luengas, E.M., McCann, J.L., Ebrahimi, D., Temiz, N.A., Love, R.P., Feng,
1419 Y., Adolph, M.B., Chelico, L., Law, E.K., et al. (2016). The DNA cytosine deaminase
1420 APOBEC3H haplotype I likely contributes to breast and lung cancer mutagenesis. Nat
1421 Commun *7*, 12918. https://doi.org/10.1038/ncomms12918.

1422 19. Henderson, S., and Fenton, T. (2015). APOBEC3 genes: retroviral restriction factors to
1423 cancer drivers. Trends Mol Med *21*, 274–284.
1424 https://doi.org/10.1016/j.molmed.2015.02.007.

1425 20. Jalili, P., Bowen, D., Langenbucher, A., Park, S., Aguirre, K., Corcoran, R.B.,
1426 Fleischman, A.G., Lawrence, M.S., Zou, L., and Buisson, R. (2020). Quantification of
1427 ongoing APOBEC3A activity in tumor cells by monitoring RNA editing at hotspots. Nat
1428 Commun *11*, 2971. https://doi.org/10.1038/s41467-020-16802-8.

1429 21. Petljak, M., Alexandrov, L.B., Brammeld, J.S., Price, S., Wedge, D.C., Grossmann, S.,
1430 Dawson, K.J., Ju, Y.S., Iorio, F., Tubio, J.M.C., et al. (2019). Characterizing Mutational
1431 Signatures in Human Cancer Cell Lines Reveals Episodic APOBEC Mutagenesis. Cell
1432 *176*, 1282-1294.e20. https://doi.org/10.1016/j.cell.2019.02.012.

1433 22. Nik-Zainal, S., Alexandrov, L.B., Wedge, D.C., Van Loo, P., Greenman, C.D., Raine, K.,
1434 Jones, D., Hinton, J., Marshall, J., Stebbings, L.A., et al. (2012). Mutational processes
1435 molding the genomes of 21 breast cancers. Cell *149*, 979–993.
1436 https://doi.org/10.1016/j.cell.2012.04.024.

1437 23. Nik-Zainal, S., Davies, H., Staaf, J., Ramakrishna, M., Glodzik, D., Zou, X., Martincorena,
1438 I., Alexandrov, L.B., Martin, S., Wedge, D.C., et al. (2016). Landscape of somatic
1439 mutations in 560 breast cancer whole-genome sequences. Nature *534*, 47–54.
1440 https://doi.org/10.1038/nature17676.

1441 24. Alexandrov, L.B., Nik-Zainal, S., Wedge, D.C., Aparicio, S.A.J.R., Behjati, S., Biankin,
1442 A.V., Bignell, G.R., Bolli, N., Borg, A., Børresen-Dale, A.-L., et al. (2013). Signatures of
1443 mutational processes in human cancer. Nature *500*, 415–421.
1444 https://doi.org/10.1038/nature12477.

1445 25. Roberts, S.A., Lawrence, M.S., Klimczak, L.J., Grimm, S.A., Fargo, D., Stojanov, P.,
1446 Kiezun, A., Kryukov, G.V., Carter, S.L., Saksena, G., et al. (2013). An APOBEC cytidine

1447 deaminase mutagenesis pattern is widespread in human cancers. Nat Genet *45*, 970–
1448 976. https://doi.org/10.1038/ng.2702.

1449 26. de Bruin, E.C., McGranahan, N., Mitter, R., Salm, M., Wedge, D.C., Yates, L., Jamal-
1450 Hanjani, M., Shafi, S., Murugaesu, N., Rowan, A.J., et al. (2014). Spatial and temporal
1451 diversity in genomic instability processes defines lung cancer evolution. Science *346*,
1452 251–256. https://doi.org/10.1126/science.1253462.

1453 27. Morganella, S., Alexandrov, L.B., Glodzik, D., Zou, X., Davies, H., Staaf, J., Sieuwerts,
1454 A.M., Brinkman, A.B., Martin, S., Ramakrishna, M., et al. (2016). The topography of
1455 mutational processes in breast cancer genomes. Nat Commun *7*, 11383.
1456 https://doi.org/10.1038/ncomms11383.

1457 28. Carpenter, M.A., Temiz, N.A., Ibrahim, M.A., Jarvis, M.C., Brown, M.R., Argyris, P.P.,
1458 Brown, W.L., Starrett, G.J., Yee, D., and Harris, R.S. (2023). Mutational impact of
1459 APOBEC3A and APOBEC3B in a human cell line and comparisons to breast cancer.
1460 PLoS Genet *19*, e1011043. https://doi.org/10.1371/journal.pgen.1011043.

1461 29. Bergstrom, E.N., Luebeck, J., Petljak, M., Khandekar, A., Barnes, M., Zhang, T., Steele,
1462 C.D., Pillay, N., Landi, M.T., Bafna, V., et al. (2022). Mapping clustered mutations in
1463 cancer reveals APOBEC3 mutagenesis of ecDNA. Nature *602*, 510–517.
1464 https://doi.org/10.1038/s41586-022-04398-6.

1465 30. Alexandrov, L.B., Kim, J., Haradhvala, N.J., Huang, M.N., Tian Ng, A.W., Wu, Y., Boot,
1466 A., Covington, K.R., Gordenin, D.A., Bergstrom, E.N., et al. (2020). The repertoire of
1467 mutational signatures in human cancer. Nature *578*, 94–101.
1468 https://doi.org/10.1038/s41586-020-1943-3.

1469 31. Dananberg, A., Striepen, J., Rozowsky, J.S., and Petljak, M. (2024). APOBEC
1470 Mutagenesis in Cancer Development and Susceptibility. Cancers (Basel) *16*, 374.
1471 https://doi.org/10.3390/cancers16020374.

1472 32. Hix, M.A., Wong, L., Flath, B., Chelico, L., and Cisneros, G.A. (2020). Single-nucleotide
1473 polymorphism of the DNA cytosine deaminase APOBEC3H haplotype I leads to enzyme
1474 destabilization and correlates with lung cancer. NAR Cancer *2*, zcaa023.
1475 https://doi.org/10.1093/narcan/zcaa023.

1476 33. Sanchez, A., Ortega, P., Sakhtemani, R., Manjunath, L., Oh, S., Bournique, E., Becker,
1477 A., Kim, K., Durfee, C., Temiz, N.A., et al. (2024). Mesoscale DNA features impact
1478 APOBEC3A and APOBEC3B deaminase activity and shape tumor mutational
1479 landscapes. Nat Commun *15*, 2370. https://doi.org/10.1038/s41467-024-45909-5.

1480 34. Burns, M.B., Lackey, L., Carpenter, M.A., Rathore, A., Land, A.M., Leonard, B., Refsland,
1481 E.W., Kotandeniya, D., Tretyakova, N., Nikas, J.B., et al. (2013). APOBEC3B is an
1482 enzymatic source of mutation in breast cancer. Nature *494*, 366–370.
1483 https://doi.org/10.1038/nature11881.

1484 35. Burns, M.B., Temiz, N.A., and Harris, R.S. (2013). Evidence for APOBEC3B
1485 mutagenesis in multiple human cancers. Nat Genet *45*, 977–983.
1486 https://doi.org/10.1038/ng.2701.

1487 36. Apolonia, L., Schulz, R., Curk, T., Rocha, P., Swanson, C.M., Schaller, T., Ule, J., and
1488 Malim, M.H. (2015). Promiscuous RNA binding ensures effective encapsidation of
1489 APOBEC3 proteins by HIV-1. PLoS Pathog *11*, e1004609.
1490 https://doi.org/10.1371/journal.ppat.1004609.

1491 37. York, A., Kutluay, S.B., Errando, M., and Bieniasz, P.D. (2016). The RNA Binding
1492 Specificity of Human APOBEC3 Proteins Resembles That of HIV-1 Nucleocapsid. PLoS
1493 Pathog *12*, e1005833. https://doi.org/10.1371/journal.ppat.1005833.

1494 38. Dang, Y., Siew, L.M., Wang, X., Han, Y., Lampen, R., and Zheng, Y.-H. (2008). Human
1495 cytidine deaminase APOBEC3H restricts HIV-1 replication. J Biol Chem *283*, 11606–
1496 11614. https://doi.org/10.1074/jbc.M707586200.

1497 39. Shaban, N.M., Shi, K., Lauer, K.V., Carpenter, M.A., Richards, C.M., Salamango, D.,
1498 Wang, J., Lopresti, M.W., Banerjee, S., Levin-Klein, R., et al. (2018). The Antiviral and
1499 Cancer Genomic DNA Deaminase APOBEC3H Is Regulated by an RNA-Mediated
1500 Dimerization Mechanism. Mol Cell *69*, 75-86.e9.
1501 https://doi.org/10.1016/j.molcel.2017.12.010.

1502 40. Refsland, E.W., Hultquist, J.F., Luengas, E.M., Ikeda, T., Shaban, N.M., Law, E.K.,
1503 Brown, W.L., Reilly, C., Emerman, M., and Harris, R.S. (2014). Natural polymorphisms in
1504 human APOBEC3H and HIV-1 Vif combine in primary T lymphocytes to affect viral G-to-
1505 A mutation levels and infectivity. PLoS Genet *10*, e1004761.
1506 https://doi.org/10.1371/journal.pgen.1004761.

1507 41. Lackey, L., Demorest, Z.L., Land, A.M., Hultquist, J.F., Brown, W.L., and Harris, R.S.
1508 (2012). APOBEC3B and AID have similar nuclear import mechanisms. J Mol Biol *419*,
1509 301–314. https://doi.org/10.1016/j.jmb.2012.03.011.

1510 42. Salamango, D.J., Becker, J.T., McCann, J.L., Cheng, A.Z., Demir, Ö., Amaro, R.E.,
1511 Brown, W.L., Shaban, N.M., and Harris, R.S. (2018). APOBEC3H Subcellular
1512 Localization Determinants Define Zipcode for Targeting HIV-1 for Restriction. Mol Cell
1513 Biol *38*, e00356-18. https://doi.org/10.1128/MCB.00356-18.

1514 43. Chesarino, N.M., and Emerman, M. (2020). Polymorphisms in Human APOBEC3H
1515 Differentially Regulate Ubiquitination and Antiviral Activity. Viruses *12*, 378.
1516 https://doi.org/10.3390/v12040378.

1517 44. de Almeida, M., Hinterndorfer, M., Brunner, H., Grishkovskaya, I., Singh, K., Schleiffer,
1518 A., Jude, J., Deswal, S., Kalis, R., Vunjak, M., et al. (2021). AKIRIN2 controls the nuclear
1519 import of proteasomes in vertebrates. Nature *599*, 491–496.
1520 https://doi.org/10.1038/s41586-021-04035-8.

1521 45. Vunjak, M., Schwartz, I., Cantoran García, A., Mastrovito, M., Hinterndorfer, M., de
1522 Almeida, M., Budroni, V., Wang, J., Froussios, K., Jude, J., et al. (2022). SPOP targets
1523 the immune transcription factor IRF1 for proteasomal degradation (Cell Biology)
1524 https://doi.org/10.1101/2022.10.10.511567.

1525 46. Scinicariello, S., Soderholm, A., Schäfer, M., Shulkina, A., Schwartz, I., Hacker, K.,
1526 Gogova, R., Kalis, R., Froussios, K., Budroni, V., et al. (2023). HUWE1 controls
1527 tristetraprolin proteasomal degradation by regulating its phosphorylation. Elife *12*,
1528 e83159. https://doi.org/10.7554/eLife.83159.

1529 47. Jang, G.M., Annan Sudarsan, A.K., Shayeganmehr, A., Prando Munhoz, E., Lao, R.,
1530 Gaba, A., Granadillo Rodríguez, M., Love, R.P., Polacco, B.J., Zhou, Y., et al. (2024).
1531 Protein interaction map of APOBEC3 enzyme family reveals deamination-independent
1532 role in cellular function. Mol Cell Proteomics, 100755.
1533 https://doi.org/10.1016/j.mcpro.2024.100755.

1534 48. Gallois-Montbrun, S., Kramer, B., Swanson, C.M., Byers, H., Lynham, S., Ward, M., and
1535 Malim, M.H. (2007). Antiviral protein APOBEC3G localizes to ribonucleoprotein

1536 complexes found in P bodies and stress granules. J Virol *81*, 2165–2178.
1537 https://doi.org/10.1128/JVI.02287-06.

1538 49. Izumi, T., Burdick, R., Shigemi, M., Plisov, S., Hu, W.-S., and Pathak, V.K. (2013).
1539 Mov10 and APOBEC3G localization to processing bodies is not required for virion
1540 incorporation and antiviral activity. J Virol *87*, 11047–11062.
1541 https://doi.org/10.1128/JVI.02070-13.

1542 50. Phalora, P.K., Sherer, N.M., Wolinsky, S.M., Swanson, C.M., and Malim, M.H. (2012).
1543 HIV-1 replication and APOBEC3 antiviral activity are not regulated by P bodies. J Virol
1544 *86*, 11712–11724. https://doi.org/10.1128/JVI.00595-12.

1545 51. Kozak, S.L., Marin, M., Rose, K.M., Bystrom, C., and Kabat, D. (2006). The anti-HIV-1
1546 editing enzyme APOBEC3G binds HIV-1 RNA and messenger RNAs that shuttle
1547 between polysomes and stress granules. J Biol Chem *281*, 29105–29119.
1548 https://doi.org/10.1074/jbc.M601901200.

1549 52. Ito, F., Yang, H., Xiao, X., Li, S.-X., Wolfe, A., Zirkle, B., Arutiunian, V., and Chen, X.S.
1550 (2018). Understanding the Structure, Multimerization, Subcellular Localization and mC
1551 Selectivity of a Genomic Mutator and Anti-HIV Factor APOBEC3H. Sci Rep *8*, 3763.
1552 https://doi.org/10.1038/s41598-018-21955-0.

1553 53. Zhen, A., Du, J., Zhou, X., Xiong, Y., and Yu, X.-F. (2012). Reduced APOBEC3H variant
1554 anti-viral activities are associated with altered RNA binding activities. PLoS One *7*,
1555 e38771. https://doi.org/10.1371/journal.pone.0038771.

1556 54. Polevoda, B., Joseph, R., Friedman, A.E., Bennett, R.P., Greiner, R., De Zoysa, T.,
1557 Stewart, R.A., and Smith, H.C. (2017). DNA mutagenic activity and capacity for HIV-1
1558 restriction of the cytidine deaminase APOBEC3G depend on whether DNA or RNA binds
1559 to tyrosine 315. Journal of Biological Chemistry *292*, 8642–8656.
1560 https://doi.org/10.1074/jbc.M116.767889.

1561 55. Matsuoka, T., Nagae, T., Ode, H., Awazu, H., Kurosawa, T., Hamano, A., Matsuoka, K.,
1562 Hachiya, A., Imahashi, M., Yokomaku, Y., et al. (2018). Structural basis of chimpanzee
1563 APOBEC3H dimerization stabilized by double-stranded RNA. Nucleic Acids Research
1564 *46*, 10368–10379. https://doi.org/10.1093/nar/gky676.

1565 56. Bohn, J.A., Thummar, K., York, A., Raymond, A., Brown, W.C., Bieniasz, P.D.,
1566 Hatziioannou, T., and Smith, J.L. (2017). APOBEC3H structure reveals an unusual
1567 mechanism of interaction with duplex RNA. Nat Commun *8*, 1021.
1568 https://doi.org/10.1038/s41467-017-01309-6.

1569 57. Yau, R.G., Doerner, K., Castellanos, E.R., Haakonsen, D.L., Werner, A., Wang, N.,
1570 Yang, X.W., Martinez-Martin, N., Matsumoto, M.L., Dixit, V.M., et al. (2017). Assembly
1571 and Function of Heterotypic Ubiquitin Chains in Cell-Cycle and Protein Quality Control.
1572 Cell *171*, 918-933.e20. https://doi.org/10.1016/j.cell.2017.09.040.

1573 58. Perner, J., Abbas, S., Nowicki-Osuch, K., Devonshire, G., Eldridge, M.D., Tavaré, S., and
1574 Fitzgerald, R.C. (2020). The mutREAD method detects mutational signatures from low
1575 quantities of cancer DNA. Nat Commun *11*, 3166. https://doi.org/10.1038/s41467-020-
1576 16974-3.

1577 59. The ICGC/TCGA Pan-Cancer Analysis of Whole Genomes Consortium, Aaltonen, L.A.,
1578 Abascal, F., Abeshouse, A., Aburatani, H., Adams, D.J., Agrawal, N., Ahn, K.S., Ahn, S.-
1579 M., Aikata, H., et al. (2020). Pan-cancer analysis of whole genomes. Nature *578*, 82–93.
1580 https://doi.org/10.1038/s41586-020-1969-6.

1581 60. Butler, K., and Banday, A.R. (2023). APOBEC3-mediated mutagenesis in cancer:
1582 causes, clinical significance and therapeutic potential. J Hematol Oncol *16*, 31.
1583 https://doi.org/10.1186/s13045-023-01425-5.

1584 61. Durfee, C., Temiz, N.A., Levin-Klein, R., Argyris, P.P., Alsøe, L., Carracedo, S., Alonso
1585 de la Vega, A., Proehl, J., Holzhauer, A.M., Seeman, Z.J., et al. (2023). Human
1586 APOBEC3B promotes tumor development in vivo including signature mutations and
1587 metastases. Cell Rep Med *4*, 101211. https://doi.org/10.1016/j.xcrm.2023.101211.

1588 62. McCann, J.L., Cristini, A., Law, E.K., Lee, S.Y., Tellier, M., Carpenter, M.A., Beghè, C.,
1589 Kim, J.J., Sanchez, A., Jarvis, M.C., et al. (2023). APOBEC3B regulates R-loops and
1590 promotes transcription-associated mutagenesis in cancer. Nat Genet *55*, 1721–1734.
1591 https://doi.org/10.1038/s41588-023-01504-w.

1592 63. Middlebrooks, C.D., Banday, A.R., Matsuda, K., Udquim, K.-I., Onabajo, O.O., Paquin,
1593 A., Figueroa, J.D., Zhu, B., Koutros, S., Kubo, M., et al. (2016). Association of germline
1594 variants in the APOBEC3 region with cancer risk and enrichment with APOBEC-
1595 signature mutations in tumors. Nat Genet *48*, 1330–1338.
1596 https://doi.org/10.1038/ng.3670.

1597 64. Law, E.K., Sieuwerts, A.M., LaPara, K., Leonard, B., Starrett, G.J., Molan, A.M., Temiz,
1598 N.A., Vogel, R.I., Meijer-van Gelder, M.E., Sweep, F.C.G.J., et al. (2016). The DNA
1599 cytosine deaminase APOBEC3B promotes tamoxifen resistance in ER-positive breast
1600 cancer. Sci Adv *2*, e1601737. https://doi.org/10.1126/sciadv.1601737.

1601 65. Stopak, K.S., Chiu, Y.-L., Kropp, J., Grant, R.M., and Greene, W.C. (2007). Distinct
1602 patterns of cytokine regulation of APOBEC3G expression and activity in primary
1603 lymphocytes, macrophages, and dendritic cells. J Biol Chem *282*, 3539–3546.
1604 https://doi.org/10.1074/jbc.M610138200.

1605 66. Kreisberg, J.F., Yonemoto, W., and Greene, W.C. (2006). Endogenous factors enhance
1606 HIV infection of tissue naive CD4 T cells by stimulating high molecular mass APOBEC3G
1607 complex formation. J Exp Med *203*, 865–870. https://doi.org/10.1084/jem.20051856.

1608 67. Soros, V.B., Yonemoto, W., and Greene, W.C. (2007). Newly synthesized APOBEC3G is
1609 incorporated into HIV virions, inhibited by HIV RNA, and subsequently activated by
1610 RNase H. PLoS Pathog *3*, e15. https://doi.org/10.1371/journal.ppat.0030015.

1611 68. Friew, Y.N., Boyko, V., Hu, W.-S., and Pathak, V.K. (2009). Intracellular interactions
1612 between APOBEC3G, RNA, and HIV-1 Gag: APOBEC3G multimerization is dependent
1613 on its association with RNA. Retrovirology *6*, 56. https://doi.org/10.1186/1742-4690-6-56.

1614 69. Khan, M.A., Goila-Gaur, R., Opi, S., Miyagi, E., Takeuchi, H., Kao, S., and Strebel, K.
1615 (2007). Analysis of the contribution of cellular and viral RNA to the packaging of
1616 APOBEC3G into HIV-1 virions. Retrovirology *4*, 48. https://doi.org/10.1186/1742-4690-4-
1617 48.

1618 70. Wittkopp, C.J., Adolph, M.B., Wu, L.I., Chelico, L., and Emerman, M. (2016). A Single
1619 Nucleotide Polymorphism in Human APOBEC3C Enhances Restriction of Lentiviruses.
1620 PLoS Pathog *12*, e1005865. https://doi.org/10.1371/journal.ppat.1005865.

1621 71. Monda, J.K., Ge, X., Hunkeler, M., Donovan, K.A., Ma, M.W., Jin, C.Y., Leonard, M.,
1622 Fischer, E.S., and Bennett, E.J. (2023). HAPSTR1 localizes HUWE1 to the nucleus to
1623 limit stress signaling pathways. Cell Reports *42*.
1624 https://doi.org/10.1016/j.celrep.2023.112496.

1625 72. Xu, Y., Anderson, D.E., and Ye, Y. (2016). The HECT domain ubiquitin ligase HUWE1
1626 targets unassembled soluble proteins for degradation. Cell Discov *2*, 1–16.
1627 https://doi.org/10.1038/celldisc.2016.40.

1628 73. Tripathi, S., Pohl, M.O., Zhou, Y., Rodriguez-Frandsen, A., Wang, G., Stein, D.A.,
1629 Moulton, H.M., DeJesus, P., Che, J., Mulder, L.C.F., et al. (2015). Meta- and Orthogonal
1630 Integration of Influenza "OMICs" Data Defines a Role for UBR4 in Virus Budding. Cell
1631 Host & Microbe *18*, 723–735. https://doi.org/10.1016/j.chom.2015.11.002.

1632 74. Kim, S.T., Lee, Y.J., Tasaki, T., Hwang, J., Kang, M.J., Yi, E.C., Kim, B.Y., and Kwon,
1633 Y.T. (2018). The N-recognin UBR4 of the N-end rule pathway is required for
1634 neurogenesis and homeostasis of cell surface proteins. PLOS ONE *13*, e0202260.
1635 https://doi.org/10.1371/journal.pone.0202260.

1636 75. Chen, L.J., Xu, W.M., Yang, M., Wang, K., Chen, Y., Huang, X.J., and Ma, Q.H. (2016).
1637 HUWE1 plays important role in mouse preimplantation embryo development and the
1638 dysregulation is associated with poor embryo development in humans. Sci Rep *6*, 37928.
1639 https://doi.org/10.1038/srep37928.

1640 76. Shearer, R.F., Frikstad, K.-A.M., McKenna, J., McCloy, R.A., Deng, N., Burgess, A.,
1641 Stokke, T., Patzke, S., and Saunders, D.N. (2018). The E3 ubiquitin ligase UBR5
1642 regulates centriolar satellite stability and primary cilia. MBoC *29*, 1542–1554.
1643 https://doi.org/10.1091/mbc.E17-04-0248.

1644 77. Sanchez, A., De Vivo, A., Uprety, N., Kim, J., Stevens, S.M., and Kee, Y. (2016). BMI1–
1645 UBR5 axis regulates transcriptional repression at damaged chromatin. Proceedings of
1646 the National Academy of Sciences *113*, 11243–11248.
1647 https://doi.org/10.1073/pnas.1610735113.

1648 78. Xiang, G., Wang, S., Chen, L., Song, M., Song, X., Wang, H., Zhou, P., Ma, X., and Yu,
1649 J. (2022). UBR5 targets tumor suppressor CDC73 proteolytically to promote aggressive
1650 breast cancer. Cell Death Dis *13*, 1–14. https://doi.org/10.1038/s41419-022-04914-6.

1651 79. Jang, G.M., Sudarsan, A.K.A., Shayeganmehr, A., Munhoz, E.P., Lao, R., Gaba, A.,
1652 Rodríguez, M.G., Love, R.P., Polacco, B.J., Zhou, Y., et al. (2024). Protein interaction
1653 map of APOBEC3 enzyme family reveals deamination-independent role in cellular
1654 function. bioRxiv, 2024.02.06.579137. https://doi.org/10.1101/2024.02.06.579137.

1655 80. Esnault, C., Millet, J., Schwartz, O., and Heidmann, T. (2006). Dual inhibitory effects of
1656 APOBEC family proteins on retrotransposition of mammalian endogenous retroviruses.
1657 Nucleic Acids Res *34*, 1522–1531. https://doi.org/10.1093/nar/gkl054.

1658 81. Nakaya, Y., Stavrou, S., Blouch, K., Tattersall, P., and Ross, S.R. (2016). In Vivo
1659 Examination of Mouse APOBEC3- and Human APOBEC3A- and APOBEC3G-Mediated
1660 Restriction of Parvovirus and Herpesvirus Infection in Mouse Models. J Virol *90*, 8005–
1661 8012. https://doi.org/10.1128/JVI.00973-16.

1662 82. Moraes, S.N., Becker, J.T., Moghadasi, S.A., Shaban, N.M., Auerbach, A.A., Cheng,
1663 A.Z., and Harris, R.S. (2022). Evidence linking APOBEC3B genesis and evolution of
1664 innate immune antagonism by gamma-herpesvirus ribonucleotide reductases. Elife *11*,
1665 e83893. https://doi.org/10.7554/eLife.83893.

1666 83. Cheng, A.Z., Yockteng-Melgar, J., Jarvis, M.C., Malik-Soni, N., Borozan, I., Carpenter,
1667 M.A., McCann, J.L., Ebrahimi, D., Shaban, N.M., Marcon, E., et al. (2019). Epstein-Barr
1668 virus BORF2 inhibits cellular APOBEC3B to preserve viral genome integrity. Nat
1669 Microbiol *4*, 78–88. https://doi.org/10.1038/s41564-018-0284-6.

1670 84. Zhang, Z., Gu, Q., de Manuel Montero, M., Bravo, I.G., Marques-Bonet, T., Häussinger,
1671 D., and Münk, C. (2017). Stably expressed APOBEC3H forms a barrier for cross-species
1672 transmission of simian immunodeficiency virus of chimpanzee to humans. PLoS Pathog
1673 *13*, e1006746. https://doi.org/10.1371/journal.ppat.1006746.

1674 85. Chen, Y., Hu, J., Cai, X., Huang, Y., Zhou, X., Tu, Z., Hu, J., Tavis, J.E., Tang, N.,
1675 Huang, A., et al. (2018). APOBEC3B edits HBV DNA and inhibits HBV replication during
1676 reverse transcription. Antiviral Res *149*, 16–25.
1677 https://doi.org/10.1016/j.antiviral.2017.11.006.

1678 86. Bandarra, S., Miyagi, E., Ribeiro, A.C., Gonçalves, J., Strebel, K., and Barahona, I.
1679 (2021). APOBEC3B Potently Restricts HIV-2 but Not HIV-1 in a Vif-Dependent Manner. J
1680 Virol *95*, e0117021. https://doi.org/10.1128/JVI.01170-21.

1681 87. Mark, K.G., Kolla, S., Aguirre, J.D., Garshott, D.M., Schmitt, S., Haakonsen, D.L., Xu, C.,
1682 Kater, L., Kempf, G., Martínez-González, B., et al. (2023). Orphan quality control shapes
1683 network dynamics and gene expression. Cell *186*, 3460-3475.e23.
1684 https://doi.org/10.1016/j.cell.2023.06.015.

1685 88. Tsai, J.M., Aguirre, J.D., Li, Y.-D., Brown, J., Focht, V., Kater, L., Kempf, G., Sandoval,
1686 B., Schmitt, S., Rutter, J.C., et al. (2023). UBR5 forms ligand-dependent complexes on
1687 chromatin to regulate nuclear hormone receptor stability. Mol Cell *83*, 2753-2767.e10.
1688 https://doi.org/10.1016/j.molcel.2023.06.028.

1689 89. Kaisari, S., Miniowitz-Shemtov, S., Sitry-Shevah, D., Shomer, P., Kozlov, G., Gehring, K.,
1690 and Hershko, A. (2022). Role of ubiquitin-protein ligase UBR5 in the disassembly of
1691 mitotic checkpoint complexes. Proc Natl Acad Sci U S A *119*, e2121478119.
1692 https://doi.org/10.1073/pnas.2121478119.

1693 90. Hehl, L.A., Horn-Ghetko, D., Prabu, J.R., Vollrath, R., Vu, D.T., Pérez Berrocal, D.A.,
1694 Mulder, M.P.C., van der Heden van Noort, G.J., and Schulman, B.A. (2024). Structural
1695 snapshots along K48-linked ubiquitin chain formation by the HECT E3 UBR5. Nat Chem
1696 Biol *20*, 190–200. https://doi.org/10.1038/s41589-023-01414-2.

1697 91. Hodáková, Z., Grishkovskaya, I., Brunner, H.L., Bolhuis, D.L., Belačić, K., Schleiffer, A.,
1698 Kotisch, H., Brown, N.G., and Haselbach, D. (2023). Cryo-EM structure of the chain-
1699 elongating E3 ubiquitin ligase UBR5. EMBO J *42*, e113348.
1700 https://doi.org/10.15252/embj.2022113348.

1701 92. Wang, F., He, Q., Zhan, W., Yu, Z., Finkin-Groner, E., Ma, X., Lin, G., and Li, H. (2023).
1702 Structure of the human UBR5 E3 ubiquitin ligase. Structure *31*, 541-552.e4.
1703 https://doi.org/10.1016/j.str.2023.03.010.

1704 93. Heidelberger, J.B., Voigt, A., Borisova, M.E., Petrosino, G., Ruf, S., Wagner, S.A., and
1705 Beli, P. (2018). Proteomic profiling of VCP substrates links VCP to K6-linked
1706 ubiquitylation and c-Myc function. EMBO Rep *19*, e44754.
1707 https://doi.org/10.15252/embr.201744754.

1708 94. Hong, J.H., Kaustov, L., Coyaud, E., Srikumar, T., Wan, J., Arrowsmith, C., and Raught,
1709 B. (2015). KCMF1 (potassium channel modulatory factor 1) Links RAD6 to UBR4
1710 (ubiquitin N-recognin domain-containing E3 ligase 4) and lysosome-mediated
1711 degradation. Mol Cell Proteomics *14*, 674–685.
1712 https://doi.org/10.1074/mcp.M114.042168.

95. Haakonsen, D.L., Heider, M., Ingersoll, A.J., Vodehnal, K., Witus, S.R., Uenaka, T., Wernig, M., and Rapé, M. (2024). Stress response silencing by an E3 ligase mutated in neurodegeneration. Nature *626*, 874–880. https://doi.org/10.1038/s41586-023-06985-7.

96. Leto, D.E., Morgens, D.W., Zhang, L., Walczak, C.P., Elias, J.E., Bassik, M.C., and Kopito, R.R. (2019). Genome-wide CRISPR Analysis Identifies Substrate-Specific Conjugation Modules in ER-Associated Degradation. Mol Cell *73*, 377-389.e11. https://doi.org/10.1016/j.molcel.2018.11.015.

97. Cassidy, K.B., Bang, S., Kurokawa, M., and Gerber, S.A. (2020). Direct regulation of Chk1 protein stability by E3 ubiquitin ligase HUWE1. FEBS J *287*, 1985–1999. https://doi.org/10.1111/febs.15132.

98. Kunz, V., Bommert, K.S., Kruk, J., Schwinning, D., Chatterjee, M., Stühmer, T., Bargou, R., and Bommert, K. (2020). Targeting of the E3 ubiquitin-protein ligase HUWE1 impairs DNA repair capacity and tumor growth in preclinical multiple myeloma models. Sci Rep *10*, 18419. https://doi.org/10.1038/s41598-020-75499-3.

99. Thompson, J.W., Nagel, J., Hoving, S., Gerrits, B., Bauer, A., Thomas, J.R., Kirschner, M.W., Schirle, M., and Luchansky, S.J. (2014). Quantitative Lys-ϵ-Gly-Gly (diGly) proteomics coupled with inducible RNAi reveals ubiquitin-mediated proteolysis of DNA damage-inducible transcript 4 (DDIT4) by the E3 ligase HUWE1. J Biol Chem *289*, 28942–28955. https://doi.org/10.1074/jbc.M114.573352.

100. D'Arca, D., Zhao, X., Xu, W., Ramirez-Martinez, N.C., Iavarone, A., and Lasorella, A. (2010). Huwe1 ubiquitin ligase is essential to synchronize neuronal and glial differentiation in the developing cerebellum. Proc Natl Acad Sci U S A *107*, 5875–5880. https://doi.org/10.1073/pnas.0912874107.

101. Poulsen, E.G., Steinhauer, C., Lees, M., Lauridsen, A.-M., Ellgaard, L., and Hartmann-Petersen, R. (2012). HUWE1 and TRIP12 collaborate in degradation of ubiquitin-fusion proteins and misframed ubiquitin. PLoS One *7*, e50548. https://doi.org/10.1371/journal.pone.0050548.

102. Hegazi, S., Cheng, A.H., Krupp, J.J., Tasaki, T., Liu, J., Szulc, D.A., Ling, H.H., Rios Garcia, J., Seecharran, S., Basiri, T., et al. (2022). UBR4/POE facilitates secretory trafficking to maintain circadian clock synchrony. Nat Commun *13*, 1594. https://doi.org/10.1038/s41467-022-29244-1.

103. Hunt, L.C., Stover, J., Haugen, B., Shaw, T.I., Li, Y., Pagala, V.R., Finkelstein, D., Barton, E.R., Fan, Y., Labelle, M., et al. (2019). A Key Role for the Ubiquitin Ligase UBR4 in Myofiber Hypertrophy in Drosophila and Mice. Cell Rep *28*, 1268-1281.e6. https://doi.org/10.1016/j.celrep.2019.06.094.

104. Jeong, D.E., Lee, H.S., Ku, B., Kim, C.-H., Kim, S.J., and Shin, H.-C. (2023). Insights into the recognition mechanism in the UBR box of UBR4 for its specific substrates. Commun Biol *6*, 1214. https://doi.org/10.1038/s42003-023-05602-7.

105. Rinschen, M.M., Bharill, P., Wu, X., Kohli, P., Reinert, M.J., Kretz, O., Saez, I., Schermer, B., Höhne, M., Bartram, M.P., et al. (2016). The ubiquitin ligase Ubr4 controls stability of podocin/MEC-2 supercomplexes. Hum Mol Genet *25*, 1328–1344. https://doi.org/10.1093/hmg/ddw016.

106. Hunkeler, M., Jin, C.Y., Ma, M.W., Monda, J.K., Overwijn, D., Bennett, E.J., and Fischer, E.S. (2021). Solenoid architecture of HUWE1 contributes to ligase activity and

1757 substrate recognition. Mol Cell *81*, 3468-3480.e7.
1758 https://doi.org/10.1016/j.molcel.2021.06.032.

1759 107. Grabarczyk, D.B., Petrova, O.A., Deszcz, L., Kurzbauer, R., Murphy, P., Ahel, J.,
1760 Vogel, A., Gogova, R., Faas, V., Kordic, D., et al. (2021). HUWE1 employs a giant
1761 substrate-binding ring to feed and regulate its HECT E3 domain. Nat Chem Biol *17*,
1762 1084–1092. https://doi.org/10.1038/s41589-021-00831-5.

1763 108. Ohtake, F., Tsuchiya, H., Saeki, Y., and Tanaka, K. (2018). K63 ubiquitylation triggers
1764 proteasomal degradation by seeding branched ubiquitin chains. Proc Natl Acad Sci USA
1765 *115*, E1401–E1408. https://doi.org/10.1073/pnas.1716673115.

1766 109. Manasanch, E.E., and Orlowski, R.Z. (2017). Proteasome Inhibitors in Cancer
1767 Therapy. Nat Rev Clin Oncol *14*, 417–433. https://doi.org/10.1038/nrclinonc.2016.206.

1768 110. Venkatesan, S., Rosenthal, R., Kanu, N., McGranahan, N., Bartek, J., Quezada, S.A.,
1769 Hare, J., Harris, R.S., and Swanton, C. (2018). Perspective: APOBEC mutagenesis in
1770 drug resistance and immune escape in HIV and cancer evolution. Ann Oncol *29*, 563–
1771 572. https://doi.org/10.1093/annonc/mdy003.

1772 111. Coxon, M., Dennis, M.A., Dananberg, A., Collins, C.D., Wilson, H.E., Meekma, J.,
1773 Savenkova, M.I., Ng, D., Osbron, C.A., Mertz, T.M., et al. (2023). An impaired ubiquitin-
1774 proteasome system increases APOBEC3A abundance. NAR Cancer *5*, zcad058.
1775 https://doi.org/10.1093/narcan/zcad058.

1776 112. Shlyakhtenko, L.S., Lushnikov, A.J., Li, M., Harris, R.S., and Lyubchenko, Y.L.
1777 (2014). Interaction of APOBEC3A with DNA assessed by atomic force microscopy. PLoS
1778 One *9*, e99354. https://doi.org/10.1371/journal.pone.0099354.

1779 113. Chen, X.S. (2021). Insights into the Structures and Multimeric Status of APOBEC
1780 Proteins Involved in Viral Restriction and Other Cellular Functions. Viruses *13*, 497.
1781 https://doi.org/10.3390/v13030497.

1782 114. Bohn, M.-F., Shandilya, S.M.D., Silvas, T.V., Nalivaika, E.A., Kouno, T., Kelch, B.A.,
1783 Ryder, S.P., Kurt-Yilmaz, N., Somasundaran, M., and Schiffer, C.A. (2015). The ssDNA
1784 Mutator APOBEC3A Is Regulated by Cooperative Dimerization. Structure *23*, 903–911.
1785 https://doi.org/10.1016/j.str.2015.03.016.

1786 115. Huthoff, H., Autore, F., Gallois-Montbrun, S., Fraternali, F., and Malim, M.H. (2009).
1787 RNA-Dependent Oligomerization of APOBEC3G Is Required for Restriction of HIV-1.
1788 PLoS Pathog *5*, e1000330. https://doi.org/10.1371/journal.ppat.1000330.

1789 116. Aydin, H., Taylor, M.W., and Lee, J.E. (2014). Structure-guided analysis of the human
1790 APOBEC3-HIV restrictome. Structure *22*, 668–684.
1791 https://doi.org/10.1016/j.str.2014.02.011.

1792 117. Michlits, G., Jude, J., Hinterndorfer, M., de Almeida, M., Vainorius, G., Hubmann, M.,
1793 Neumann, T., Schleiffer, A., Burkard, T.R., Fellner, M., et al. (2020). Multilayered VBC
1794 score predicts sgRNAs that efficiently generate loss-of-function alleles. Nat Methods *17*,
1795 708–716. https://doi.org/10.1038/s41592-020-0850-8.

1796 118. Schwartz, I., Vunjak, M., Budroni, V., Cantoran García, A., Mastrovito, M., Soderholm,
1797 A., Hinterndorfer, M., de Almeida, M., Hacker, K., Wang, J., et al. (2023). SPOP targets
1798 the immune transcription factor IRF1 for proteasomal degradation. Elife *12*, e89951.
1799 https://doi.org/10.7554/eLife.89951.

1800 119. Hatziioannou, T., Cowan, S., and Bieniasz, P.D. (2004). Capsid-dependent and -
1801 independent postentry restriction of primate lentivirus tropism in rodent cells. J Virol *78*,
1802 1006–1011. https://doi.org/10.1128/jvi.78.2.1006-1011.2004.

1803 120. Yee, J.K., Friedmann, T., and Burns, J.C. (1994). Generation of high-titer
1804 pseudotyped retroviral vectors with very broad host range. Methods Cell Biol *43 Pt A*,
1805 99–112. https://doi.org/10.1016/s0091-679x(08)60600-7.

1806 121. Li, W., Xu, H., Xiao, T., Cong, L., Love, M.I., Zhang, F., Irizarry, R.A., Liu, J.S., Brown,
1807 M., and Liu, X.S. (2014). MAGeCK enables robust identification of essential genes from
1808 genome-scale CRISPR/Cas9 knockout screens. Genome Biol *15*, 554.
1809 https://doi.org/10.1186/s13059-014-0554-4.

1810 122. Suzuki, K., Bose, P., Leong-Quong, R.Y., Fujita, D.J., and Riabowol, K. (2010).
1811 REAP: A two minute cell fractionation method. BMC Res Notes *3*, 294.
1812 https://doi.org/10.1186/1756-0500-3-294.

1813 123. Artan, M., Hartl, M., Chen, W., and de Bono, M. (2022). Depletion of endogenously
1814 biotinylated carboxylases enhances the sensitivity of TurboID-mediated proximity
1815 labeling in Caenorhabditis elegans. J Biol Chem *298*, 102343.
1816 https://doi.org/10.1016/j.jbc.2022.102343.

1817 124. Rappsilber, J., Mann, M., and Ishihama, Y. (2007). Protocol for micro-purification,
1818 enrichment, pre-fractionation and storage of peptides for proteomics using StageTips.
1819 Nat Protoc *2*, 1896–1906. https://doi.org/10.1038/nprot.2007.261.

1820 125. Tyanova, S., Temu, T., and Cox, J. (2016). The MaxQuant computational platform for
1821 mass spectrometry-based shotgun proteomics. Nat Protoc *11*, 2301–2319.
1822 https://doi.org/10.1038/nprot.2016.136.

1823 126. UniProt https://www.uniprot.org/.

1824 127. R: The R Project for Statistical Computing https://www.r-project.org/.

1825 128. Madern, M. (2023). Cassiopeia_LFQ.

1826 129. Chen, E.Y., Tan, C.M., Kou, Y., Duan, Q., Wang, Z., Meirelles, G.V., Clark, N.R., and
1827 Ma'ayan, A. (2013). Enrichr: interactive and collaborative HTML5 gene list enrichment
1828 analysis tool. BMC Bioinformatics *14*, 128. https://doi.org/10.1186/1471-2105-14-128.

1829 130. Kuleshov, M.V., Jones, M.R., Rouillard, A.D., Fernandez, N.F., Duan, Q., Wang, Z.,
1830 Koplev, S., Jenkins, S.L., Jagodnik, K.M., Lachmann, A., et al. (2016). Enrichr: a
1831 comprehensive gene set enrichment analysis web server 2016 update. Nucleic Acids
1832 Res *44*, W90-97. https://doi.org/10.1093/nar/gkw377.

1833 131. Xie, Z., Bailey, A., Kuleshov, M.V., Clarke, D.J.B., Evangelista, J.E., Jenkins, S.L.,
1834 Lachmann, A., Wojciechowicz, M.L., Kropiwnicki, E., Jagodnik, K.M., et al. (2021). Gene
1835 Set Knowledge Discovery with Enrichr. Curr Protoc *1*, e90.
1836 https://doi.org/10.1002/cpz1.90.

1837 132. Perez-Riverol, Y., Csordas, A., Bai, J., Bernal-Llinares, M., Hewapathirana, S.,
1838 Kundu, D.J., Inuganti, A., Griss, J., Mayer, G., Eisenacher, M., et al. (2019). The PRIDE
1839 database and related tools and resources in 2019: improving support for quantification
1840 data. Nucleic Acids Res *47*, D442–D450. https://doi.org/10.1093/nar/gky1106.

1841 133. Neuhold, J., Radakovics, K., Lehner, A., Weissmann, F., Garcia, M.Q., Romero, M.C.,
1842 Berrow, N.S., and Stolt-Bergner, P. (2020). GoldenBac: a simple, highly efficient, and
1843 widely applicable system for construction of multi-gene expression vectors for use with
1844 the baculovirus expression vector system. BMC Biotechnology *20*, 26.
1845 https://doi.org/10.1186/s12896-020-00616-z.

1846 134. Ehrmann, J.F., Grabarczyk, D.B., Heinke, M., Deszcz, L., Kurzbauer, R., Hudecz, O.,
1847 Shulkina, A., Gogova, R., Meinhart, A., Versteeg, G.A., et al. (2023). Structural basis for
1848 regulation of apoptosis and autophagy by the BIRC6/SMAC complex. Science *379*,
1849 1117–1123. https://doi.org/10.1126/science.ade8873.

1850 135. GATK https://gatk.broadinstitute.org/hc/en-us.

1851 136. Benjamin, D., Sato, T., Cibulskis, K., Getz, G., Stewart, C., and Lichtenstein, L.
1852 (2019). Calling Somatic SNVs and Indels with Mutect2. Preprint at bioRxiv,
1853 https://doi.org/10.1101/861054 https://doi.org/10.1101/861054.

1854 137. MutationalPatterns (2024). (UMCU Genetics).

1855 138. Rozen, S.G. (2024). mSigAct.

1856 139. DCC Data Releases | ICGC Data Portal https://dcc.icgc.org/releases/PCAWG.

1857 140. The Cancer Genome Atlas Program (TCGA) - NCI (2022).
1858 https://www.cancer.gov/ccg/research/genome-sequencing/tcga.